Thesis for the degree of Doctor of Philosophy

Transport and Collective Dynamics in Fermi and Non-Fermi Liquids

Eric Nilsson

Department of Physics and Astronomy
Chalmers University of Technology
Gothenburg, Sweden, 2026

Transport and Collective Dynamics in Fermi and Non-Fermi Liquids
Eric Nilsson
ISBN: 978-91-8103-417-2.

Acknowledgments, dedications, and similar personal statements in this thesis, reflect the author's own views.

This thesis has been printed using LaTeX.

Doktorsavhandlingar vid Chalmers tekniska högskola
Ny serie nr 5874
ISSN 0346-718X
https://doi.org/10.63959/chalmers.dt/5874

Department of Physics and Astronomy
Chalmers University of Technology
SE-412 96 Gothenburg
Sweden
Telephone +46 (0)31-772 10 00

Cover: Artistic illustration of the dual nature of this thesis. The left side represents Fermi liquid physics, electron hydrodynamics, and quasiparticle excitations. The right side captures electrically charged black holes in holography, which model electromagnetic collective dynamics in strongly correlated systems. The figure was generated using OpenAI's ChatGPT Images 2.0.

Chalmers digitaltryck
Gothenburg, Sweden, 2026

Transport and Collective Dynamics in Fermi and Non-Fermi Liquids
Eric Nilsson
Department of Physics and Astronomy
Chalmers University of Technology

Abstract

Modern quantum materials host a wide range of electronic phases in which transport properties are governed by strong interactions and collective effects. This thesis investigates charge, heat, and momentum transport in interacting electronic systems across different theoretical frameworks, ranging from Fermi liquid theory to strongly coupled strange metals.

The first part of the thesis focuses on two-dimensional Fermi liquids at finite temperature, where rapid electron-electron scattering can give rise to hydrodynamic behavior. A kinetic-theory framework allowing an exact treatment of quasiparticle distribution functions beyond the asymptotic low-temperature regime is used to compute the full spectrum of collective modes, providing a detailed characterization of long-lived odd-parity excitations and the intermediate transport regime between ballistic and hydrodynamic flow. The same framework is employed to determine the shear viscosity of interacting electron liquids beyond conventional perturbative limits.

The second part of the thesis concerns strongly interacting quantum systems where the quasiparticle picture breaks down. Holographic duality is used to study transport and thermoelectric response in quantum critical systems subject to periodic potentials, providing a controlled framework for momentum relaxation and magnetotransport in non-Fermi liquids. The thesis further develops holographic models of collective charge dynamics in systems with dynamical electromagnetism, including bulk plasmons and surface plasmon polaritons, and explores connections between Fermi surface physics and holographic gauge-field dynamics.

Keywords: electron transport, kinetic theory, hydrodynamics, non-Fermi liquids, strange metals, holography, plasmons, surface plasmon polaritons

List of publications

This thesis is partly based on the author's licentiate thesis [1]:
Electron Transport and Collective Modes in Fermi and Non-Fermi Liquids, Eric Nilsson (2024).

It consists of an introductory text and the following papers:

I **Nonequilibrium relaxation and odd-even effect in finite-temperature electron gases**
E. Nilsson, U. Gran, J. Hofmann
Phys. Rev. X **15**, 041007 (2025)

II **Shear viscosity in interacting two-dimensional Fermi liquids**
E. Nilsson, J. Hofmann
Preprint: arXiv:2312.09977 [cond-mat.mes-hall]

III **Quantum critical theories in a periodic potential: strange metallic thermoelectric and magnetotransport**
E. Nilsson, K. Schalm
Preprint: arXiv:2512.19480 [hep-th]
In review for JHEP

IV **Holographic electrodynamics: surface plasmon polaritons**
U. Gran, E. Nilsson
In manuscript

V **Plasmons in holographic ersatz Fermi Liquids**
E. Ismailov, U. Gran, E. Nilsson
Preprint: arXiv:2605.03865 [cond-mat.str-el]

Statement of contributions

My contributions to the included papers were:

I I performed all of the data analysis and produced all of the results and the majority of figures. I did the analytical calculations and wrote the first draft of the paper, finalizing it together with my co-authors.

II I derived the low-temperature analytical results, and performed the comparison against known theoretical results and experimental data. I partook in finalizing the paper together with my co-authors.

III I wrote the code (building on previously written code), ran all of the simulations and produced all of the numerical results and figures. I wrote a first draft of the paper and finalized it together with my co-author.

IV I wrote all of the code, performed all numerical computations and produced all of the figures. I came up with the idea on how to formulate the specific combination of boundary conditions and how to obtain a well-behaved response function. I wrote the manuscript included in this thesis.

V I proposed the original idea of the project and contributed to the development of the numerical code used to solve the equations of motion. I participated in the writing of the manuscript together with my co-authors.

Acknowledgments

First, I would like to extend my sincere gratitude to my supervisor Prof. Ulf Gran for the guidance, help, and time devoted to me during the last five years. You have been not only a supervisor, but a friend, and always cared about my well-being. I have thoroughly enjoyed our time together!

Second, a large thank you to Prof. Koenraad Schalm at Leiden University — my extended stay in the Netherlands was one of the highlights of the PhD. Your hospitality and mentorship were greatly appreciated, and I look forward to our upcoming collaborations.

Furthermore, I would like to thank Prof. Johannes Hofmann for the collaborations and supervision, and the counsel on condensed matter physics in general. Our projects gave me a much-needed breadth in my knowledge of physics. Thanks also to my collaborator and office-mate Eli Ismailov. Having another student to discuss holography with made the last year of my PhD that much more fun!

I am grateful to my co-supervisor Prof. Christian Forssén for inspiring scientific rigor, and to my examiner Prof. Martin Cederwall for making any bureaucratic formality as simple as possible. Prof. Bengt EW Nilsson also deserves a special mention for his continuous encouragement and for getting me on the track I am now on. During my master's, you allowed me to take a one-on-one course on advanced quantum field theory the day before the semester started, which cemented my path to theoretical physics. For this I am very grateful.

Thanks to the rest of the colleagues at the division of subatomic, high energy and plasma physics — you will be missed! I want to particularly acknowledge my partner-in-crime Oliver Thim for 10 years of physics studies together, and thank him for the support, the music, and the many helpful discussions over the years. I would also like to thank Nicolas Chagnet, Aravindh Swaminathan Shankar and Calvin Bakker for great discussions during my time in Leiden.

This work was supported by the Area of Advance Nano (formerly Excellence Initiative Nano) at Chalmers University of Technology. A large thank you for allowing me to follow my interests.

Finally, I would like to send love to my family and, most of all, my dear Malin. Without you, this effort would mean nothing.

Contents

1

Introduction

"I am a beacon of knowledge blazing out across a black sea of ignorance!"

Invoker

Landau's Fermi liquid theory [2] is a cornerstone of condensed matter physics. Its central ingredient is the existence of well-defined *quasiparticles*: long-lived electronic degrees of freedom responsible for the dynamics of the system [3]. This framework successfully describes ordinary metals, where the scattering of weakly interacting quasiparticles leads to familiar metallic behavior. Under sufficiently strong interactions, however, this picture can change qualitatively. The electronic system may instead exhibit collective dynamics that cannot be understood in terms of nearly independent particle motion alone.

This thesis explores two such regimes. The first concerns ultra-clean two-dimensional materials where electron-electron interactions can dominate over other scattering processes. The electrons can then behave collectively as a viscous fluid, exhibiting hydrodynamic transport. The second concerns *non*-Fermi liquids, where the interactions become so strong that the quasiparticle picture itself breaks down. Understanding such systems requires fundamentally different approaches to quantum many-body physics.

Conventional metallic transport

As a current runs through a metal, the conduction electrons scatter off impurities, other sources of disorder, and phonons (lattice vibrations) [4]. These processes dissipate the total electron momentum, thereby governing transport properties such as the electrical resistivity. The dominant contribution is de-

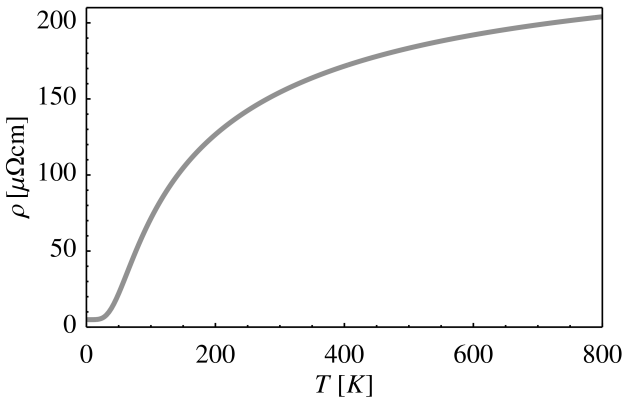

Figure 1.1: Schematic temperature dependence of the resistivity in a conventional metal, illustrating residual resistivity, electron–phonon scattering, and eventual saturation near the Mott-Ioffe-Regel limit. While the figure is not intended to represent any particular material quantitatively, it qualitatively resembles the behavior of Nb_3Sb [9].

termined by the fastest characteristic scattering rate, which heuristically corresponds to the inverse average time between a specific scattering event.

For instance, the electron-phonon scattering rate increases rapidly once the temperature approaches the Debye temperature[1] $\Theta_D \simeq 100$–500 K [6], and therefore becomes the dominant process at higher temperatures. By contrast, disorder scattering is typically temperature independent and instead determined by the crystal purity of the material. Finally, the electron-electron scattering rate generally scales as $\Gamma_{ee} \sim T^2/T_F$, where T_F is the Fermi temperature [7]. However, since $T_F \gtrsim 10^4$ K in most three-dimensional metals [6], this process is typically subleading.

In the case of the electrical resistivity, this results in the following phenomenological picture [7]. At low temperatures, there is a residual contribution to the resistivity from disorder scattering, together with a subleading T^2-correction from electron-electron interactions. As the temperature is increased, electron-phonon scattering takes over, resulting in a T^5 scaling that crosses over to a T-linear scaling beyond the Debye temperature [6]. Eventually, the system can reach its Mott-Ioffe-Regel (MIR) limit, which can be understood as the point when at which the electron mean free path becomes comparable to the interatomic spacing, causing the resistivity to saturate [8]. Figure 1.1 illustrates this characteristic temperature dependence of the resistivity in a conventional metal, which will serve as a useful reference point for the two directions explored in this thesis.

[1] In the two-dimensional materials we discuss next, it is rather the Bloch-Grüneisen temperature which is the relevant scale [5]. Nevertheless, the same logic applies.

Two-dimensional Fermi liquids

The above picture can change markedly as one goes from three dimensions to two. Especially in the case of low carrier densities, two-dimensional materials can exhibit Fermi temperatures below 100 K [10], making electron-electron collisions significantly more frequent than in ordinary three-dimensional metals. At the same time, recent advances in fabrication techniques have enabled extremely clean samples in which impurity scattering is strongly suppressed [11]. The result is an extended *interaction-dominated* regime, where the temperature is high enough to make electron-electron scattering occur more frequently than impurity scattering, yet still low enough that phonon scattering remains subleading.

This scenario is novel for two reasons. First, sufficiently frequent electron-electron collisions can effectively redistribute energy throughout the electron subsystem, driving it toward local thermal equilibrium. The electrons then reach a hydrodynamic regime, behaving collectively as a fluid rather than as individual particles. Second, the electron-electron interaction conserves total momentum, meaning that the dominant scattering mechanism does not relax the electrical current. This instead happens through comparatively infrequent interactions with impurities, phonons, or the boundaries of the sample.

If momentum loss through the boundaries dominates while the electrons are in a hydrodynamic regime, the transport properties become governed by the collective fluid dynamics. In particular, the resistivity is determined by the viscous drag exerted along the edges of the sample. How efficiently this momentum loss propagates to the rest of the fluid is determined by the *shear viscosity*, which is notably an intrinsic property of the electron fluid itself, and not of the medium through which it flows [12]. This can even lead to a decrease of the resistivity with increasing temperature, since more frequent electron-electron collisions improve the collective flow of the electron fluid [13]. Hydrodynamic electron flow therefore represents a distinct departure from the typical dissipative (Ohmic) transport described above.

Hydrodynamic electron behavior has now been reported in mono- [14–19] and bilayer [20] graphene, (Al,Ga)As heterostructures [10, 21–23], GaAs quantum wells [24, 25], $PdCoO_2$ [26] and in Weyl semimetals [27], through signatures such as a parabolic flow profile due to the aforementioned viscous drag [27], or a negative local resistivity due to current backflow caused by vortices [28]. These effects could potentially play a role in future electronic devices, for instance by allowing the resistivity in nanostructures to go below previously thought fundamental limits [12].

In two dimensions, the momentum and energy conservation of electron-electron interactions also lead to strong restrictions on the phase space available for scattering near the Fermi surface. As a consequence, certain types of electron-electron scattering are suppressed, which results in the appearance of

an additional, much slower rate $\Gamma_{ee} \sim T^4/T_F^3$ [29]. The interaction-dominated regime can therefore involve multiple parametrically distinct timescales. This enables the existence of another, so-called *tomographic* regime that combines aspects of collective hydrodynamic flow with more conventional quasiparticle transport, and which has garnered significant attention recently [29–40].

From a theoretical perspective, the lower Fermi temperature of two-dimensional materials introduces important challenges. Perturbative low-temperature expansions in T/T_F, which are very successful in three dimensions [41], become much more limited. There is also a significant broadening of the Fermi surface near the Fermi temperature, reducing the effectiveness of Pauli blocking and enhancing the role of collisions throughout momentum space. At the same time, the system is still far from the classical high-temperature limit. One therefore requires a complete mathematical description of interacting electrons that remains valid across the entire temperature range relevant for the interaction-dominated regime.

This motivates Part I of this thesis. In Paper I, we present a numerical solution of the kinetic equation describing a two-dimensional electron liquid interacting through a screened Coulomb interaction. The general formalism is able to describe the crossover between different interaction-dominated transport regimes, including the recently proposed tomographic regime. The solution is then applied in Paper II to calculate the shear viscosity of the electron liquid at arbitrary temperatures.

Strange metals: non-Fermi liquid physics

The aforementioned hydrodynamic regime occurs when the electron-electron interactions become sufficiently strong and frequent to dominate the transport dynamics. At the same time, it still lies within the framework of Fermi liquid theory: the charge-carrying degrees of freedom are not the bare electrons themselves, but rather long-lived electron quasiparticles. Their comparatively long lifetimes still permit a particle-based description. However, there exist systems with interparticle correlations so strong that the quasiparticle lifetimes become comparable to microscopic quantum timescales, rendering the quasiparticle description invalid. Instead, such systems behave as strongly correlated electron "soups" [42]. This exemplifies *non*-Fermi liquid physics, which represents a major area of interest in contemporary condensed matter physics.

The canonical example of non-Fermi liquid behavior is the *strange metal* phase of cuprate and iron-based high-temperature superconductors. It is the metallic phase out of which superconductivity emerges, and sits above the superconducting dome in the phase diagram [43], which is schematically illustrated in Figure 1.2. Unlike conventional superconductors explained by Bardeen-Cooper-Schrieffer (BCS) theory [44], the underlying microscopic mechanism of

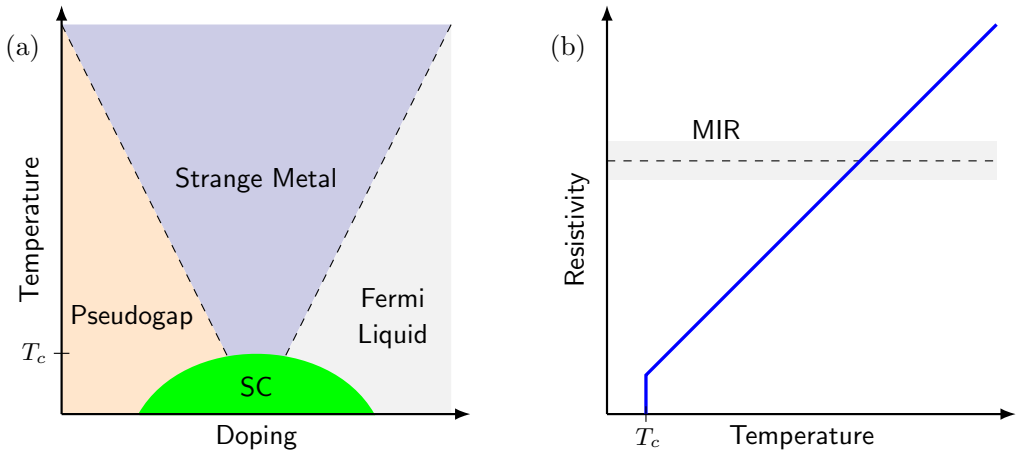

Figure 1.2: (a) Schematic phase diagram of hole-doped high-temperature superconductors [43]. Above the superconducting dome (SC) sits the strange metal phase. (b) Schematic illustration of the corresponding resistivity as a function of temperature at optimal doping [46].

superconductivity in these materials remains unresolved, despite decades of research since their discovery in 1986 [45]. Even more puzzling is the strange metal phase itself, which exhibits several unconventional transport properties.

Near optimal doping, where the superconducting transition temperature T_c is maximal, the resistivity increases almost perfectly linearly with temperature above T_c [47]. Perhaps even more surprising is that the resistivity can continue smoothly beyond the MIR limit and keep growing linearly, in principle until the material melts[2]. This stands in stark contrast to the conventional metallic transport discussed previously. Understanding the mechanism behind this remarkably robust linearity could potentially allow for the engineering of materials that are superconducting at even higher temperatures, as the linear-in-T slope appears to be related to T_c [46].

Measurements of the optical conductivity reveal another surprising feature of strange metals [48]. Using the Drude formula of the conductivity to extract a relaxation time τ (although the applicability of the Drude picture in this regime is questionable), one finds it to be very short: in fact, it comes close to the *Planckian timescale*[3]

$$\tau_{\mathrm{pl}} = \frac{\hbar}{k_B T}\,, \tag{1.1}$$

where $\hbar$ and k_B are Planck's and Boltzmann's constants, respectively. This corresponds to an extremely rapid relaxation rate set only by temperature and fundamental constants, and is characteristic of strongly interacting quantum matter [49]. The Planckian timescale, which can also be inferred from the T-

[2]Metals that violate the MIR limit are called *bad metals* in the regime above the limit.

[3]Not to be confused with the *Planck* time $t_P = \sqrt{\hbar G/c^5} \approx 10^{-44}\,\mathrm{s}$.

linear resistivity [50], is associated with a highly entangled many-body state, and signals that the charge carriers need not be interpreted as particles [46].

Holographic duality for condensed matter systems

Non-Fermi liquids, and strange metals in particular, pose a great theoretical challenge to conventional many-body methods, which almost all rely on the quasiparticle concept. Additionally, brute-force simulations of interacting electrons are severely limited by the fermion sign problem [51] that complicates the convergence of numerical quantum Monte Carlo algorithms[4] [53].

One promising approach instead comes from holographic duality. In this framework, a strongly correlated theory admits a dual description in terms of a weakly coupled gravitational theory in a higher dimension [54, 55]. The low-energy dynamics of the strongly correlated system are then encoded in black hole physics, where rapid, nearly Planckian relaxation and the absence of long-lived quasiparticles emerge naturally [56].

Although the holographic duality is best understood for systems that at first glance differ substantially from those of condensed matter physics, many experimentally relevant phenomena are governed by the emergent low-energy physics that can be remarkably insensitive to the microscopic details. Holographic models can therefore provide valuable insight into universal aspects of strongly correlated quantum matter. Indeed, holographic models of strange metals have reproduced several qualitative features observed experimentally, including the linear-in-T resistivity [57] and aspects of the unconventional optical conductivity.

However, the phenomenology of strange metals extends well beyond the linear-in-T resistivity and optical conductivity. Experiments have also revealed anomalous magnetotransport, such as a Hall angle with different temperature scaling than the resistivity [46], as well as a B-linear longitudinal magnetoresistance [58–60], together with unusual collective charge dynamics observed through momentum-resolved spectroscopy [61–64]. Understanding how these features emerge from strongly interacting quantum matter remains an important open problem.

These questions motivate the holographic models studied in Part II of this thesis. In Paper III, we investigate the effects of strong translational symmetry breaking on thermoelectric and magnetotransport, and show that there exists an extended regime with roughly B-linear magnetoresistance. In Paper IV, we extend the holographic framework of the collective charge response to also include the surface charge response. Finally, in Paper V, we explore a novel type of holographic model that builds in an explicit Fermi surface through an anomaly, and investigate the implications on the charge response.

[4] Some progress has been made on this front in models of quantum critical systems [52].

Part I
Fermi liquid transport

2

Kinetic theory of interacting electrons

"Zip! Zap!"

Storm Spirit

Kinetic theory provides the standard framework for describing transport in interacting Fermi liquids. This chapter introduces the kinetic framework underlying Papers I and II, and serves as the basis for the transport analysis in Chapter 3.

2.1 The quasiparticle

Many-body physics is notoriously difficult. While we know the governing equation — the Schrödinger equation — solving it while accounting for all particles in a piece of material is generically impossible. However, Landau realized in the 50s that only a small subset of the electrons in the system will meaningfully contribute to the physical processes of interest [2]. We begin by imagining adiabatically turning on the interactions between the fermionic electrons. The assumption is that as the system evolves from a free Fermi gas toward an interacting Fermi liquid, there exists a one-to-one mapping between the low-energy eigenstates of the free and interacting theories. As a result, the ground states of the two systems are adiabatically connected, implying that a well-defined Fermi surface survives[1] [65].

Next, we turn to the excited states, which, due to the interactions, are now able to decay. However, Pauli blocking prevents scattering into already

[1] In a metal, i.e., charged fermions within an ionic potential, interactions generally modify the shape of the Fermi surface. However, the resulting ground state remains adiabatically connected to an excited state of the free theory, and therefore does not invalidate the quasiparticle picture [3].

occupied states in the Fermi sea; thus, the closer a state is to the Fermi surface, the smaller the phase space for decay. For low-energy excitations, one finds an inverse lifetime[2] [7]

$$\frac{1}{\tau} \sim (\epsilon - E_F)^2 + (\pi k_B T)^2 \,, \tag{2.1}$$

which vanishes at the Fermi surface ($\epsilon = E_F$) at zero temperature. Crucially, the inverse lifetime vanishes faster than the excitation energy itself, ensuring that excitations near the Fermi surface form well-defined low-energy degrees of freedom. In the language of Green's functions, this corresponds to a pole with vanishing imaginary part at the Fermi surface [3].

Further away from the Fermi surface, the available phase space for scattering grows rapidly, and the excitations decay accordingly. The only excitations that contribute non-trivially to low-energy physical processes are therefore those close to the Fermi surface: these are the quasiparticles, understood as the adiabatic continuation of non-interacting electrons into the interacting system [7]. While their quantum numbers remain unchanged, their properties are renormalized — for instance, for the *quasielectrons* we will consider here, the bare electron mass is replaced by the effective mass m^*. Although quasiparticles are strictly well-defined only near the Fermi surface, we will nevertheless refer to all momentum states as quasiparticle states here, with the understanding that only those near the Fermi surface are long-lived and relevant for low-energy dynamics.

It is worth emphasizing that, unlike many of our most successful theories of nature — such as general relativity or the Standard Model — Fermi liquid theory is not traditionally formulated in terms of a fundamental action. Instead, it emerges as an effective low-energy description of interacting fermions. Modern approaches do formulate Fermi liquids in terms of an *effective* action in the sense of effective field theory [67–69]. A renormalization group (RG) analysis[3] reveals that in two dimensions and up, most four-fermion interaction channels are irrelevant in the infrared. The two notable marginal exceptions are the BCS instability, responsible for superconductivity, and forward scattering, which gives rise to the phenomenological parameters Landau introduced. In this sense, Landau effectively "guessed" the correct low-energy theory from intuition alone. We will return to this effective description in Chapter 6, where it will be used to encode the Fermi surface in theories where the quasiparticle description breaks down.

[2] In two dimensions, there are additional logarithmic corrections [66].

[3] This is non-trivial since the RG flow must be performed toward the Fermi surface rather than toward zero momentum.

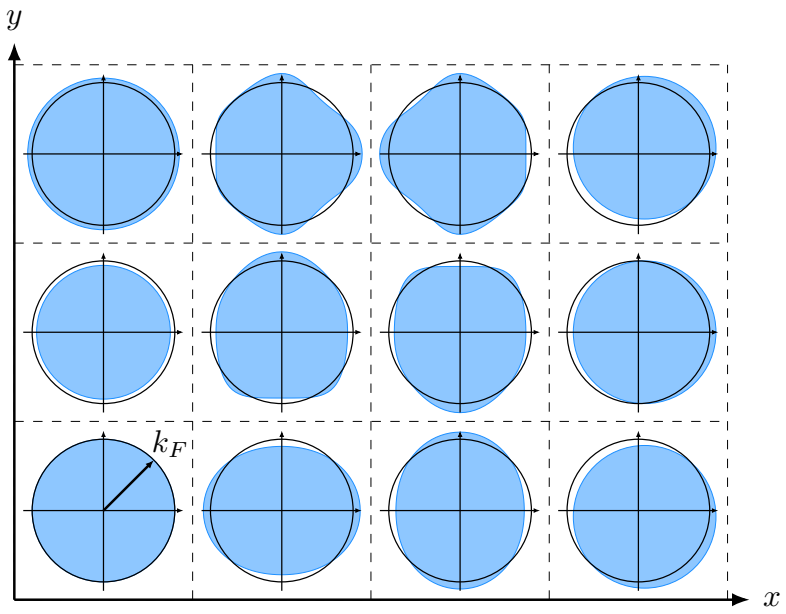

Figure 2.1: Coarse-graining of the electron system required for a semiclassical description in terms of a quasiparticle distribution function $f(t; \boldsymbol{r}, \boldsymbol{p})$. At each point in space, there is a distribution $f(t; \boldsymbol{p})$ (blue), which may or may not align with the Fermi surface (black circle). The system is in local equilibrium only in the bottom left.

2.2 The kinetic equation

Having established the existence of long-lived quasiparticles as the relevant degrees of freedom, a second simplification of the many-body problem comes from adopting a statistical description of the system. Consider the quasiparticle distribution function $f(t; \boldsymbol{r}, \boldsymbol{p})$, acting as a probability distribution function in phase space. For this description to make sense, we must effectively coarse-grain the system: at each mesoscopic point in space, there must be enough electrons to form a Fermi surface such that a quasiparticle description is valid. At the same time, we must be studying phenomena on length scales much larger than the inverse Fermi wave vector k_F^{-1} such that these discrete mesoscopic points may be treated as a continuum. This restriction also brings us to length- and time scales much larger than those of the atomic constituents, enabling the explicit dependence on both the position $\boldsymbol{r}$ and momentum[4] $\hbar\boldsymbol{p}$, despite the apparent tension with the uncertainty principle [65]. We can thus imagine a local Fermi surface, together with an accompanying quasiparticle distribution $f(t; \boldsymbol{p})$, at each point in space, as is schematically illustrated in Figure 2.1.

The dynamics of the quasiparticle distribution is governed by the semiclassical kinetic equation

[4]We let $\boldsymbol{p}$ denote the wave vector, so the momentum carried by a quasiparticle wave packet is $\hbar\boldsymbol{p}$.

$$\left(\frac{\partial}{\partial t} + \boldsymbol{v}\cdot\frac{\partial}{\partial \boldsymbol{r}} - \frac{\partial U}{\partial \boldsymbol{r}}\cdot\frac{\partial}{\partial \hbar\boldsymbol{p}}\right) f(t;\boldsymbol{r},\boldsymbol{p}) = I[f(t;\boldsymbol{r},\boldsymbol{p})]\,, \tag{2.2}$$

where $\boldsymbol{v} = \hbar\boldsymbol{p}/m^*$ is the quasiparticle velocity, m^* the effective mass, and $\boldsymbol{F} = -\partial U/\partial \boldsymbol{r}$ the force from an external potential $U(\boldsymbol{r})$. The spatial and momentum derivatives on the left-hand side combine into a classical Poisson bracket $\{H, f\}$ between a mean-field Hamiltonian $H = \hbar^2\boldsymbol{p}^2/2m^* + U(\boldsymbol{r})$ and the distribution function, which is referred to as the *streaming term*. In the absence of a right-hand side, (2.2) therefore assumes the form of a classical Liouville equation, and indeed describes a continuity equation balancing the flow of probability through the volume element $\mathrm{d}^d\boldsymbol{r}\,\mathrm{d}^d\boldsymbol{p}$ in phase space [70].

This continuity flow is broken by collisions with other quasiparticles, captured in the *collision integral* $I[f(t;\boldsymbol{r},\boldsymbol{p})]$ which encodes the relaxation rate of the quasiparticles. Introducing the shorthand $f_i^{(\prime)} = f(t;\boldsymbol{r},\boldsymbol{p}_i^{(\prime)})$, the collision integral reads

$$\begin{aligned} I[f(t;\boldsymbol{r},\boldsymbol{p}_1)] = -\int \frac{\mathrm{d}\boldsymbol{p}_2\,\mathrm{d}\boldsymbol{p}_1'\,\mathrm{d}\boldsymbol{p}_2'}{(2\pi)^{2d}} W(\boldsymbol{p}_1\boldsymbol{p}_2|\boldsymbol{p}_1'\boldsymbol{p}_2') \\ \times\left[f_1 f_2(1-f_1')(1-f_2') - f_1' f_2'(1-f_1)(1-f_2)\right]\,, \end{aligned} \tag{2.3}$$

where $W(\boldsymbol{p}_1\boldsymbol{p}_2|\boldsymbol{p}_1'\boldsymbol{p}_2')$ is a matrix element describing the scattering between states of momenta $\boldsymbol{p}_1, \boldsymbol{p}_2$ and $\boldsymbol{p}_1', \boldsymbol{p}_2'$. The two terms in square brackets describe the in- and out-flux of particles scattering to and from the states with momentum $\boldsymbol{p}_1$ and $\boldsymbol{p}_2$. Technically, the collision integral depends on the two-particle distribution function $f^{(2)}(t;\boldsymbol{r}_1,\boldsymbol{p}_1;\boldsymbol{r}_2,\boldsymbol{p}_2)$, which in turn satisfies its own kinetic equation with a collision integral dependent on the three-particle distribution, and so on: this is the BBGKY hierarchy [71]. Assuming the correlations to be weak and the particle collision time scale τ_{coll} to be much smaller than the scattering time scale τ on which $f(t;\boldsymbol{p},\boldsymbol{r})$ varies, we have here truncated this hierarchy to first order, which leads to (2.3).

For energy- and momentum-conserving interactions, such as the electron-electron interaction, the kinetic equation admits the general local solution

$$f(t;\boldsymbol{r},\boldsymbol{p}) = \frac{1}{e^{\beta(\varepsilon(\boldsymbol{p})-\mu-\hbar\boldsymbol{p}\cdot\boldsymbol{V})}+1}\,. \tag{2.4}$$

Here, $\varepsilon(\boldsymbol{p})$ is the quasiparticle dispersion, $\boldsymbol{V}(t,\boldsymbol{r})$ is the local velocity field of the quasiparticles, and in general, the chemical potential $\mu(t,\boldsymbol{r})$ and inverse temperature $\beta = 1/k_BT(t,\boldsymbol{r})$ may also be functions of both space and time. By virtue of satisfying the property of *detailed balance*,

$$\frac{f_1 f_2}{(1-f_1)(1-f_2)} = \frac{f_1' f_2'}{(1-f_1')(1-f_2')}\,, \tag{2.5}$$

the distribution (2.4) is annihilated by the collision integral (2.3), making the dynamics controlled by the streaming term alone. Equation (2.4) generalizes the Fermi-Dirac distribution, which additionally has a vanishing streaming term and therefore satisfies $\partial_t f = 0$.

2.2.1 Limitations of the semiclassical description

While the streaming term $\{H, f\}$ remains the same as in a purely classical description, the semiclassical label makes itself apparent from the blocking factors $(1 - f)$ in the collision integral, which are of quantum origin. Equation (2.2) can therefore be seen as a classical Boltzmann equation with a select set of important quantum effects built in, namely the constraints on the scattering phase space. While this formulation can seem quite phenomenological — we are starting from an equation of motion, not an action principle — a more rigorous derivation of a quantum kinetic equation can be made by starting from a Keldysh effective action [72], where a Wigner transformation allows for a quantum mechanical representation of phase space [73, 74]. After an approximation of having well-defined quasiparticles[5], (2.2) emerges as a lowest-order gradient expansion of the underlying quantum theory [74]. In these steps, the memory effects[6] of the quantum theory are neglected, limiting our discussion to timescales above the saturation of the time-energy uncertainty relation.

One could ask whether the description of a quasiparticle distribution function is limited to low temperatures, as the quasiparticle concept requires that $E_{\mathrm{qp}}\tau_{\mathrm{qp}} \gg \hbar$ [75] and quasiparticle lifetime τ_{qp} generally decreases with increased temperature due to an increased collision rate. In Paper I we compute an entire spectrum of quasiparticle lifetimes, and while they do reach their minimum values near the Fermi temperature T_F where the thermal and quantum effects become comparable, they still satisfy the aforementioned inequality.

At even higher temperatures, the gas transitions into a non-degenerate regime, with a typical inter-particle spacing much larger than the thermal wavelength $\lambda_T = \sqrt{2\pi\hbar^2/m^* k_B T}$. In the collision integral, the blocking factors $(1 - f)$ vanish, and the background solution (2.4) instead takes on a Maxwell-Boltzmann form. The semiclassical kinetic equation therefore reduces to the classical Boltzmann equation in the high-temperature regime, effectively describing a gas of wave packets of size λ_T.

2.2.2 Coupled systems

Aside from the aforementioned limitations, we have a controlled and widely applicable description of the physics governing a gas of interacting electrons. It

[5] Even for strong interactions, where the quasiparticle approximation would be poor, a kinetic equation of similar form can still be derived using a semiclassical approximation [73].

[6] In the quantum description, the collision integral involves an integral over time, and there is no conservation of energy due to $\delta E \delta t \geq \hbar$.

is, however, highly non-trivial to solve the non-linear integro-differential kinetic equation (2.2), made further complicated by the fact that condensed matter systems in general contain several species of quasiparticles. Each species obeys their own kinetic equation, which couple through the collision integral as [76]

$$\partial_t f^{(i)} - \{H^{(i)}, f^{(i)}\} = \sum_j I^{(i)}[f^{(i)}, f^{(j)}]\,, \tag{2.6}$$

where $f^{(i)}$ ($H^{(i)}$) is the distribution (Hamiltonian) of the ith species of quasiparticles[7]. For example, the electrons in a typical metal will not only collide with other electrons, but also interact with holes, phonons and impurities, which each provide a collision integral contribution. Due to the increased complexity, coupled systems are often studied in the *relaxation time approximation*; $I^{(i)}[f^{(i)}, f^{(j)}] \approx -f^{(i)}/\tau_{ij}$, where the collision integral is replaced by a single relaxation time τ_{ij} capturing the interactions between species i and j. By Matthiessen's rule, the total relaxation time of species i,

$$\frac{1}{\tau^{(i)}} = \frac{1}{\tau_{ii}} + \sum_{j\neq i} \frac{1}{\tau_{ij}}\,, \tag{2.7}$$

receives contributions from scattering off of both the same (τ_{ii}) and different (τ_{ij}) quasiparticle species. However, the dynamics are dominated by the fastest relaxing channel (i.e., the one with the largest scattering rate), so if $\tau_{ii} \ll \tau_{ij}$, an approximate description is obtained by decoupling the ith equation from the rest. For example, impurity scattering provides the dominant pathway of momentum relaxation for electrons at low temperatures, which is why (non-superconducting) materials have a residual zero-temperature resistivity $\rho(T=0) \approx m^*/ne^2\tau_{\text{imp}}$. In this thesis, we focus on systems with dominant electron-electron interactions, and therefore restrict the kinetic equation to a single species of electron quasiparticles living in two dimensions.

2.3 The linearized kinetic equation

To study transport, the system must be perturbed from equilibrium, which can be achieved by a temperature or velocity gradient, an external force, or a voltage (affecting the chemical potential). This shifts the distribution of quasiparticles as $f = f_0 + \delta f$, where f_0 is the background distribution (2.4). We parameterize

$$\delta f = f_0(1-f_0)\chi(t; \boldsymbol{r}, \boldsymbol{p})\,, \tag{2.8}$$

[7] We can here extend the term quasiparticles to also cover bosonic excitations, as would be suitable for e.g., phonons. Such excitations can be shown to also satisfy kinetic equations, with the appropriate sign flips in Eqs. (2.3)–(2.5) [71, 76].

such that $\chi(t;\boldsymbol{r},\boldsymbol{p})$ can be thought of as a perturbation to the dimensionless quasiparticle energy[8]. Next, we assert the dependence

$$\chi(t;\boldsymbol{r},\boldsymbol{p}) = \chi(\boldsymbol{p})e^{-i\omega t+i\boldsymbol{q}\cdot\boldsymbol{r}}\,, \quad \beta(t,\boldsymbol{r}) = \beta + \delta\beta e^{-i\omega t+i\boldsymbol{q}\cdot\boldsymbol{r}}\,, \tag{2.9}$$

and so on for $\boldsymbol{F}, \boldsymbol{V}$ and μ. The streaming term, acting on the equilibrium distribution (2.4), contributes to linear order in perturbations with

$$\{H, f_0\} = \left(-\frac{\partial f_0}{\partial\varepsilon}\right)\left[\frac{\varepsilon-\mu}{T}\boldsymbol{v}\cdot\nabla T + m^*\boldsymbol{v}^T\boldsymbol{Q}\boldsymbol{v} + \boldsymbol{v}\cdot(\nabla\mu - \boldsymbol{F})\right]\,, \tag{2.10}$$

where[9] $Q_{ij} = \partial_{(i}V_{j)}$ is the so-called rate-of-strain tensor [71], we assume $\varepsilon = \varepsilon(\boldsymbol{p})$, and take $\boldsymbol{V} = 0$ on average (or perform a Galilean transformation to make it so). Finally, by defining the collision operator

$$\mathcal{L}[\chi(t;\boldsymbol{r},\boldsymbol{p})] = -\frac{I[\delta f(t;\boldsymbol{r},\boldsymbol{p})]}{f_0(1-f_0)}\,, \tag{2.11}$$

we arrive at a general form of the linearized kinetic equation

$$\beta\left(\boldsymbol{v}\cdot\boldsymbol{F} - m^*\boldsymbol{v}^T\boldsymbol{Q}\boldsymbol{v}\right) + (\partial_t + \boldsymbol{v}\cdot\nabla)\left(\beta(\varepsilon-\mu) - \chi\right) = \mathcal{L}[\chi]\,, \tag{2.12}$$

capturing the interplay between the dynamics of the quasiparticle distribution, external perturbations, and the scattering among the quasiparticles. This equation is the object of interest in Papers I and II, and we cover its solutions in the next chapter.

[8] $f_0(1-f_0) = (-k_BT\frac{\partial f_0}{\partial\varepsilon})$, so the time- and spatial derivatives act on $\beta(\varepsilon-\mu) - \chi(\boldsymbol{p})$; see (2.12) below.

[9] $X_{(\alpha\beta)} \equiv \frac{1}{2}(X_{\alpha\beta} + X_{\beta\alpha})$.

3

Electron transport

"Look at it go!"

Witch Doctor

With the linearized kinetic equation (2.12) in place, we are ready to discuss the transport properties of the electron liquid. The main challenge is the right-hand side of the equation: the linearized collision operator $\mathcal{L}[\chi]$. Section 3.2 covers the method presented in Paper I used to determine the complete spectrum of decay rates of the collision operator. We subsequently apply it to the computation of the shear viscosity of the electron liquid in Section 3.3, which is the focus of Paper II. A further discussion on the numerical implementation of the method can be found in Appendix D in Paper I.

3.1 The linearized electron-electron collision operator

In the absence of external forces, and with the temperature, chemical potential and fluid velocity kept fixed, the linearized kinetic equation (2.12) takes the form of an eigenvalue problem,

$$\mathcal{L}[\chi(\boldsymbol{p})] = \gamma\chi(\boldsymbol{p})\,, \tag{3.1}$$

where γ is the *decay* rate[1]. $\mathcal{L}$ is a positive semi-definite Hermitian operator [77], making the eigenvalues γ, which describe the relaxation of the quasielectron distribution toward local equilibrium, real and bounded from below, $\gamma \geq 0$. The lower limit is saturated for the so-called *zero modes* ($\gamma = 0$), that correspond to

[1] I.e., we consider perturbations in (2.9) that are exponentially decaying in time: $\omega = -i\gamma$ and $\boldsymbol{q} = 0$.

the conservation of particle number, momentum and energy, as will be discussed in Section 3.2.1 below.

Historically, the electron liquid was characterized by a single decay rate γ, which was inferred from transport coefficients obtained within Fermi liquid theory in the zero-temperature limit. This gives the now well-known result $\gamma \sim T^2$ in three dimensions [78–80]. In two spatial dimensions, the constrained phase space leads to a logarithmic enhancement $\gamma \sim T^2 \ln(T_F/T)$ [66, 81–84][2].

The notion of a single decay rate of the entire electron liquid is however oversimplified, as there exists an entire spectrum of decay rates in (3.1). Only if this spectrum is dominated by a single (non-zero) decay rate γ much smaller than the rest will such a notion be valid, and as highlighted in Paper I, this is indeed not the case in two spatial dimensions[3]. This limits the applicability of diagrammatic approaches that determine a decay rate via the quasielectron self-energy as $\gamma \approx -\operatorname{Im}\Sigma$ [66, 83, 84]. Additionally, (2.12) implies that it is the collective relaxation of the quasielectron distribution, and not that of a single electron quasiparticle, that governs transport. For instance, the logarithmic temperature enhancement of the quasielectron self-energy in two dimensions does not translate to the shear relaxation rate, as we show in Paper II and in Section 3.3 below. A proper understanding of transport therefore requires access to the full spectrum of the collision operator, which may be obtained through a matrix representation of the kinetic equation.

3.1.1 Matrix representation

The crucial step for turning the kinetic equation into a concrete linear algebra problem is the introduction of an inner product naturally induced by the collision integral,

$$\langle \chi' | \chi \rangle = \lambda_T^2 \int \frac{\mathrm{d}^2 \boldsymbol{p}}{(2\pi)^2} \bar{\chi}'(\boldsymbol{p}) f_0(\boldsymbol{p})(1 - f_0(\boldsymbol{p}))\chi(\boldsymbol{p})\,. \tag{3.2}$$

Matrix elements of the linearized collision operator with respect to this inner product then read

$$\langle \psi | \mathcal{L} | \chi \rangle = \frac{\lambda_T^2}{4} \int \frac{\mathrm{d}\boldsymbol{p}_1\, \mathrm{d}\boldsymbol{p}_2\, \mathrm{d}\boldsymbol{p}_1'\, \mathrm{d}\boldsymbol{p}_2'}{(2\pi)^8} W_{121'2'} F_{121'2'} \left[\sum_i{}' \psi(\boldsymbol{p}_i) \right] \left[\sum_i{}' \chi(\boldsymbol{p}_i) \right], \tag{3.3}$$

where the scattering matrix element $W_{121'2'} = W(\boldsymbol{p}_1\boldsymbol{p}_2|\boldsymbol{p}_1'\boldsymbol{p}_2')$ enforces momentum and energy conservation, $F_{121'2'} = f_0(\boldsymbol{p}_1) f_0(\boldsymbol{p}_2)(1 - f_0(\boldsymbol{p}_1'))(1 - f_0(\boldsymbol{p}_2'))$ is the product of Fermi factors, and $\sum_i' x_i = x_1 + x_2 - x_1' - x_2'$.

[2] The restriction to one spatial dimension has even more radical consequences, and leads to the Tomonaga-Luttinger liquid [41].

[3] This was recently shown to also be the case in three dimensions, although the effect is not as large [85].

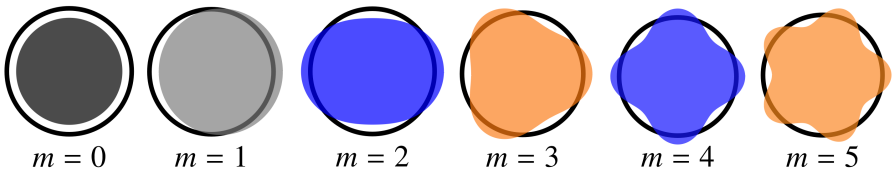

Figure 3.1: An expansion of the Fermi surface deformation $\chi(\boldsymbol{p})$ into angular harmonics labeled by a mode number m. The black circle is the Fermi energy for electrons with a parabolic dispersion $\varepsilon(\boldsymbol{p}) = \hbar^2\boldsymbol{p}^2/2m^*$.

From this point on, we will assume the material to have a parabolic band dispersion $\varepsilon(\boldsymbol{p}) = \hbar^2\boldsymbol{p}^2/2m^*$, with m^* the effective quasielectron mass. The Fermi surface is therefore circular, so the perturbation χ may be expanded into angular harmonics as

$$\chi(\boldsymbol{p}) = \sum_m \chi(p)e^{im\theta}\,, \tag{3.4}$$

with θ the polar angle on the Fermi surface. Figure 3.1 illustrates the first few Fermi surface deformations for constant $\chi(p)$, which may be thought of as a rigid deformation in the chemical potential[4]. The angular mode number m dictates the behavior of the deformations under parity $\boldsymbol{p} \to -\boldsymbol{p}$: modes with m even are even-parity, whereas modes with m odd are odd-parity. Modes of different angular mode numbers m are orthogonal with respect to the inner product (3.2), making the full matrix $\langle\psi|\mathcal{L}|\chi\rangle$ block diagonal, with blocks $\mathcal{L}^{(m)} = \langle\psi e^{im\theta}|\mathcal{L}|\chi e^{im\theta}\rangle$ that may be treated separately.

The inner product (3.2) allows for a basis of orthogonal polynomials $\{T_n(p)\}$ to be generated (e.g., by a Gram-Schmidt procedure), whereby the radial part of the perturbations can be expanded as

$$\chi(p) = \sum_{n=1}^{N} T_n(p)\,, \tag{3.5}$$

up to an upper basis dimension N. Here, the lowest order, constant basis polynomial $T_1(p)$ corresponds to a rigid deformation of the Fermi surface. Higher-order, momentum-dependent polynomials incorporate the effects of finite energy transfer, and have a larger influence at higher temperatures as the broadening of the Fermi surface increases. From the collision operator matrix elements $\langle T_n|\mathcal{L}^{(m)}|T_{n'}\rangle$, one obtains a spectrum of N eigenvalues $\gamma_m^{(1)} \leq \cdots \leq \gamma_m^{(N)}$. Since $\mathcal{L}$ is a positive semi-definite Hermitian operator, the Rayleigh-Ritz principle guarantees that the eigenvalues converge from above as the basis dimension N is increased [86].

[4]The illustrations in Figure 3.1 therefore correspond to zero temperature (when the Fermi-Dirac distribution is a step function). Momentum-dependence in $\chi(p)$ captures the softening of the Fermi surface at finite temperature, which would blur the edges of the deformations in the figure.

The numerical challenge of solving the linearized kinetic equation thus lies in the evaluation of the matrix elements $\langle T_n|\mathcal{L}^{(m)}|T_{n'}\rangle$, which are multidimensional integrals that at low temperatures feature highly peaked integrands due to the Fermi factors in the collision integral. To this end, we use the adaptive *Divonne* algorithm within the Cuba library [87], as it allows for a Monte Carlo sampling of the integrand to be biased toward the peaked regions. This formulation makes it possible to numerically characterize the eigenmode spectrum, as was first demonstrated in [33] using a constant interaction matrix element. In Paper I, we generalize this to a screened Coulomb interaction in order to connect more directly with realistic experimental systems.

3.1.2 The screened Coulomb interaction

The scattering element in (3.3) is within a Golden-Rule approximation given by

$$W(\boldsymbol{p}_1', \boldsymbol{p}_2'|\boldsymbol{p}_1\boldsymbol{p}_2) = \frac{2\pi}{\hbar}\left|\langle \boldsymbol{p}_1\boldsymbol{p}_2|V|\boldsymbol{p}_1'\boldsymbol{p}_2'\rangle\right|^2 (2\pi)^2 \delta\left(\sum_i{}' \boldsymbol{p}_i\right)\delta\left(\sum_i{}' \varepsilon_i\right), \tag{3.6}$$

where the delta functions ensure conservation of momentum and energy. Here, we consider a screened Coulomb interaction, acting through both direct and exchange channels[5]

$$\left|\langle \boldsymbol{p}_1\boldsymbol{p}_2|V|\boldsymbol{p}_1'\boldsymbol{p}_2'\rangle\right|^2 = \underbrace{V^2(\boldsymbol{p}_1' - \boldsymbol{p}_1) + V^2(\boldsymbol{p}_1' - \boldsymbol{p}_2)}_{\text{direct}} - \underbrace{V(\boldsymbol{p}_1' - \boldsymbol{p}_1)V(\boldsymbol{p}_1' - \boldsymbol{p}_2)}_{\text{exchange}}, \tag{3.7}$$

where

$$V(\boldsymbol{q}) = \frac{2\pi e^2}{q + k_{\mathrm{TF}}}, \tag{3.8}$$

and $k_{\mathrm{TF}} = 2e^2 m^*/\hbar^2$ is the Thomas-Fermi wave vector. The contributing diagrams are shown in Figure 3.2. This potential is obtained from the static ($\omega \ll q v_F$) limit of the dielectric function $\varepsilon(\omega, \boldsymbol{q})$ computed within the random phase approximation (RPA) as $V(\boldsymbol{q}) = V_0(\boldsymbol{q})/\varepsilon(\omega = 0, \boldsymbol{q})$, where $V_0(\boldsymbol{q})$ is the bare Coulomb interaction. This relates the Thomas-Fermi wave vector to the RPA density parameter r_s as $k_{\mathrm{TF}} = 2r_s\sqrt{\pi n}$, where $n = 2T_F/T\lambda_T^2$ is the density of the electron gas. The parameter r_s can be thought of as the radius of the volume containing on average one electron, where a larger value implies stronger correlations between the electrons due to the decreased screening [72]. While the RPA expansion is strictly valid only for $r_s < 1$, it empirically works well for most metals, where $r_s \sim 3 - 6$ [88].

The most pertinent critique of the choice of interaction element is the neglect of a finite energy transfer ω, that can be important at large temperatures. Generalizing (3.8) to include the finite-temperature Lindhard function $\Pi(\omega, \boldsymbol{q}; T)$

[5] This is essentially Møller scattering, so the s-channel process is forbidden as there is no photon carrying charge $2e$.

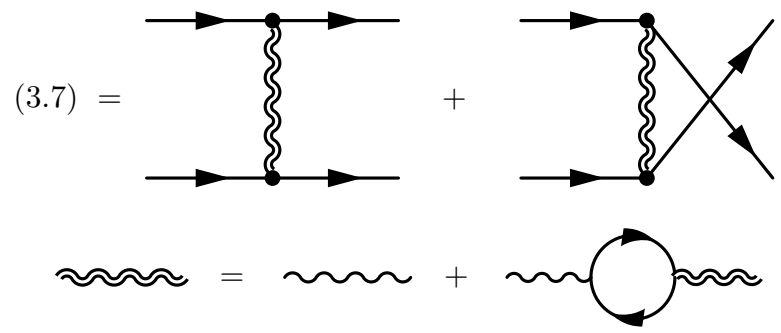

Figure 3.2: Direct and exchange-channel diagrams for the Coulomb interaction $\langle \boldsymbol{p}_1 \boldsymbol{p}_2 | V | \boldsymbol{p}_1' \boldsymbol{p}_2' \rangle$ (top). The RPA approximation of the Coulomb interaction is the sum over all ring-diagrams (bottom). In the static limit $\omega \ll q v_F$, it takes the form of the Thomas-Fermi screened interaction in (3.8).

would involve an additional integral at every point of the integrand [41], slowing down the computations. However, in the case of the shear viscosity of the electron liquid discussed in Section 3.3 and in Paper II, only the first few basis polynomials enter the calculation. The shear viscosity is therefore primarily governed by processes with small energy transfer, justifying this approximation. A second approximation is the use of the Golden rule expression in (3.6), which technically corresponds to a first-order Born approximation estimating the transition T-matrix as $T \approx V$, valid for weak scattering potentials V [89]. While the RPA-screened interaction incorporates higher-order screening effects (cf. Figure 3.2), it does not resum higher-order scattering processes in the T-matrix; however, screening reduces the effective interaction strength, making the Born approximation more reliable.

3.2 Mode spectrum of the electron liquid

With a concrete interaction matrix element, the method detailed in Section 3.1.1 can be employed to obtain a complete solution of the spectrum of the two-dimensional electron liquid. This results in a description that, at linear order and in the absence of other scattering species, is exact and valid at all temperatures. Paper I obtains the full spectrum of modes associated with the eigenvalue problem in (3.1), whose main features are summarized below.

3.2.1 Zero modes and hydrodynamics

Some eigenvalues of the collision operator vanish identically due to the underlying symmetries of the electron liquid. In particular, the electron-electron interaction (3.6) conserves particle number, momentum and energy. In the language of (3.4), the zero modes of particle number and energy correspond to $\chi(p) \sim 1$

and $\chi(p) \sim p^2$ in the $m = 0$ sector, respectively, captured in a breathing mode (black deformation in Figure 3.1). The two conserved components of the total momentum are linear combinations of $\chi(\boldsymbol{p}) \sim pe^{\pm i\theta}$ in $m = \pm 1$, captured by rigid shifts of the quasiparticle distribution (gray deformation in Figure 3.1).

In a regime where all other decay rates $\gamma' \neq 0$ are parametrically large compared to the scales of interest — for instance, for slow dynamics with $\omega \ll \gamma'$ — all non-conserved modes relax rapidly. The dynamics is then governed by the conserved quantities, whose evolution is constrained by conservation laws [70]

$$\frac{\partial n}{\partial t} + \partial_i(nV^i) = 0\,, \quad \frac{\partial(nV^i)}{\partial t} + \partial_j \Pi^{ij} = 0\,, \tag{3.9}$$

and the conservation of energy. To close the system of equations, one must specify constitutive relations, such as

$$\Pi_{ij} = -P\delta_{ij} + \eta\,(2Q_{ij} - \nabla \cdot \boldsymbol{V}\delta_{ij}) + \zeta(\nabla \cdot \boldsymbol{V})\delta_{ij}\,, \tag{3.10}$$

which expresses the stress tensor Π_{ij} in terms of the hydrodynamic fields and their gradients, with coefficients set by the shear and bulk viscosities η and ζ, and the pressure P. These are the equations of hydrodynamics, corresponding to a projection of the kinetic theory onto the subspace spanned by the zero modes of the collision operator, as in a Chapman-Enskog expansion [90, 91].

In a realistic system, momentum and energy conservation are broken by e.g., impurity or phonon scattering[6]. Nevertheless, the same logic applies: if the symmetry breaking is weak enough, hydrodynamics provides an approximate description on scales $\omega \ll \gamma_{\text{sym. break.}}$ [76].

Hydrodynamics is most readily realized when electron-electron scattering is sufficiently rapid to establish local equilibrium. This typically occurs at temperatures approaching T_F, where thermal broadening weakens the Pauli blocking that suppresses scattering at low temperatures, while the electron gas still remains degenerate. The hydrodynamic regime is therefore concomitant with a strongly interacting electron liquid. Importantly, hydrodynamics itself does not rely on quasiparticles, and extends to systems with even stronger correlations. We will return to this in Chapter 5.

3.2.2 Higher-order modes and the tomographic regime

Aside from the two lowest modes in the $m = 0$ sector and lowest modes in the $m = \pm 1$ sectors, the remaining modes have a finite lifetime. A complete analysis of the spectrum is presented in Paper I, and we focus here on the main physical effect, which is summarized in Figure 3.3. Panel (a) shows the eight lowest-lying decay rates $\gamma_m^{(n)}, n = 1, \ldots 8$, for $0 \leq m \leq 20$, of the collision operator at a low temperature $T = 0.001T_F$.

[6] The lattice-induced breaking of translational symmetry from continuous to discrete is discussed further in Section 5.3.

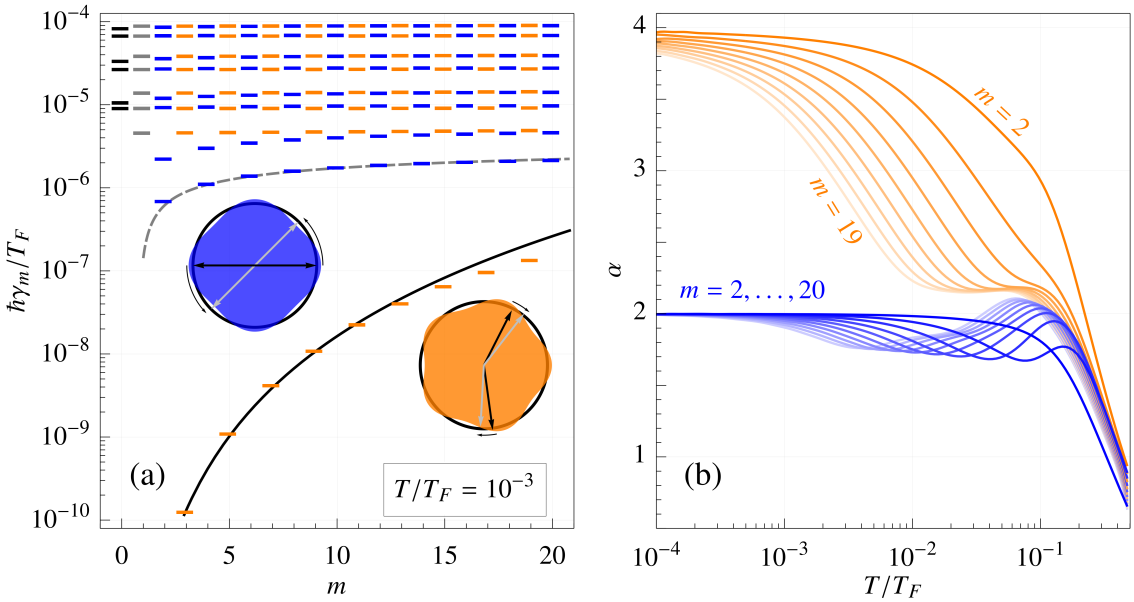

Figure 3.3: (a) Hierarchy of eigenmodes of the collision operator (3.3) at a low temperature $T = 10^{-3}\,T_F$. There is a separation by several orders of magnitude between the lowest-lying odd-parity modes and the rest of the spectrum. The dashed gray and solid black line correspond to (3.11) and (3.12), respectively. Insets: examples of scattering processes for even and odd modes at low temperature. (b) Temperature scaling exponents α for the lowest-lying modes of angular mode number $2 \leq m \leq 20$. Reproduced from Paper I [77]. In both figures, the density parameter $r_s = 1$.

The most striking behavior is the pronounced separation between the lowest-lying odd-parity (orange) modes and the rest. The origin of this hierarchy lies in the kinematics of low-temperature scattering [29]. As $T \to 0$, all participating states in a scattering process are confined to a narrow region around the Fermi surface, strongly restricting the available phase space. Only head-on collisions, with incoming momenta diametrically opposed on the Fermi surface, satisfy the conservation of both momentum and energy as $T \to 0$ while also relaxing the distribution toward equilibrium. Such scattering events are favored for even-parity Fermi surface deformations, which have an excess of quasiparticles on opposite sides [cf. left inset in Figure 3.3(a)]. For this reason, the decay rates of odd-parity deformations instead become suppressed. They must rely on the small broadening of the Fermi surface at finite T to relax by successive small-angle scattering, which reduces the odd-parity decay rate [cf. right inset in Figure 3.3(a)]. This mechanism also leads to a strong m-scaling in the odd modes, which may be viewed as a form of angular superdiffusion along the Fermi surface [30].

This separation, which can be seen in Figure 3.3(b) to extend up to $T \approx 0.1T_F$, has been dubbed the "odd-even effect" and can give rise to a new tomographic transport regime in between the limits of ballistic and hydrodynamic

flow [29, 31]. It is realized when most modes decay sufficiently quickly for hydrodynamics to otherwise provide an approximate description, but where the long-lived, odd-parity, non-hydro modes still appreciably influence transport. The effective description is therefore a kind of extended, "suprahydrodynamics[7]" [38]. Importantly, Paper I shows that this large separation between decay rates applies only to the lowest-lying odd modes. The set of parametrically long-lived modes is therefore finite, while the remainder of the spectrum continues to relax at conventional rates. Hydrodynamics thus still provides an approximate description, albeit one modified by a small number of additional long-lived modes.

Another important result concerns the role of the Coulomb interaction. By analytically evaluating $\langle\psi^\star|\mathcal{L}|\psi^\star\rangle$ for a lowest order basis element $\psi^\star$, we obtain an approximation of the lowest-lying even modes at low temperatures and $r_s \gtrsim 1$ as[8]

$$\gamma_{m\ \mathrm{even}} \approx \frac{2\pi}{3\hbar}\frac{T^2}{T_F}r_s^2\left[\log\left(1+\frac{\sqrt{2}}{r_s}\right)-\frac{\sqrt{2}}{\sqrt{2}+r_s}\right]\frac{\ln m\phi}{\ln 2\phi}\,, \tag{3.11}$$

where ϕ is a fit parameter partially absorbing the small error of using a single lowest order basis element. Equation (3.11) is shown as a dashed gray line in Figure 3.3, where $\phi = 1.23$. The lowest-lying odd modes are instead approximately given by

$$\gamma_{m\ \mathrm{odd}} = \frac{4\pi^3 T_F}{15\hbar}\left|V^\star(r_s)\right|^2\left(\frac{T}{T_F}\right)^\alpha m^4, \tag{3.12}$$

where $|V^\star(r_s)|^2$ is the Coulomb matrix element evaluated at a small momentum transfer $q \approx 0.2k_F$ and the scaling exponent α, shown in Figure 3.3(b), asymptotes to 4 in the low-temperature limit. Equation (3.12) is shown as a solid black line in Figure 3.3.

Aside from the drastically different temperature scaling, a major difference between (3.11) and (3.12) is their dependence on the RPA density parameter r_s. While the matrix element $|V^\star(r_s)|^2$ controlling the odd modes varies only weakly with r_s, the even-parity decay rates show a much stronger dependence, as seen in (3.11). As discussed in Paper I, this difference originates from the underlying scattering mechanisms: when r_s is decreased, small angle scattering becomes increasingly favored, which strongly reduces the relaxation of even-parity modes. Odd-parity modes, by contrast, already relax through repeated small-angle scattering and are therefore much less affected by changes in r_s.

[7] Similar extended hydrodynamics are known as "hydro+" in the QCD community [92], or "quasihydro" within holography [93].

[8] While these modes display the expected T^2/T_F-scaling, they exhibit a logarithmic dependence on the angular mode number m (up to $m \lesssim \sqrt{T_F/T}$). This may be contrasted with the logarithmic-in-temperature scaling seen in self-energy calculations [66], but such approaches are oblivious to the symmetries of different Fermi surface deformations.

The upshot is that the separation between the lowest-lying even and odd modes can be experimentally tuned by changing the density parameter r_s, for instance through doping or by modifying the dielectric environment. Magnetic fields provide an additional handle: by explicitly breaking parity, they alter the structure of the odd-even hierarchy and may enable direct measurements of the even and odd lifetimes [36, 37, 40, 94].

Any transport property that couples to the odd-parity sector will show clear signatures of the tomographic regime. Predicted phenomena include novel charge-neutral modes [32], fractional-power flow profiles [31], and anomalous scaling of the non-local conductivity [95, 96]. Furthermore, the odd-parity modes have a large effect on nonlinear transport [34], and have been shown to explain the "superballistic paradox" [39], where experiments observe a decrease of resistivity with increasing temperature down to temperatures below the applicability of hydrodynamics. The odd-even effect has also been investigated in other fermionic systems, such as cold atoms [35], which signals that the effect is universal.

3.3 Shear viscosity of the electron liquid

With the ability to completely characterize the behavior of the collision operator $\mathcal{L}$, the extension to the full linearized kinetic equation (2.12) is simply that of a linear algebra problem. A host of transport coefficients and response functions can be analyzed depending on which sources are turned on, such as external forces (e.g., electric fields), temperature gradients, or the rate-of-strain tensor. Here, and in Paper II, we focus on the *shear viscosity*, which quantifies momentum transport in the hydrodynamic regime.

Consider the flow of electrons through a channel of width W at a temperature where phonons can be neglected, as illustrated in Figure 3.4. Electron-electron scattering defines a momentum-conserving length scale $\ell_{ee} = v\gamma_{ee}^{-1}$, with v the typical velocity of the electrons. Impurity or disorder scattering is similarly associated with a momentum-relaxing length scale ℓ_d. When $\ell_d \ll W \ll \ell_{ee}$, electron-electron interactions are negligible and transport is governed by impurity scattering, resulting in a diffusive (Ohmic) regime [5]. Here, one can imagine the electrons as balls in a pinball machine hitting against bumpers (the impurities) that relax the momentum of the electrons. The resistivity, related to the momentum dissipation of the charge-carrying electrons, is therefore governed by the rate of impurity scattering.

Advances in fabrication techniques have enabled ultra-clean two-dimensional materials with very weak impurity scattering [11]. Sufficiently small devices can therefore realize the hierarchy $W \ll \ell_{ee}, \ell_d$. In this ballistic regime, the electrons follow nearly straight trajectories and primarily scatter off the boundaries, resulting in a resistivity determined mainly by the device geometry. Even more

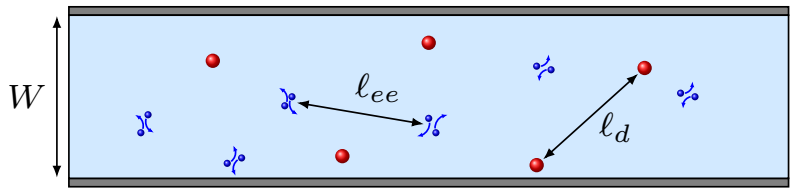

Figure 3.4: The electron fluid flowing through a channel of width W. The length scale set by electron-electron scattering (blue) is ℓ_{ee}, whereas the length scale set by scattering off impurities or disorder (red) is ℓ_d. If $\ell_{ee} \ll W \ll \ell_d$, the fluid enters a hydrodynamic regime, where the resistivity is set by the shear viscosity.

interesting is when the electron-electron interactions become strong enough that $\ell_{ee} \ll W \ll \ell_d$ [5]. This causes hydrodynamic flow, where frequent electron-electron interactions establish local equilibrium and conserve momentum locally, while global momentum relaxation still mainly occurs at the boundaries. This results in a boundary drag that causes the fluid to develop a parabolic profile as it flows through the channel, and is one of the experimental signatures of hydrodynamic flow [19, 27]. In this setting, the total resistivity is affected by the efficiency of momentum transport across the fluid, captured by the shear viscosity.

Intriguingly, the stronger the interactions between the electrons — i.e., a larger γ_{ee} — the lower the resistance. This contrasts sharply with the diffusive regime, where the resistance is governed by electron-impurity scattering, but can be understood intuitively as a smaller ℓ_{ee} making it harder for the electrons to find the boundaries. Since $\gamma_{ee} \sim T^2/T_F$, this also leads to a *decrease* in the resistivity with increased temperature, which is known as the Gurzhi effect [13].

3.3.1 Shear viscosity from the kinetic equation

To determine the shear response, consider the *gedankenexperiment* of applying a force along one of the edges of the channel through which the fluid flows [70]. This causes a spatially varying velocity profile perpendicular to the direction of the force, as illustrated in Figure 3.5, captured mathematically in a non-zero stress tensor $\Pi_{ij} = -nm^* \langle v_i v_j \rangle$. By perturbing the system within linear response with a wave vector perpendicular to the fluid velocity ($\nabla \cdot \boldsymbol{V} = 0$), the shear viscosity may be obtained as the proportionality coefficient between the stress and rate-of-strain tensors through the decomposition (3.10) as

$$\eta = -\frac{nm^*}{2Q_{xy}} \langle v_x v_y \rangle = -\frac{m^*}{2Q_{xy}} \int \frac{\mathrm{d}^2 \boldsymbol{p}}{(2\pi)^2} v_x v_y \delta f(\boldsymbol{p}) \,. \tag{3.13}$$

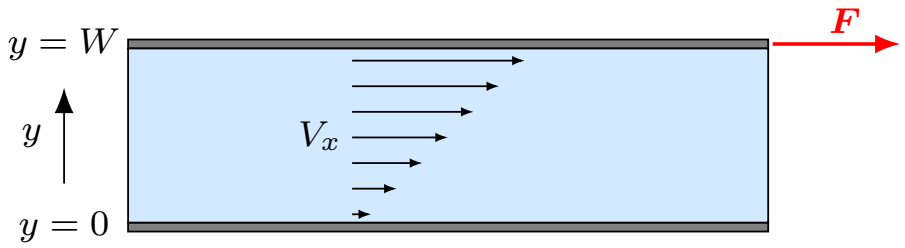

Figure 3.5: A fluid (blue) between two plates (gray) experiencing shear stress. By applying a force $\boldsymbol{F}$ to the upper plate, the fluid develops a velocity gradient $V_x(y)$. The shear viscosity is the proportionality constant between the force (per unit area) and the gradient of the fluid velocity, effectively determining the rate of momentum loss. Image adapted from [70].

Expressed in the basis $|nm\rangle = |T_n e^{im\theta}\rangle$ generated by the inner product (3.2), this becomes

$$\frac{\eta}{\hbar n} = \frac{m^{*2}}{\hbar k_B T_F} \langle v_x v_y | (\mathcal{L} - i\omega + i\boldsymbol{v}\cdot\boldsymbol{q})^{-1} | v_x v_y \rangle \,, \tag{3.14}$$

where we introduced the vector

$$|v_x v_y\rangle = \langle nm | v_x v_y \rangle = \frac{\lambda_T^2}{2} \int \frac{\mathrm{d}\boldsymbol{p}}{(2\pi)^2} \bar{T}_n(p) e^{-im\theta} v^2 \sin 2\theta \chi(p) \propto \delta_{m,2} \,. \tag{3.15}$$

Note that $\eta(\omega, \boldsymbol{q} = 0)$ is entirely determined by the dynamics of the quadrupole $m = 2$ mode[9], due to the orthogonality of angular harmonics. Figure 3.6(a) shows the zero-momentum, static shear viscosity for $r_s = 0.5, 1$ and 3, which in a Fermi liquid is related to the relaxation time of shear stress τ_η as $\eta = P\tau_\eta$. Equation (3.15) implies that $\tau_\eta \sim \gamma_{m=2}^{-1}$, making the shear viscosity controlled by the relaxation of the $m = 2$ angular harmonic — a collective mode — and not the quasielectron lifetime τ_{ee} obtained from the self-energy. The pressure asymptotes to the constant value $P = nE_F/2$ at low temperatures and the ideal gas pressure $P = (T/T_F)nE_F$ at high temperatures, which together with

$$\begin{cases} \gamma_{m=2} & \sim (T/T_F)^2, \quad T \ll T_F \,, \\ \gamma_{m=2} & \sim (T/T_F)^{-1}, \quad T \gg T_F \,, \end{cases} \tag{3.16}$$

leads to a diverging shear viscosity at both low and high temperatures. In particular, the viscosity attains a minimum at intermediate temperatures, where electron-electron scattering is strongest and a hydrodynamic description is most appropriate.

[9] The term $i\boldsymbol{v}\cdot\boldsymbol{q}$ in (3.14) is not a diagonal matrix in m-space, so a finite $\boldsymbol{q}$ introduces a coupling to other modes. The same story applies to e.g., the conductivity. This also makes the inversion in (3.14) well-defined for $\omega, \boldsymbol{q} = 0$, as the zero mode subspace does not contribute.

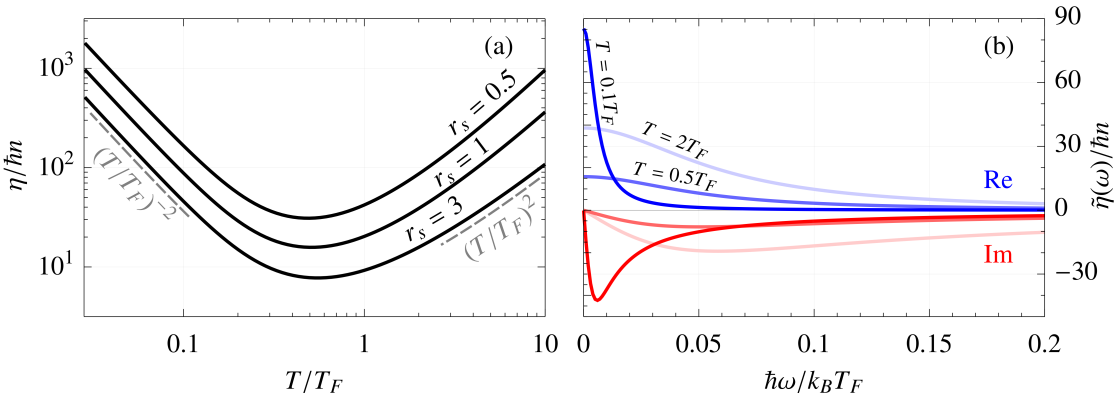

Figure 3.6: (a) Static shear viscosity for $r_s = 0.5, 1, 3$. It attains a minimum at temperatures near the Fermi temperature T_F. (b) Frequency dependent shear viscosity at three different temperatures for $r_s = 1$. The real parts are shown in blue and the imaginary parts in red. Lighter colors indicate a higher temperature.

The famous Kovtun-Son-Starinets (KSS) bound postulates that $\eta/s \geq \hbar/4\pi$ for a relativistic system, where s is the entropy density [97]. For the non-relativistic system considered here, $\eta/s \sim E_F/\gamma$, so a saturation of the KSS bound would imply $E_F \sim \hbar\gamma$, signaling a breakdown of the quasiparticle description. The electron liquid would then enter a strongly correlated regime more aptly described by the methods presented in Part II of this thesis. For the two-dimensional electron liquid interacting through the screened Coulomb interaction (3.7), we find that the minimum is larger than the KSS bound by at least a factor of 50, so the quasiparticle description remains valid.

At finite frequency, the shear viscosity can be expressed as a complex-valued function [98]

$$\tilde{\eta}(\omega) = \frac{P\tau_\eta}{1 - i\omega\tau_\eta}, \quad P = -n\varepsilon_F \left(\frac{T}{T_F}\right)^2 \mathrm{Li}_2(-e^{\beta\mu}), \tag{3.17}$$

describing the viscoelastic response. The real and imaginary parts of the complex shear viscosity $\tilde{\eta}(\omega)$ are shown in Figure 3.6(b) for three different temperatures at $r_s = 1$. At low temperatures, the real part is sharply peaked at zero frequency, signaling that the system behaves hydrodynamically only in the narrow window $\omega\tau_\eta \ll 1$. The response is therefore predominantly reactive (elastic) rather than dissipative. For temperatures near T_F, on the other hand, there is a significant broadening of the response function, highlighting that the stress response is governed by a single hydrodynamic parameter — the shear viscosity $\eta \sim P\tau_\eta$ — up to energies $\hbar\omega$ that are a sizable fraction of the Fermi energy. This corresponds to the hydrodynamic regime, enabled by the enhanced electron-electron scattering near T_F.

Part II
Non-Fermi liquids and holography

4
Holography

"If light cannot escape me, what hope have you?"

Enigma

In this chapter, we move beyond quasiparticle-based descriptions of metallic transport, and turn to holography, a framework that provides controlled access to strongly interacting quantum matter without well-defined quasiparticles. A detailed discussion on the use of holographic methods for strongly correlated systems can be found in Refs. [54, 55, 99], and we focus here on the essentials needed for Papers III–V. In this and the following chapters, we adopt units where $c = \hbar = k_B = 1$.

4.1 The holographic duality

Holography is a duality between a quantum field theory (QFT) and a gravitational theory living in a higher dimension. The term reflects how higher-dimensional information is encoded in a lower dimension, loosely analogous to an optical hologram. It emerged from the "AdS/CFT correspondence" in what is widely regarded as one of the most influential papers in theoretical physics in the last three decades [100], where Maldacena conjectured that $\mathcal{N} = 4$ super Yang-Mills theory admits a dual description as type IIB string theory on $\mathrm{AdS}_5 \times S^5$. In the large-$N$ limit, where N is the number of colors of the gauge theory, together with the limit of large 't Hooft coupling, $\lambda = g_{YM}^2 N \to \infty$, the duality reduces to that between a strongly coupled, conformal quantum field theory (CFT) and weakly coupled, classical (super)gravity. This strong/weak aspect underpins the usefulness of the duality, since it allows otherwise intractable strongly correlated quantum dynamics to be mapped to classical gravity, where calculations are feasible.

As indicated by the name of the original correspondence, the relevant gravitational backgrounds of interest are most often asymptotically anti-de Sitter (AdS) spacetimes, which are solutions of Einstein's equations with a negative cosmological constant. The isometry group of AdS_{D+1} coincides with the conformal group $\mathrm{SO}(2, D)$ in D dimensions, which underlies the correspondence. AdS space also exhibits the peculiar property that light-like paths reach spatial infinity in a finite coordinate time, which makes the boundary an essential part of the geometry. One can therefore interpret the dual CFT as living on the lower-dimensional asymptotic boundary of the so-called *bulk* AdS spacetime.

The extra dimension of the bulk theory geometrizes the RG flow of the boundary theory, where the asymptotic AdS region encodes the ultraviolet (UV) physics, while the deep interior determines the infrared (IR). At finite temperature, the bulk geometry develops a black hole[1], which governs the infrared dynamics of the dual theory. The thermal scale breaks the conformal invariance in the infrared, and the horizon provides a natural mechanism for dissipation. Furthermore, the characteristic dissipative relaxation timescales are often Planckian [54], which makes holography especially appealing for the description of the strongly correlated strange metals.

While the original AdS/CFT correspondence was formulated in a so-called top-down perspective, where one starts from a full string theory, one can instead work with effective bulk theories containing only the fields and symmetries relevant for the observables of interest [54]. We adopt this "bottom-up" approach[2] throughout this thesis.

Holographic models should not be interpreted as microscopic descriptions of specific materials. They rely on large-N limits and (very) strong coupling, and neglect detailed atomic structure and weakly coupled quasiparticle sectors. The main value lies instead in revealing universal features of strongly correlated systems that are insensitive to microscopic details. Nevertheless, in order to approach modeling a realistic system, a handful of salient features need to be incorporated. Modern holographic bottom-up models are indeed able to capture many such features, including compressible states at finite density [54, 55], broken translational symmetry [101, 102], fermionic spectral structure [103–105], and long-range Coulomb interactions [106–109]. We will discuss some of these in more detail in this and the following chapters.

4.1.1 The dictionary

The duality becomes useful through a holographic dictionary, which specifies how operators, sources, and thermodynamic quantities in the boundary theory are encoded in bulk fields and geometry. The boundary quantum field theory

[1] Technically these are black *branes*, but we will simply refer to them as black holes here.

[2] Many commonly used holographic bottom-up models can in fact be embedded in consistent truncations of a full string theory [55].

is described by the generating functional

$$Z_{\mathrm{QFT}}[h(x)] \equiv \int \mathcal{D}\Phi \, e^{i \int \mathrm{d}^{d+1}x \, [\mathcal{L} + h(x)\mathcal{O}(x)]} \,, \tag{4.1}$$

where Φ denotes the degrees of freedom of the theory and $\mathcal{L}$ is the Lagrangian. By coupling an operator $\mathcal{O}(x)$ to a source $h(x)$, the n-point functions $\langle \mathcal{O}\mathcal{O} \ldots \rangle$ can be obtained through successive functional derivatives with respect to $h(x)$.

The central statement of the duality is that this functional equals the partition function of the bulk gravitational theory, which is captured in the Gubser-Klebanov-Polyakov-Witten (GKPW) formula [110, 111]

$$Z_{\mathrm{QFT}}[h(x)] = Z_{\mathrm{Grav}}[h(x)] \equiv \int^{\phi \to h} \mathcal{D}\phi \, e^{i S_{\mathrm{Grav}}[\phi]} \,. \tag{4.2}$$

The source $h(x)$ is on the gravitational side identified with the value of the bulk field ϕ dual to the operator $\mathcal{O}$ at the asymptotic AdS boundary, which is here schematically represented as $\phi \to h$. In the limit of large 't Hooft coupling, stringy gravity in the bulk reduces to classical gravity. The bulk partition function can then be evaluated on the classical saddle

$$Z_{\mathrm{Grav}}[h(x)] \approx e^{i S_{\mathrm{Grav}}[\phi^*]} \,, \tag{4.3}$$

where ϕ^* denotes the solutions of the bulk equations of motion subject to the boundary condition $\phi \to h$. Once the bulk equations of motion are solved, the GKPW formula (4.2) means that the boundary n-point functions can be obtained from successive functional derivatives of the bulk on-shell action as

$$\langle \mathcal{O}(x_1) \ldots \mathcal{O}(x_n) \rangle = \frac{\delta^n S_{\mathrm{Grav}}[\phi^*]}{\delta h(x_1) \ldots \delta h(x_n)} \,. \tag{4.4}$$

The difficult problem of computing observables in a strongly interacting quantum many-body system is thus recast as a classical boundary-value problem in gravity.

The dictionary then specifies which bulk object corresponds to which boundary operators and observables[3]. Some entries relevant to this thesis include

1. The bulk metric $g_{\mu\nu}$ is dual to the boundary stress-energy tensor $\mathcal{T}^{\mu\nu}$,
2. A bulk $U(1)$ gauge field A_μ corresponds to a conserved $U(1)$ current $\mathcal{J}^\mu$ on the boundary,
3. The regularized Euclidean gravitational on-shell action corresponds to the free energy of the dual theory.

[3]It is in general not trivial to identify which field corresponds to what operator, but they must share symmetry properties, which greatly restricts the number of possible options.

The current-current and density-density correlators, which determine the optical conductivity and the collective longitudinal charge response, respectively, play a central role in this thesis. A famous application is the 2-point stress tensor correlator $\langle \mathcal{T}_{xy} \mathcal{T}_{xy} \rangle$, which we saw in Section 3.3 to determine the shear viscosity. It led Kovtun, Son, and Starinets (KSS) to conjecture the lower bound $\eta/s \geq \hbar/4\pi$ [97], where s is the entropy density. Such a low viscosity is a telltale sign of strongly correlated physics, and has been observed in the quark-gluon plasma created by colliding nuclei at high energies [112]. While the original bound is violated in some holographic models [113], it remains a paradigmatic example of near-perfect fluidity at strong coupling. Effective hydrodynamic descriptions of holographic transport will be discussed in Section 5.3.

4.2 Quantum criticality

Since holography originated in high-energy physics, it is natural to ask why it should apply to condensed matter systems, which at first sight seem far removed from anything relativistic or conformal. The key point is that many-body physics is often governed by emergent infrared descriptions largely independent of microscopic details, such as the Fermi liquid discussed in Part I. For instance, the low-energy theory of charge-neutral graphene consists of Dirac cones at distinct points in the Brillouin zone, and is effectively relativistic with the speed of light replaced by the Fermi velocity, $c \to v_F$ [114]. Likewise, we know from the classical theory of phase transitions that a system at criticality exhibits both scale invariance and universality [115].

The latter is particularly relevant in the context of quantum phase transitions, which occur at zero temperature as a non-thermal parameter g is tuned to a critical value g_c, and where quantum rather than thermal fluctuations act as the driving mechanism [115]. The vicinity of such a zero-temperature transition defines a regime of *quantum criticality*. Although the quantum critical point itself occurs only at a single point in the phase diagram, its influence counterintuitively extends to finite temperature.

To see this, let Δ denote a characteristic energy scale which vanishes at the critical point. It may represent an energy gap, or the energy scale over which a gapless excitation has changed considerably, generally encoding the scale below which the system resolves deviations from the critical point. When $T \gtrsim \Delta$, the thermal fluctuations begin to mask these deviations, causing the system to remain quantum critical. This gives rise to the characteristic quantum critical fan, whose width grows with temperature, as is illustrated in Figure 4.1. Within this regime, the system is no longer strictly at a zero-temperature fixed point, but the temperature acts as the dominant infrared scale. Consequently, observables controlled by the critical sector often collapse onto universal scaling forms depending only on dimensionless ratios such as ω/T and $k/T^{1/z}$, up

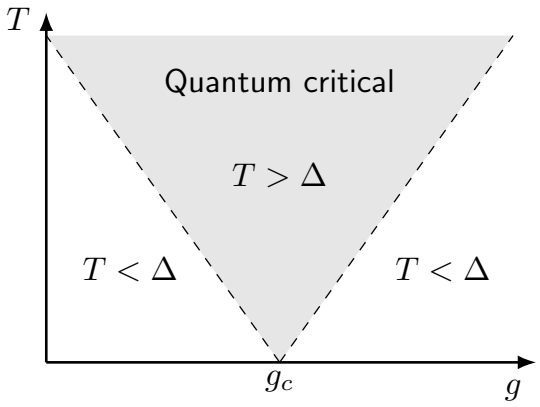

Figure 4.1: Schematic phase diagram of a quantum critical system.

to overall powers fixed by dimensional analysis [115]. The dynamical critical exponent z characterizes the anisotropic scaling of space and time, and depends on the universality class of the critical point.

Quantum critical regimes are especially interesting in metals, where coupling between itinerant electrons and critical collective modes can invalidate the Landau quasiparticle picture. Scattering rates are naturally Planckian by the scaling analysis, and instead of sharp poles in the Green's functions corresponding to long-lived excitations, they can exhibit broad continua or branch-cut like behavior characteristic of incoherent many-body dynamics. In this sense, the system behaves more like a strongly correlated "quantum soup" [54].

Considerable recent interest has focused on Sachdev-Ye-Kitaev (SYK) type models that describe solvable large-N fermionic systems with random all-to-all interactions [116, 117]. These models realize strongly interacting quantum critical dynamics, and recent lattice extensions [118, 119] capture several hallmark features of strange metals, such as a T-linear resistivity [50], a $T \ln T$ specific heat [120], and the mid-IR scaling of the optical conductivity [48].

One influential interpretation is that strange metallic behavior is associated with proximity to a quantum critical point. However, this picture has come under increasing scrutiny [46]. Experimental phenomenology instead suggests the possibility of an extended quantum critical regime, or even a quantum critical *phase* at zero temperature, rather than a single point [121]. Nevertheless, the universality associated with critical dynamics may help explain the robustness of T-linear transport across very different material families, as well as the approximate ω/T-scaling of the optical conductivity [48, 120, 122].

As we will see, quantum critical phases naturally emerge in holographic models and thus provide a complementary route to such physics. In fact, SYK models are intimately linked to the near-horizon AdS_2 geometries of certain holographic models [56] (see Section 4.3.2 below), and are believed to admit dual

gravitational descriptions [123]. The two approaches provide complementary strengths, with certain aspects more naturally addressed in either the SYK language (e.g., point defects) or the holographic one (e.g., the finite momentum response).

It is through this lens that holography becomes valuable for condensed matter physics. It provides controlled access to strongly interacting finite-density regimes where quasiparticles fail and universal scaling dominates. When extended to incorporate salient features of real materials, such as translational symmetry breaking (Chapter 5) or long-range Coulomb interactions (Chapter 6), it becomes a useful framework for probing universal aspects of strange-metal phenomenology.

4.3 Background geometries

The simplest and most widely used finite-density holographic background is the Reissner-Nordström (RN) AdS black hole. It describes a compressible strongly interacting state with a conserved U(1) charge density, and serves as the minimal starting point for most applications to condensed matter systems. It is obtained from the Einstein-Maxwell bulk action

$$S_{EM} = \frac{1}{2\kappa^2} \int \mathrm{d}^{d+2}x\sqrt{-g} \left(R - 2\Lambda - \frac{1}{4g_F^2} F_{\mu\nu}F^{\mu\nu} \right) , \tag{4.5}$$

where d denotes the number of spatial dimensions in the boundary theory, $\kappa^2 = 8\pi G$ is Einstein's gravitational constant, g_F the coupling constant of the bulk $U(1)$ gauge field A, $F = \mathrm{d}A$, and $\Lambda = -d(d+1)/2L^2$ is the negative cosmological constant needed to make spacetime asymptotically AdS. The theory admits charged black hole background solutions of the form

$$\mathrm{d}s^2 = \frac{L^2}{r^2} \left(-f(r)\,\mathrm{d}t^2 + \mathrm{d}x_i^2 + \frac{1}{f(r)}\,\mathrm{d}r^2 \right) , \quad A = \mu \left[1 - \left(\frac{r}{r_h} \right)^{d-1} \right] \mathrm{d}t\,. \tag{4.6}$$

The metric is here expressed in Poincaré coordinates, where r is an (inverted) radial coordinate that runs from the black hole horizon $r = r_h$ to the conformal boundary at $r = 0$. The $r \to 0$ limit value of the gauge field, μ, is canonically identified with chemical potential on the boundary[4], and the emblackening factor $f(r)$ takes the form

$$f(r) = 1 - M \left(\frac{r}{r_h} \right)^{d+1} + Q^2 \left(\frac{r}{r_h} \right)^{2d} , \tag{4.7}$$

[4] In Paper IV, we clarify that this identification is technically only valid up to an overall numerical constant.

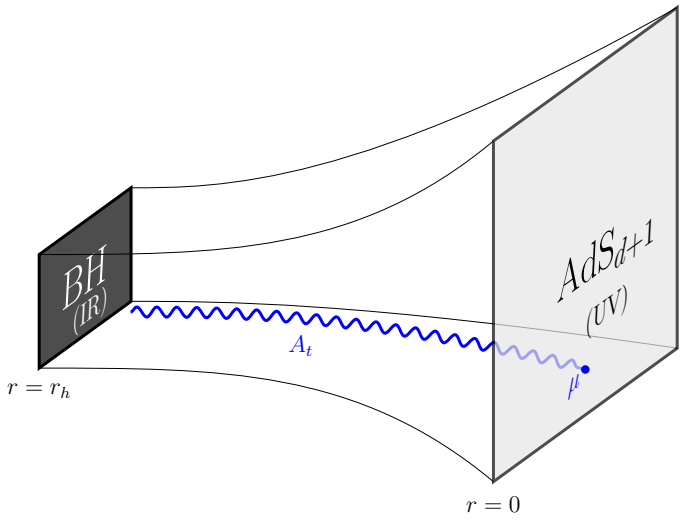

Figure 4.2: Schematic illustration of the RN background geometry (4.6). There is a black hole at $r = r_h$. The bulk gauge field A_t takes the value of the chemical potential μ at the conformal boundary.

where $f(r \to 0) \to 1$, such that the geometry at the asymptotic boundary is pure AdS as required by the duality. The black hole mass M and the chemical potential μ can be expressed in terms of dimensionless black hole charge Q as

$$M = 1 + Q^2\,, \quad \mu = \sqrt{\frac{2d}{d-1}}\frac{g_F L}{r_h} Q\,. \tag{4.8}$$

The geometry is schematically illustrated in Figure 4.2. The radial coordinate, which corresponds to the (inverse) energy scale of the dual theory, effectively describes the RG flow. The finite temperature terminates the RG flow at the horizon before the true zero-temperature infrared fixed point at $r \to \infty$ is reached.

4.3.1 Background thermodynamics

Upon varying the action (4.5) and integrating by parts, one obtains a bulk term containing the bulk equations of motion, along with a boundary term. The former vanishes on-shell, leaving

$$\delta S^*_{\mathrm{EM}} = \frac{1}{2\kappa^2}\oint_{\partial \mathrm{AdS}} \sqrt{-\gamma}\,\mathrm{d}^{d+1}x\,\left[n_\mu\left(\nabla_\nu \delta g^{\mu\nu} - \nabla^\mu \delta g\right) + \delta A_\mu g_F^{-2} n_\nu F^{\mu\nu}\right]\,, \tag{4.9}$$

where $\gamma_{\mu\nu} = g_{\mu\nu} - n_\mu n_\nu$ is the induced boundary metric and n_ν is an outward-pointing unit normal on the boundary; $n_\mu n_\nu g^{\mu\nu} = 1$. The gravitational part of this action must be supplemented by a set of boundary counterterms: the

Gibbons-Hawking-York term to obtain a well-defined variational Dirichlet problem, and a counterterm[5] to regulate the divergent volume of the AdS space [125],

$$S_{\mathrm{GHY}} + S_{\mathrm{ct}} = -\frac{1}{\kappa^2} \oint_{\partial \mathrm{AdS}} \sqrt{-\gamma}\, \mathrm{d}^{d+1}x \left(K + d - \frac{\mathcal{R}}{2(d-1)} \right) . \tag{4.10}$$

Here, $K = \gamma^{\mu\nu}\nabla_\mu n_\nu$ is the trace of the extrinsic curvature and $\mathcal{R}$ is the Ricci scalar of the $(d+1)$-dimensional boundary hypersurface.

The variation of the total on-shell action $\delta S^*_{\mathrm{EM}} + \delta S^*_{\mathrm{GHY}} + \delta S^*_{\mathrm{ct}}$ must, from the point of view of the dual field theory, take the form

$$\delta S = \int \mathrm{d}^{d+1}x \left(\frac{1}{2}\mathcal{T}^{\alpha\beta}\delta\eta_{\alpha\beta} + \mathcal{J}^\alpha \delta \mathcal{A}_\alpha \right) , \tag{4.11}$$

where the boundary stress tensor $\mathcal{T}^{\alpha\beta}$ and U(1) current $\mathcal{J}^\alpha$ are sourced by the (flat) boundary metric $\eta_{\alpha\beta} = (r^2/L^2)\gamma_{\alpha\beta}$ and external gauge field $\mathcal{A}_\alpha$, respectively. We distinguish boundary quantities by calligraphic letters for clarity, and adopt the index notation[6] $\mu = (\alpha, r)$, where α runs over the boundary spacetime directions. The application of the GKPW formula (4.4) yields the expectation values of these operators, which for the the RN black hole results in

$$\begin{aligned} \langle \mathcal{J}^t \rangle &= \rho = \sqrt{2d(d-1)}\frac{Q}{2\kappa^2 g_F L}\left(\frac{L}{r_h}\right)^d , \\ \langle \mathcal{T}^{tt} \rangle &= \epsilon = \frac{d}{2\kappa^2 r_h}\left(\frac{L}{r_h}\right)^d (1+Q^2) , \quad P = \epsilon/d , \end{aligned} \tag{4.12}$$

the charge, energy and pressure densities, respectively. Furthermore, the (Hawking) temperature and entropy density are given by

$$T = \frac{1}{4\pi r_h}\left(1 + d - (d-1)Q^2\right) , \quad s = \frac{2\pi}{\kappa^2}\left(\frac{L}{r_h}\right)^d , \tag{4.13}$$

which, according to the holographic dictionary, equal those of the boundary theory. Together, these quantities obey the fundamental thermodynamic relation $\epsilon + P = sT + \mu\rho$.

The thermodynamics of the model are thus controlled by a single dimensionless parameter Q, which is most often re-expressed in terms of the dimensionless ratio μ/T. At $\mu/T = 0$, the black hole is charge neutral (a Schwarzschild black hole), and the boundary theory is at zero density. As $\mu/T \to \infty$, the black hole

[5] In odd space dimensions d, the Maxwell part is also plagued by logarithmic divergences. These do not matter for the background solutions considered here, but must be added at the level of the fluctuations, cf. Appendix B in Paper IV. In $d > 3$ there are also additional gravitational counterterms [124].

[6] In coordinate systems on Fefferman-Graham form, both the terms multiplying δA_r and $\delta g_{r\mu}$ in (4.9) vanish. That (4.11) only runs over boundary indices is therefore not an issue.

becomes extremal, with its mass entirely determined by the charge, describing a boundary theory at zero temperature. The ratio μ/T therefore controls the crossover between thermally dominated and density-dominated regimes.

Finally, there is a choice to be made between two and three spatial dimensions d in the boundary theory, which on the bulk side means either AdS_4 or AdS_5 geometries. Most often, the simpler AdS_4 suffices, or is more relevant for applications to strange metals (for instance, most of the conduction in cuprate high-temperature superconductors happens along the copper oxide planes [43]). Papers III and V consider AdS_4 geometries. In Paper IV, we study phenomena that require the full, dynamic Maxwell equations in three dimensions, and therefore use AdS_5.

4.3.2 Quantum critical geometries

Many holographic geometries naturally realize quantum criticality. The AdS-Schwarzschild solution, which corresponds to (4.6) with $\mu = 0$, describes a CFT_{d+1} at finite temperature. Since space and time scale identically, this corresponds to a relativistic quantum critical point with dynamical critical exponent $z = 1$. At finite density, the infrared structure is richer. Expanding the emblackening factor of the RN metric (4.6) near the horizon, the metric takes the form[7] [126]

$$\mathrm{d}s^2 \approx \frac{\tilde{L}^2}{\zeta^2}\left[-\left(1-\frac{\zeta^2}{\zeta_h^2}\right)\mathrm{d}\tau^2 + \frac{\mathrm{d}\xi^2}{\left(1-\frac{\zeta^2}{\zeta_h^2}\right)}\right] + \ell^2\,\mathrm{d}x_i^2\,, \tag{4.14}$$

which describes an AdS_2 black hole times $\mathbb{R}^d$, and in the extremal $T = 0$ ($\zeta_h \to \infty$) limit, $AdS_2 \times \mathbb{R}^d$. The corresponding infrared theory is therefore scale invariant in time, since the AdS_2 factor is dual to a CFT_1, while the spatial coordinates act only as spectators. This is a manifestation of *local* quantum criticality, where the dynamical exponent $z = \infty$. Crucially, the AdS_2 geometry controls the low-energy sector of an entire compressible phase, rather than a single critical point. Holographic matter therefore provides a natural realization of an extended quantum critical regime governed by the AdS_2 fixed point [54].

The RN model is, however, somewhat pathological. In the extremal $T \to 0$ limit, it exhibits a non-vanishing ground state entropy density[8], suggesting an unphysically large ground state degeneracy. This can be remedied by studying more complicated Einstein-Maxwell-Dilaton (EMD) models that feature an

[7] By expanding $f(r) \approx -4\pi T(r-r_h) + f''(r_h)(r-r_h)^2/2$, the specific coordinate change becomes $r = r_h + \zeta^{-1} + 4\pi T/f''(r_h)$, $t = \tau\sqrt{2/f''(r_h)}$. In (4.14), $\tilde{L} = L/r_h$, $\ell = \tilde{L}\sqrt{f''(r_h)/2}$, and $\zeta_h = f''(r_h)/(4\pi T)$.

[8] This is perhaps not obvious from (4.13), because $Q \propto \mu r_h$, which results in $s = \frac{2\pi}{\kappa^2}\left(\sqrt{\frac{2(d-1)}{3(d+1)}}\frac{\kappa\mu}{g_F}\right)^d + O(T/\mu)$.

additional scalar field. The resulting background geometries are then characterized by both a dynamical critical and hyperscaling-violating[9] exponent z and θ, with a ground state entropy density $s \sim T^{(d-\theta)/z}$. This allows theories for which $z \to \infty$, $\theta \to -\infty$ but with $-z/\theta = 1$ to achieve Sommerfeld-like metallic entropy scaling $s \sim T$ [127]. The Gubser-Rocha model [128] is one notable example, which in the presence of translational symmetry breaking also can give rise to the T-linear resistivity as observed in strange metals [57]. We study this model alongside the RN model in Paper IV.

4.4 Linear response and boundary Green's functions

Beyond determining the thermodynamics of the dual theory, the main power of holography lies in the computation of dynamical response functions through (4.4). This is achieved by perturbing the system around a given background solution, $g_{\mu\nu} \mapsto g_{\mu\nu} + \delta g_{\mu\nu}$, $A_\mu \mapsto A_\mu + \delta A_\mu$, and working within linear response. With the action (4.5), one obtains the linearized Einstein and Maxwell equations

$$\delta G_{\mu\nu} + \Lambda \delta g_{\mu\nu} = \kappa^2 \delta T_{\mu\nu} \,, \quad \nabla_\mu \delta F^{\mu\nu} = 0 \,, \tag{4.15}$$

where the stress-energy tensor $T_{\mu\nu} = (F_{\mu\rho}F^{\rho}{}_{\nu} - g_{\mu\nu}F_{\rho\sigma}F^{\rho\sigma}/4)/(2\kappa^2 g_F^2)$ and the Einstein tensor $G_{\mu\nu} = R_{\mu\nu} - g_{\mu\nu}R/2$. By solving these equations and evaluating the linearized version of the on-shell boundary action as in (4.11), one obtains the n-point functions of the dual theory by successive variational derivatives with respect to the sources. In practice, this amounts to fixing a value for the linearized source of the desired operator at the UV boundary, setting the other sources to zero, which makes the on-shell action proportional to the operator.

The IR boundary conditions at the black hole horizon are more subtle, especially since the equations of motion are generally singular at that point. In Euclidean space, one simply requires regularity at the horizon, whereby (4.4) can be applied to obtain Euclidean (imaginary time) n-point functions. However, one of the major advantages of holography, particularly for condensed matter applications, is the ability to compute real-time Green's functions directly, without the need for analytic continuation [54]. A complete treatment, distinguishing between various real-time correlators, involves an extension of the black hole geometry, which results in two separate asymptotic boundaries. This leads to a doubling of the boundary degrees of freedom, naturally reproducing the Schwinger-Keldysh contour of the dual field theory [129], whereby (4.4) can be applied consistently.

[9] This relates to how the number of thermodynamically relevant degrees of freedom scale. For instance, the Fermi surface has dimension $\theta = d - 1$, which is why Fermi liquids exhibit $s \sim T$ in all dimensions [127]. For the RN model, $z = \infty$ but $\theta = 0$, so $s \sim T^0$.

A more pragmatic approach, however, is to impose infalling boundary conditions at the horizon, such that all modes carry energy into the black hole. This effectively selects the retarded sector of the Schwinger-Keldysh contour and yields the retarded Green's function on the boundary[10]. The caveat is that instead of directly applying (4.4) to the on-shell action, the Green's function is to be extracted from the boundary term at conformal infinity [130, 131]. For a boundary term in momentum space of the form

$$S^* = \oint_{r\to 0} \frac{\mathrm{d}\omega\, \mathrm{d}^d k}{(2\pi)^{d+1}}\, h(-\omega, -\boldsymbol{k})\mathcal{F}(\omega, \boldsymbol{k})h(\omega, \boldsymbol{k})\,, \tag{4.16}$$

the retarded Green's function of the operator $\mathcal{O}$ dual to h is identified with

$$G^R_{\mathcal{O}\mathcal{O}}(\omega, \boldsymbol{k}) = -2 \lim_{r\to 0} \mathcal{F}(\omega, \boldsymbol{k})\,. \tag{4.17}$$

To implement such infalling boundary conditions at the horizon, there are two main options. One is to factor out an infalling plane-wave factor from all fields in a Frobenius-like expansion[11],

$$\Phi(\boldsymbol{x}, r) \to (r_h - r)^{-i\omega/4\pi T}\Phi^*(\boldsymbol{x}, r)\,, \tag{4.18}$$

whereby one solves the equations of motion for the regular fields Φ^*. The IR boundary conditions for Φ^* are obtained from regularity, by algebraically solving the equations of motion order by order in a series expansion around $r = r_h$. Alternatively, one can transform to infalling Eddington-Finkelstein coordinates, which for a metric as simple as the RN one looks like

$$\mathrm{d}t \to \mathrm{d}v = \mathrm{d}t - \frac{1}{f(r)}\,\mathrm{d}r\,. \tag{4.19}$$

In this case, the equations of motion remain regular at $r = r_h$, and there is no need to impose additional infalling boundary conditions explicitly[12], as the regular, infalling solution is automatically selected. We employ this method in Paper IV, which treats homogeneous backgrounds, but for the lattice models studied in Paper III, the coordinate shift becomes so complicated that it is not worth the effort.

[10] Advanced Green's functions are analogously obtained by imposing outgoing boundary conditions at the horizon.

[11] It is useful to factor out additional integer powers of $(r_h - r)$ for any field with a radial index.

[12] EF coordinates slightly change the UV boundary conditions, however. Regularity requires that the radial components of any field must equal the EF-time v-component at the boundary, e.g., $\delta A_r = \delta A_v$. This becomes particularly important when extracting the density-density response $\langle \mathcal{J}^t \mathcal{J}^t \rangle$ as one then fixes $\delta A_v = \delta A_r = 1$.

As an example, we can consider the Maxwell part of the Reissner-Nordström action in AdS_4. By solving the equations of motion, one infers that the near-boundary expansion of the gauge-field reads

$$A_\mu = a_\mu^{(0)} + a_\mu^{(1)} r + \mathcal{O}(r^2)\,, \tag{4.20}$$

where $a_\mu^{(0)}$ and $a_\mu^{(1)}$ are the integration constants of the two linearly independent solutions to the bulk equations of motion. The gauge field A_μ in the bulk is dual to the current operator $\mathcal{J}^\mu$ on the boundary, whose source is an external boundary gauge field $\mathcal{A}_\mu$. Fixing a value for this source amounts to a Dirichlet boundary condition for A_μ, which determines the value of $a_\mu^{(0)}$, in accordance with the "$\phi \to h$" prescription in (4.2). Evaluating the Maxwell part of (4.9), one obtains

$$\delta S^*_{EM} = \frac{1}{2\kappa^2 g_F^2} \oint \mathrm{d}^{d+1}x\, a_\mu^{(0)} \eta^{\mu\nu} a_\nu^{(1)}\,. \tag{4.21}$$

The integration constant $a_\mu^{(1)}$ becomes related to $a_\mu^{(0)}$ by the infalling boundary conditions at the horizon, whereby (4.21) takes the form of (4.16) and one may extract $G^R_{\mathcal{J}^\mu \mathcal{J}^\nu}$. The horizon thus sets the relation between source and response, and is ultimately responsible for dissipative (imaginary) parts of the boundary Green's functions.

Closely related to the retarded Green's functions are the *quasinormal modes* of the system. These correspond to the poles of the Green's functions, or equivalently, to non-trivial solutions in the absence of external sources. They are obtained by solving the linearized equations with homogeneous boundary conditions at the UV boundary, resulting in a discrete spectrum of generally complex frequencies (or, equivalently, complex wavevectors). We perform a computation of quasinormal modes in Paper IV.

With the holographic response machinery in place, we now turn to concrete applications involving momentum relaxation and dynamical electromagnetism.

5

Holographic transport

"Expect some turbulence!"

Gyrocopter

Transport measurements are central to experimental condensed matter physics. Here, we consider in particular thermoelectric transport, capturing the interplay between heat and charge transport, and magnetotransport, i.e., how these quantities change under the influence of an external magnetic field. Subjecting the system to either an external electric field E^i or a thermal drive $\zeta^i = -\nabla^i T/T$ will in general cause both an electric current J^i and a thermal current Q^i to flow. The relationship between the sources and the currents is given in terms of the thermoelectric conductivity matrix,

$$\begin{pmatrix} J^i \\ Q^i \end{pmatrix} = \begin{pmatrix} \sigma^{ij} & T\alpha^{ij} \\ T\bar{\alpha}^{ij} & T\bar{\kappa}^{ij} \end{pmatrix} \begin{pmatrix} E_j \\ \zeta_j \end{pmatrix} , \tag{5.1}$$

which defines the electrical, thermoelectric, and thermal conductivities σ, α and $\bar{\kappa}$, respectively. These conductivities are in general tensorial quantities, which gain non-zero off-diagonal components in the presence of an external magnetic field B. Since a magnetic field breaks time-reversal symmetry, the Onsager reciprocity relations generalize to $\alpha_{ij}(B) = \bar{\alpha}_{ji}(-B)$.

5.1 Breaking translational invariance

To obtain finite DC conductivities, translational invariance must be broken in order for momentum to relax; otherwise, an external electric field can continuously accelerate the charge and heat carriers, resulting in infinite conductivities. At the most basic level, the breaking of translational invariance simply requires

a right-hand side of the Ward identity

$$\partial_\mu \mathcal{T}^{\mu i} = 0 \tag{5.2}$$

which encodes momentum conservation. This can be achieved by adding an operator with explicit position dependence [101] to the theory, or by making gravity massive in the bulk [132, 133]. In fact, many of the common mechanisms for breaking translational invariance in holography lead to an effective graviton mass m_g in the IR [134]. This partially breaks the diffeomorphisms, and since gauge invariance in the bulk gives rise to the Ward identities on the boundary [12], these are modified accordingly, producing a relaxation rate $\Gamma \sim m_g^2$ on the right-hand side of (5.2).

The simplest choice of such operators to add are scalars, where axions $\phi = \alpha x^n$ [135, 136] or Q-lattices $\phi = e^{ikx}\psi(r)$ [137] are particularly convenient, as they keep the background geometry homogeneous. In this thesis, we consider a spatially modulated chemical potential,

$$\mu(x, y) = \bar{\mu} + \frac{\delta\mu}{2}\left[\cos(Gx) + \cos(Gy)\right] , \tag{5.3}$$

which has several distinct advantages. Interpreted as a lattice, this introduces an explicit Brillouin zone, as well as Umklapp physics, where physical processes at momentum $\boldsymbol{k}$ are influenced by processes at $\boldsymbol{k} \pm \boldsymbol{G}_i, \boldsymbol{k} \pm 2\boldsymbol{G}_i$, and so on, where $\boldsymbol{G}_i$ is a reciprocal lattice vector. This substantially affects the mode structure, as will be discussed in Section 5.3 below. Additionally, (5.3) introduces two scales: $\delta\mu/\bar{\mu}$, which encodes the strength of the translational symmetry breaking, and the inverse length scale G. The latter facilitates a much clearer comparison to real lattice systems[1], in particular since the chemical potential μ need not be interpreted as the chemical potential of the electrons in the dual condensed matter system[2].

5.2 Lattice equations

The downside of an explicit spatial structure as in (5.3) is the numerical complexity introduced into the equations, as the additional spatial dimensions turn already challenging ODEs into PDEs. Furthermore, the background geometries no longer admit analytical solutions, meaning that they also need to be solved for numerically, before one can linearize around them to extract AC responses.

[1] For example, while the parameter α in linear axion models controls the strength of the translational symmetry breaking, analogous to $\delta\mu$, it is not as straightforwardly related to a microscopic lattice quantity.

[2] Cf. the discussion around footnote 4 on page 32.

5.2.1 Inhomogeneous background geometries

The first step in the analysis of systems subject to a spatially varying chemical potential (5.3) is to solve for the inhomogeneous background geometries. This takes the form of a boundary value problem (BVP), where one should impose generalized versions of the boundary conditions for the charged black hole geometries in Section 4.3: in the UV, the time component of the gauge field should asymptote to the spatially varying chemical potential (5.3), and as always, the metric must asymptote to pure AdS. The IR boundary conditions are simply that the solutions remain regular, and the equations of motion that follow from the Einstein-Maxwell action (4.5) are

$$R_{\mu\nu} = \kappa^2 \left(T_{\mu\nu} - \frac{1}{2} T g_{\mu\nu} \right) , \qquad \nabla_\mu F^{\mu\nu} = 0 \, , \tag{5.4}$$

where we have written the Einstein equations in trace-reversed form.

As they stand, these non-linear PDEs are ill-suited for a numerical solution of the BVP. By expressing them in terms of a differential operator $\mathcal{L}[\Phi] = 0$ acting on the constituent fields $\Phi = \{g_{\mu\nu}, A_\mu\}$, it becomes apparent that the operator has zero modes originating from the pure gauge modes of the underlying diffeomorphism and U(1) invariance. The principal symbol is therefore not sign-definite, causing relaxation-type schemes for the non-linear equations to diverge.

The key to obtaining a well-posed BVP is the so-called de Turck trick [138]: the replacement of the Ricci tensor with the harmonic Ricci tensor,

$$R_{\mu\nu} \to R^H_{\mu\nu} = R_{\mu\nu} - \nabla_{(\mu} \xi_{\nu)} \, , \tag{5.5}$$

will dynamically impose the gauge $\xi^\mu = 0$, where $\xi^\mu = g^{\lambda\nu}(\Gamma^\mu_{\lambda\nu} - \bar{\Gamma}^\mu_{\lambda\nu})$ is the de Turck vector and $\bar{\Gamma}^\mu_{\nu\rho}$ is the Christoffel symbol for an appropriately chosen reference metric $\bar{g}_{\mu\nu}$ that is a solution to the Einstein equations [139, 140]. Similarly, by adding a term $\nabla^\nu \varphi$ to the left hand side of Maxwell's equations, the generalized Lorenz gauge $\varphi = \nabla_\mu (A^\mu - \bar{A}^\mu) + \xi^\mu (A_\mu - \bar{A}_\mu) = 0$ is imposed. The subtraction of $\bar{A} = \frac{1}{2} B (x \, \mathrm{d}y - y \, \mathrm{d}x)$ is needed in the presence of a background magnetic field B in order to consistently identify the x and y-directions as periodic, which is required for numerical implementations.

These shifts effectively endow the gauge degrees of freedom with kinetic terms. In turn, the differential operator becomes elliptic, with all principal eigenvalues negative. A Newton-Raphson-type scheme can then be applied to the modified non-linear PDEs $\mathcal{L}[\Phi] = 0$: given a sufficiently good initial guess $\Phi^{(0)}$, the solution can be found by iterating

$$\Phi^{(i+1)} = \Phi^{(i)} - \mathcal{J}^{-1}[\Phi^{(i)}] \mathcal{L}[\Phi^{(i)}] \, , \qquad i \geq 0 \, , \tag{5.6}$$

where the Jacobian $\mathcal{J} = \delta \mathcal{L} / \delta \Phi$ is the linearization of the non-linear operator $\mathcal{L}$ around the current iterate $\Phi^{(i)}$. The level of convergence can be assessed by

verifying that the square of the de Turck vector[3] ξ^2 and the Maxwell scalar φ are numerically close to zero at each point in the computational domain. For a further discussion on the numerical implementation, see Appendix A in Paper III.

5.2.2 DC transport: Stokes flow

With the background geometries in hand, we can move on to transport, which is in general much more difficult. Fortunately, as was shown in a series of works [141–144], the thermoelectric DC conductivities in Einstein-Maxwell-Dilaton theories can be obtained by solving a much simpler Stokes flow problem on the black hole horizon of a given background geometry. The underlying principle is that one can construct charge and heat currents J^i and Q^i whose spatial averages are radially conserved and coincide, in the UV limit $r \to 0$, with the boundary charge and heat current operators. They may therefore be solved for on the horizon $r = r_h$, where a consistent closed set of equations are given by the conservation equations and constitutive relations[4]

$$\begin{aligned} \nabla_i J^i &= 0\,, \qquad & J^i &= n^H v^i + \sqrt{h}(E^i + \nabla^i w + F_H^{ij} v_j)\,, \\ \nabla_i Q^i &= 0\,, \qquad & Q^i &= s^H T v^i\,, \end{aligned} \tag{5.7}$$

where the index i runs over the spatial coordinates transverse to the black hole, along with

$$2\sqrt{h}\nabla^j \nabla_{(i} v_{j)} + (\,\mathrm{d}\chi^H)_{ij} Q^j + F^H_{ij} J^j + s^H T \zeta_i - \sqrt{h}\nabla_i p + n^H(E_i + \nabla_i w) = 0\,, \tag{5.8}$$

which takes the form of a Stokes equation for an incompressible fluid at low Reynolds numbers. These equations are to be solved for the fluid velocity v^i, energy density w and pressure p in terms of the horizon metric h_{ij}, charge density n^H, entropy density s^H, magnetic field F^H_{ij} and "gravitational magnetic field"[5] $(\,\mathrm{d}\chi)^H_{ij}$, for a given external electric field E^i or thermal drive ζ^i. To obtain the DC conductivities, one therefore only needs to solve a non-linear $(d+1)$-dimensional PDE for the background, followed by a d-dimensional, relatively simple linear PDE[6] for a reduced set of fields on the horizon. Additionally, this avoids the numerically delicate $\omega \to 0$ limit of AC data.

[3] It is spacelike ($\xi^2 \geq 0$), so it suffices to check the square rather than all components.

[4] We set the dilaton $\phi = 0$ here.

[5] This term arises from the time-space components g_{ti} of the metric, which correspond to the energy current $T^{ti} = Q^i + \mu J^i$. Analogously to the Lorentz force term for the charge current, this produces a coupling $(\,\mathrm{d}\chi^H)_{ij} Q^j$, hence the name.

[6] There are zero modes present in the Stokes equations due to the fact that the pressure and energy densities only appears as derivatives. One can simply fix a value at a single point in the computational domain to remove the associated zero eigenvalues from the matrix describing the discretized PDE [145].

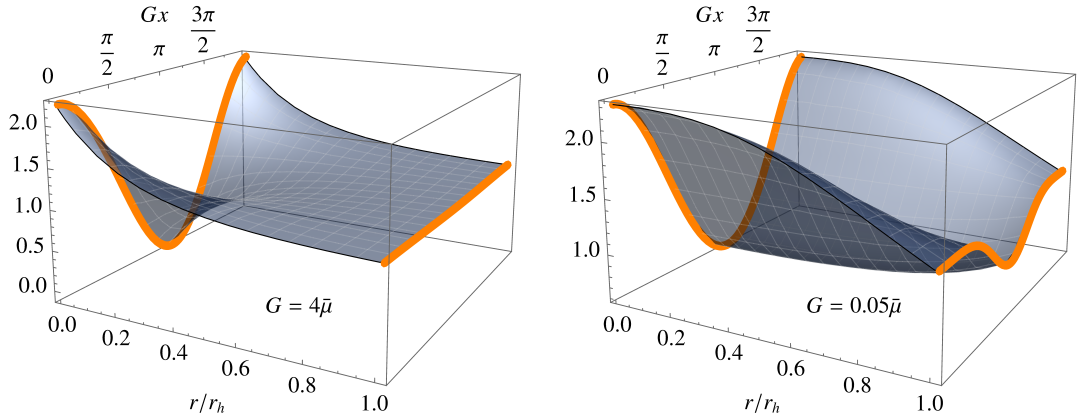

Figure 5.1: RG flow of a lattice deformation captured in the radial evolution of the background electric field F_{tr} (proportional to the boundary charge density) for an AdS_4 RN model subject to a 1D lattice deformation with $\delta\mu = 0.5\bar{\mu}$ at $T = 0.15\bar{\mu}$. For $G = 4\bar{\mu}$ (left), the lattice washes out in the IR, whereas for $G = 0.05\bar{\mu}$ (right), the RG flow is halted by the horizon.

The fact that the DC transport coefficients are controlled by the black hole horizon for these models can be seen as a manifestation of the fact that the IR physics is governed by near-horizon geometry. Likewise, the fact that the equations are fluid equations matches the idea that hydrodynamics emerges as the effective theory at sufficiently late times ($\omega \to 0$) and long distances ($\boldsymbol{k} \to 0$) [146]. With this in mind, it is fruitful to analyze the background geometry, which encodes the RG flow. While a scaling analysis of the lattice deformation (5.3) reveals that it is irrelevant [147], the finite temperature of the black hole (encoded in the horizon at $r = r_h$) can cut off the RG flow before reaching the true IR fixed point (at $r = \infty$). This is exemplified in Figure 5.1 for the background electric field F_{tr} of a geometry subject to a 1D lattice deformation in the UV. When $G \ll \bar{\mu}$, the lattice leaves a substantial imprint on the horizon, which in turn affects the DC conductivities via the horizon metric[7] $h_{ij}(x^i)$ and transport coefficients $n^H(x^i), s^H(x^i), \ldots$ in the Stokes equations (5.7). We discuss the implications this has for the effective hydrodynamic description in Section 5.3 below.

5.2.3 AC transport

Finite frequency transport requires linearizing around the inhomogeneous background geometries. As in Section 4.4, we let $\Phi \mapsto \Phi + \delta\Phi$, where now

$$\delta\Phi(t, \boldsymbol{x}, r) = \delta\Phi(\boldsymbol{x}, r) e^{-i\omega t + i\boldsymbol{k}\cdot\boldsymbol{x}} \,. \tag{5.9}$$

[7] The various components of the background metric display a similar behavior, and can give rise to a corrugated black hole geometry, cf. Figure 2 in Paper III.

In analogy with Bloch's theorem [6], the amplitudes $\delta\Phi(\boldsymbol{x}, r)$ are periodic with respect to the potential, whereas the exponentials are not.

Just as for the backgrounds, a well-posed BVP suitable for numerics can be obtained by a de Turck-like trick[8]. The de Donder and Lorenz gauge choices,

$$\tau_\mu = \nabla^\nu \left(\delta g_{\mu\nu} - \frac{1}{2} g_{\mu\nu} \delta g_\rho{}^\rho \right) = 0 \,, \quad \vartheta = \nabla^\mu \delta A_\mu = 0 \,, \tag{5.10}$$

can be implemented by shifting the linearized equations (4.15) as

$$\begin{aligned} \delta G_{\mu\nu} &\to \delta G_{\mu\nu} - \nabla_{(\mu} \tau_{\nu)} \,, \\ \delta(\nabla_\mu F^{\mu\nu}) &\to \delta(\nabla_\mu F^{\mu\nu}) + \nabla^\nu \vartheta \,. \end{aligned} \tag{5.11}$$

One may again monitor the convergence by verifying that τ^2 and φ are numerically close to zero over the computational domain.

After solving the linearized equations, the electrical conductivity may be extracted from the Kubo formula

$$\sigma^{ij}(\omega) = \frac{i}{\omega} \left[G^R_{\mathcal{J}^i \mathcal{J}^j}(\omega, k = 0) - \mathrm{Re}\, G^R_{\mathcal{J}^i \mathcal{J}^j}(\omega = 0, k \to 0) \right] \,, \tag{5.12}$$

where the retarded Green's function is obtained as in (4.17), and the subtraction removes potential contact terms [146, 148]. The thermal and thermoelectric AC conductivities $\bar{\kappa}^{ij}(\omega)$ and $\alpha^{ij}(\omega)$ follow similarly from the Green's functions $G^R_{\mathcal{Q}^i \mathcal{Q}^j}$ and $G^R_{\mathcal{J}^i \mathcal{Q}^j}$, respectively, where the boundary heat current is obtained by removing the contribution to the total energy current associated with charge transport as

$$\mathcal{Q}^i = \mathcal{T}^{ti} - \mu(x, y) \mathcal{J}^i \,. \tag{5.13}$$

The appropriate UV boundary conditions for the fluctuations in the case of thermal transport are

$$\delta g_{ti} = \text{const.} \qquad \text{and} \qquad \delta A_i + \mu(x, y) \delta g_{ti} = 0 \,, \tag{5.14}$$

for a chosen direction i, setting the remaining fluctuations to zero. This fixes a source for the energy current $\mathcal{T}^{ti}$ while ensuring that the gauge-invariant source for the electrical current (i.e., the electric field) is zero.

5.3 Umklapp hydrodynamics

As we saw in Section 5.2.2, the DC transport coefficients are obtained from solving fluid-like equations on the black hole horizon. Similarly, AC transport of a strongly correlated system in local thermal equilibrium should also admit a

[8] An alternative is to use gauge-invariant variables. Although the construction of such variables is not particularly difficult, re-writing the equations of motion in terms of them is.

hydrodynamic description, valid up to some cutoff scale $\omega, k < \Lambda_{\text{hydro}}$. However, as was illustrated in Figure 5.1, the irrelevant lattice deformation (5.3) leaves an imprint on the horizon. Thus, the effective low-energy description is not standard, isotropic hydrodynamics, but rather hydrodynamics in the presence of a periodic potential: *Umklapp hydrodynamics*. We present here a brief outline of some key results in Ref. [149], as will be relevant for a complete understanding of the results in Paper III.

5.3.1 Homogeneous relativistic hydrodynamics

As we saw in Section 3.2.1, hydrodynamics is the theory of conserved quantities, which in the present case are the energy, particle, and momentum densities, just as in the kinetic-theory discussion of Part I. The starting point is therefore the conservation equations, now written in relativistic form,

$$\partial_\alpha \mathcal{T}^{\alpha\beta} = \mathcal{F}^{\beta\gamma}_{\text{ext}} \mathcal{J}_\gamma \,, \quad \partial_\alpha \mathcal{J}^\alpha = 0 \,, \tag{5.15}$$

where the stress tensor conservation equation acquires a source term due to the electrical field generated by the spatially varying chemical potential. The hydrodynamic analysis is based on the conserved quantities

$$\phi_i = \left[\epsilon, n, \pi_x, \pi_y\right]^T \,, \tag{5.16}$$

whereby a linearization of the conservation equations (5.15) around an equilibrium configuration $\bar{\phi}$ results in a linear system of equations for the fluctuations $\delta\phi$. In Fourier[9] space, this takes the form $K(\omega, k)\delta\phi = 0$, where

$$\begin{aligned} K &= \text{diag}(K_L, K_T) \,, \qquad & K_T &= \frac{\eta}{\chi^{(0)}_{\pi\pi}} k^2 - i\omega \,, \\ K_L &= \begin{pmatrix} -i\omega & 0 & ik \\ \frac{-\chi_{\epsilon n}}{d_\chi}\sigma_Q k^2 & -i\omega + \frac{\chi_{\epsilon\epsilon}}{d_\chi}\sigma_Q k^2 & ik\frac{\bar{n}}{\chi_{\pi\pi}} \\ ik\frac{\chi_{nn}\chi_{\pi\pi} - \bar{n}\chi_{\epsilon n}}{d_\chi} & ik\frac{\bar{n}\chi_{\epsilon\epsilon} - \chi_{\epsilon n}\chi_{\pi\pi}}{d_\chi} & \frac{\zeta+\eta}{\chi_{\pi\pi}}k^2 - i\omega \end{pmatrix} . \end{aligned} \tag{5.17}$$

Here we have used the standard first-order constitutive relations of relativistic hydrodynamics to express the currents in terms of transport coefficients σ_Q, ζ and η, and the conserved densities and their gradients. The $\chi_{\phi\phi}$ are static (thermodynamic) susceptibilities, defined as derivatives of the conserved densities with respect to their conjugate sources, and $d_\chi = \chi_{\epsilon\epsilon}\chi_{nn} - (\chi_{\epsilon n})^2$. The poles in the energy, density, and momentum Green's functions correspond to the roots of the polynomial equation $\det K = 0$, which in the longitudinal sector gives the three modes

$$\omega_D = -iD_\rho k^2 + \mathcal{O}(k^3) \,, \quad \omega_\pm = \pm v_s k - \frac{i}{2} D_s k^2 + \mathcal{O}(k^3) \,. \tag{5.18}$$

[9] Technically one must Laplace transform in time unless sources are added [146].

This describes a charge diffusion mode and a pair of propagating sound modes, where the speed of sound v_s and the charge and sound diffusion constants D_ρ and D_s depend on the hydrodynamic transport coefficients and the susceptibilities.

5.3.2 Lowest order inhomogeneous analysis

Next, we consider a spatially varying chemical potential in 1D, with $\delta\mu$ small, and expand the fluctuations in Bloch waves as

$$\delta\phi(t,x) = \sum_n \int_{-G/2}^{G/2} \mathrm{d}k\, e^{i(k+nG)} \delta\phi_n(t,k)\,. \tag{5.19}$$

For a qualitative understanding of the mode spectrum, it suffices to truncate the analysis at order $(\delta\mu)^2$ and to consider only nearest neighbors, i.e., the fluctuations $\delta\phi_{-1}, \delta\phi_0$ and $\delta\phi_1$ [149]. This results in a 12×12 dynamical matrix $K(\omega,k)$, with off-diagonal blocks that describe the coupling between adjacent Brillouin zones. As is relevant for Paper III, we restrict this analysis[10] to $k=0$, where the matrix decouples not only in longitudinal and transverse sectors (with respect to the fluid velocity), but also under parity in the x-direction ($G\to -G$).

The parity-odd, longitudinal sector, which influences the longitudinal current-current correlators (i.e., the conductivities), contains the modes

$$\begin{aligned}
\omega_{\text{Drude}}^{(L-)} &= -i(\Gamma_d + \Gamma_\eta)\,,\\
\omega_D^{(L-)} &= -i\left(D_\rho^{(0)} + \frac{\delta\mu^2}{\bar\mu^2} D_\rho^{(2)}\right) G^2 + i\Gamma_d\,,\\
\omega_\pm^{(L-)} &= \pm\left(c_s^{(0)} + \frac{\delta\mu^2}{\bar\mu^2} c_s^{(2)}\right) G - \frac{i}{2}\left(D_s^{(0)} + \frac{\delta\mu^2}{\bar\mu^2} D_s^{(2)}\right) G^2\,,
\end{aligned} \tag{5.20}$$

that is: (1) a Drude mode with two contributions to the total damping, $\Gamma_d \sim \delta\mu^2$ and $\Gamma_\eta \sim \delta\mu^2 G^2$, (2) an Umklapped charge diffusion mode with a lattice correction to the charge diffusion constant ($D_\rho^{(2)}$) and (3) a pair of Umklapped sound modes at $\omega_\pm \approx \pm c_s G$, where the speed of sound c_s has been renormalized by the lattice[11].

These modes play an important role in Paper III, where we study thermoelectric transport in a lattice system with $\bar\mu = 0$[12]. In this particle-hole

[10] These results cannot be obtained from a $k\to 0$ limit analysis due to an order-of-limits conflict with $\delta\mu$, originating in the perturbative treatment of the lattice. See [149] for an in-depth discussion.

[11] The quantities $D_\rho^{(0)}, D_s^{(0)}$ and $v_s^{(0)}$ equal those in the homogeneous setting in (5.18)

[12] As we saw in Figure 5.1, the lattice deformation has a large effect on the IR geometry mainly for $G \ll \bar\mu \neq 0$. One must however be careful in extrapolating this wisdom to the $\bar\mu = 0$ case. In fact, the horizon fluctuations are generally relatively large, with practically no renormalization at all for $T/G \gg 1$; cf. Figure 2 in Paper III.

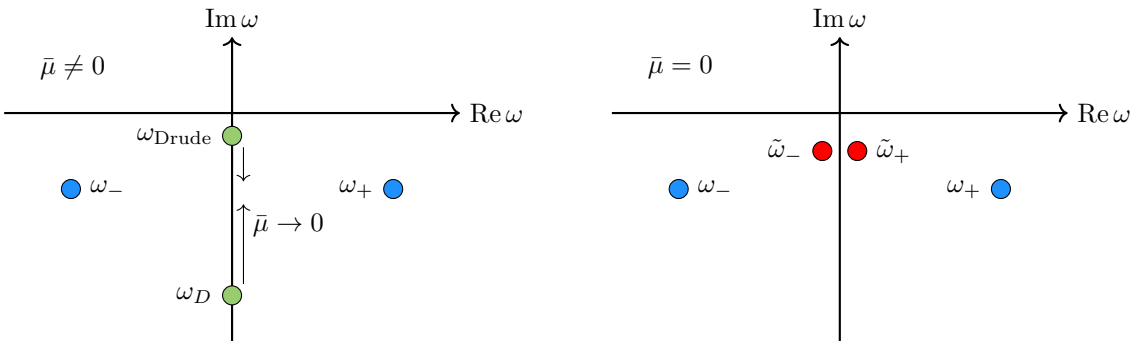

Figure 5.2: The modes of Umklapp hydrodynamics in the longitudinal, parity-odd sector at zero momentum. As the finite average chemical potential $\bar{\mu} \to 0$, the Drude and charge diffusion modes ω_{Drude} and ω_D collide, resulting in a pair of propagating modes $\tilde{\omega}_\pm$ that control thermal transport. The electrical transport is governed by the Umklapp sound modes $\omega_\pm$.

symmetric setting, charge and energy fluctuations decouple at linear order in the longitudinal channel relevant for transport. This means that the electric current overlaps only with the two Umklapp sound modes, whereas the heat current overlaps only with the two diffusive modes. Furthermore, the thermal sector warrants another separate analysis due to an order-of-limits conflict with $\bar{\mu} \to 0$. In fact, at small $\bar{\mu} \neq 0$ the Drude and Umklapp charge diffusion modes collide, turning into an additional pair of propagating modes, as is illustrated in Figure 5.2. This process, which at finite $\bar{\mu} \neq 0$ also influences the electrical transport, has been proposed as a possible explanation for the mid-infrared resonance of the optical conductivity [57] as observed experimentally in strange metals [48, 120, 122].

5.4 Emergent effective medium theory

An important observation we make in Paper III is that strong two-dimensional periodic potentials can generate spatial regions in which transport is locally well described by finite-density hydrodynamics, despite the vanishing average chemical potential. The local conductivity in these regions reacquires a Drude contribution due to the local non-zero density. When averaged over the lattice, these contributions add up, resulting in a broad, emergent Drude-like peak in the global electrical conductivity. This may be interpreted as an effective enhancement of the low-energy degrees of freedom in the IR, seemingly at odds with conventional c-theorem intuition. This is made possible by the periodic potential, as the theorem relies on translational invariance and thus does not apply [150]. Such a multiplication of time scales may help explain the long-standing conundrum of the concomitant T-linear longitudinal resistance and

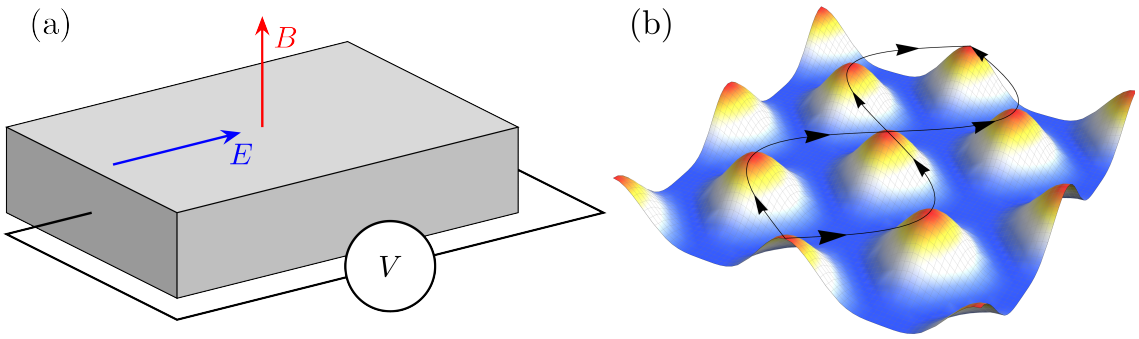

Figure 5.3: (a) Setup for measuring magnetotransport, e.g., the magnetoresistance $\rho_{xx}(B)$. (b) Schematic illustration of effective medium-type current flow (lines) over a sample with regions of varying conductivity (surface). This influences the magnetotransport due to contributions from the Lorentz force.

quadratic Hall angle [151] $\cot\Theta_H = \sigma_{xx}/\sigma_{xy} \sim T^2$ in strange metals[13] [152].

The emergent Drude peak, which appears at large T/G, leads to an enhanced global DC conductivity. This can also be understood from a horizon flow analysis: by inspecting the local current $J^i(x, y)$, we find that it preferentially flows into regions where the local conductivity is large, effectively taking the path of least resistance. This picture provides an intuitive understanding of why this effect only appears in two-dimensional periodic potentials. The same conclusion also follows from the horizon Stokes equations (5.7): in the large T/G-limit, the heat conservation equation reduces to the incompressibility condition $\partial_i v^i = 0$, which enforces a spatially constant flow profile in one but not in two dimensions.

This curved path of least resistance has implications for magnetotransport, as illustrated in Figure 5.3. When the current meanders through an inhomogeneous medium, the Lorentz force generated by the external magnetic field can affect the global longitudinal response. This mechanism underlies "effective medium" models of strange metals, where locally quantum critical regions with slightly different parameters are combined to reproduce the experimentally observed crossover [58–60] to a B-linear magnetoresistance $\rho(B)$ [153]. Such constructions, however, are phenomenological, and the desired B-linear scaling is only realized in the equipartitioned two-component case [154]. The model in Paper III, which also displays an extended roughly linear-in-B regime, instead has the effective medium behavior emerge dynamically from the spatially modulated potential itself, which raises the possibility of a unified description of thermoelectric and magnetotransport within a single framework.

[13] In Fermi liquid metals, the Hall angle is obtained from the same momentum-relaxing time scale as the longitudinal resistivity, $\rho_{xx} \sim \cot\Theta_H \sim \tau^{-1}_{\text{mom. rel.}} \sim T^2$. [152]

6

Dynamical electromagnetism

"Quick as lightning"

Razor

So far, we have considered how the current of the boundary theory responds to an external gauge field. This is sufficient for computing transport coefficients such as the electrical conductivity as in (5.12), but it does not describe truly dynamical electromagnetism. For that to be the case, the boundary gauge field $\mathcal{A}_\mu$ must itself become a propagating degree of freedom obeying Maxwell's equations. This is the topic of the present chapter, and a central ingredient in Papers IV and V.

6.1 Dynamical boundary conditions

The bulk Einstein-Maxwell action (4.5) is, by construction, invariant under local U(1) gauge transformations. For the entire theory to be gauge invariant, the boundary term (4.9) must also vanish under a pure gauge transformation $\delta A_\mu = \partial_\mu \lambda$. Upon partial integration in the boundary coordinates, this reduces to the condition $\partial_\mu \mathcal{J}^\mu = 0$, stating that the boundary current must be conserved. This is the standard meaning of the common dictionary entry that a local symmetry in the bulk corresponds to a *global* symmetry on the boundary, which, however, paints an incomplete picture [155]. Much of the early holographic literature worked exclusively in this framework. As a consequence, the original holographic superconductors [156] were more precisely models of superfluids instead, since the boundary U(1) symmetry was global rather than local. Only more recently have models of holographic superconductors where the boundary contains a truly dynamical local U(1) gauge theory appeared [157].

How, then, can the boundary source be promoted to a genuine photon field? Once $\mathcal{A}_\mu$ is allowed to propagate, it can no longer be treated as a passive source. A consistent description of a massless spin-1 field requires a local U(1) gauge redundancy to remove the longitudinal polarization, leaving only the physical photon degrees of freedom. The most straightforward way is to add a Maxwell term to the boundary generating functional $W^{(0)} = -i \ln Z^{(0)}_{\mathrm{QFT}}$ of the undeformed theory, which gives

$$Z_{\mathrm{QFT}} = \int \mathcal{D}\mathcal{A}_\mu \, e^{iW^{(0)}[\eta^{(0)}_{\alpha\beta}, \mathcal{A}^{(0)}_\alpha] + i \int \mathrm{d}^{d+1}x \left(-\frac{1}{4}\mathcal{F}^2 + \mathcal{A}_\alpha \mathcal{J}^\alpha \right)} , \tag{6.1}$$

where $\mathcal{F} = \mathrm{d}\mathcal{A}$ with respect to the boundary coordinates. There are now two approaches that lead to the same result. The first is to still consider the original source for the current $\mathcal{A}^{(0)}_\alpha$, which equals the boundary value of the bulk gauge field, as an auxiliary source field separate from the boundary photon $\mathcal{A}_\alpha$. One can then integrate out the photon by completing the square. Dropping the stress tensor contribution for brevity, this results in a new energy functional

$$-i \ln Z_{\mathrm{QFT}} = W[\mathcal{A}^{(0)}_\alpha] = \frac{1}{2} \int \mathrm{d}^{d+1}x \, \left[\mathcal{A}^{(0)}_\alpha - \mathcal{J}^\beta \mathcal{V}_{\alpha\beta} \right] \mathcal{J}^\alpha , \tag{6.2}$$

where the photon propagator $\mathcal{V}_{\alpha\beta} = [\eta_{\alpha\beta} k^2 - (1-\xi) k_\alpha k_\beta]/k^4$ in momentum space, with k_α the 4-momentum and ξ a gauge fixing parameter[1]. The resulting deformation then takes the form of a double-trace deformation[2] which does not change the identification of the boundary current [159, 160]. However, the interpretation of (6.2) is that the source for the operator $\mathcal{J}^\alpha$ is now the term in brackets. Consequently, it is this source that should be fixed in order to compute the n-point functions of $\mathcal{J}^\alpha$.

The other approach, which we adopt in Paper IV, takes a more physical point of view: allow the original source term $\mathcal{A}^{(0)}_\alpha$ to be interpreted as the actual dynamical gauge field $\mathcal{A}_\alpha$ on the boundary, and let the added term $\mathcal{A}_\alpha \mathcal{J}^\alpha \to \mathcal{A}_\alpha \mathcal{J}^\alpha_{\mathrm{ext}}$ in (6.1). This introduces the external current $\mathcal{J}^\alpha_{\mathrm{ext}}$, which is distinct from the internal current $\mathcal{J}^\alpha$ of the strongly correlated medium. As in classical electrodynamics, the total current is given by the sum of the two contributions. There is no need here to integrate out the photon, and we can simply consider

$$W[\mathcal{A}_\alpha] = \frac{1}{2} \int \mathrm{d}^{d+1}x \, \left(\mathcal{A}_\alpha \mathcal{J}^\alpha - \frac{1}{4}\mathcal{F}^2 + \mathcal{A}_\alpha \mathcal{J}^\alpha_{\mathrm{ext}} \right) . \tag{6.3}$$

[1] In order to invert the operator in front of the $\mathcal{A}^2$-term in (6.1), one adds an additional gauge-fixing term $(\partial^\alpha \mathcal{A}_\alpha)^2/(2\xi)$ to the Lagrangian [158]. The parameter ξ drops out of any observable.

[2] For a general non-Abelian gauge theory, the operator $\mathcal{O}$ (here $\mathcal{O} = \mathcal{J}^\alpha$) involves a trace over the gauge group. The addition of a term $\sim \mathcal{O}^2$ is therefore a "double-trace" deformation.

The inclusion of these terms to the boundary generating functional corresponds to additional boundary terms in the gravitational theory. Upon partial integration, the variation of the gauge part of the bulk action now leads to[3]

$$\delta S_A = \oint_{r\to 0} \mathrm{d}^{d+1}x\, \delta\mathcal{A}_\alpha \left[\mathcal{J}^\alpha + \nabla_\beta \mathcal{F}^{\beta\alpha} + \mathcal{J}^\alpha_{\text{ext}}\right] + \delta S_{A,\text{bulk}}\,, \tag{6.4}$$

where we have re-written the boundary values of the bulk fields in terms of the boundary fields in calligraphic font. On-shell, the bulk term $S_{A,\text{bulk}}$ vanishes by the bulk equations of motion. A consistent variational problem can now be obtained by taking the term in brackets to be zero, allowing the boundary value $\delta\mathcal{A}_\alpha$ to be non-zero. At the level of the equations of motion, we must therefore impose the boundary condition

$$\left(\nabla_\beta \mathcal{F}^{\alpha\beta} - \mathcal{J}^\alpha\right)\Big|_{r=0} = \mathcal{J}^\alpha_{\text{ext}}\,. \tag{6.5}$$

Since the indices here only run over the boundary directions and $\mathcal{J}^\alpha$ is directly related to $\partial_r A_\alpha$ at the boundary, (6.5) takes the form of a Robin-type, mixed boundary condition for the bulk gauge field. Thus, in practical terms, Dirichlet boundary conditions fix the (external) gauge field, whereas mixed boundary conditions allow it to evolve dynamically.

The explicit external current on the right hand side of (6.5) identifies the source s_α in the (momentum space) linear response relation

$$\mathcal{J}^\alpha = -\chi^{\alpha\beta} s_\beta\,, \qquad s_\alpha = \mathcal{V}_{\alpha\beta}\mathcal{J}^\beta_{\text{ext}}\,. \tag{6.6}$$

The physical source is therefore the external current screened through the photon propagator $\mathcal{V}_{\alpha\beta}$. By comparing with the response function to an external field, $\mathcal{J}^\alpha = -\Pi^{\alpha\beta}\mathcal{A}_\beta$ (e.g., as in a computation of the conductivity), the screened density-density response takes the form

$$\langle\rho\rho\rangle = \chi^{tt} = \frac{\Pi^{tt}}{1 - \frac{1}{\boldsymbol{k}^2}\Pi^{tt}}\,. \tag{6.7}$$

This resembles the RPA approximation familiar from condensed matter physics [72]. However, the function $\Pi^{\mu\nu}$ has a rather different interpretation in the holographic approach. While it normally corresponds to the one-loop particle-hole bubble describing the response of quasiparticles [72], it is here a retarded Green's function of an already strongly interacting medium [161]. The subsequent resummation represented by the denominator therefore promotes an already collective excitation into a propagating electromagnetic collective mode: the *plasmon*, which we will discuss in the following section.

[3] We freely switch to boundary indices α, β here, since $\mathcal{J}^r = 0$ (cf. Footnote 6 on page 34), and we keep $\mathcal{J}^\alpha_{\text{ext}}$ fixed.

These boundary conditions thus enable the study such collective excitations [106–108, 162–168], and provide access to fully dynamical magnetohydrodynamics[4] [171, 172]. Analogous modifications of the graviton boundary conditions can also give dynamical gravity on the boundary [173, 174]. A change of boundary conditions therefore provides a general mechanism for coupling conserved currents to dynamical fields in holography.

Note that we specifically chose not to introduce an explicit electromagnetic coupling constant in the deformation above, e.g., with a prefactor $1/e^2$ in the kinetic term. It is advantageous to instead absorb this factor into the definition of the boundary fields and currents, which ensures that the plasma frequency can be identified consistently both from the pole of the screened response function (6.7) and as the zero of the dielectric function, as discussed in Paper IV. With this choice, the correlator $\Pi^{\mu\nu}$ naturally scales as e^2, which recovers the standard textbook expressions in (6.7) upon factoring out this overall normalization.

6.2 Bulk plasmons

The boundary condition (6.5) is simply Maxwell's equations for the boundary electromagnetic field. In the absence of an external current, the non-trivial solutions to these equations comprise self-sustained electromagnetic modes. These are either photons, which correspond to transverse excitations with vanishing induced current, or plasmons: longitudinally polarized collective modes that arise when charge fluctuations in a polarizable medium couple to the electromagnetic field. For such modes, the electric field $\mathcal{E}$ is generated entirely by the induced polarization $\mathcal{P}$, making the displacement field $\mathcal{D} = \varepsilon_0\mathcal{E} + \mathcal{P} = 0$; equivalently, the longitudinal dielectric function $\varepsilon_L(\omega, \boldsymbol{k}) = 0$. Their behavior is captured by the screened density-density response function (6.7), which correspondingly can be rewritten as

$$\chi^{tt}(\omega, \boldsymbol{k}) = \frac{\Pi^{tt}(\omega, \boldsymbol{k})}{\varepsilon_L(\omega, \boldsymbol{k})}\,, \tag{6.8}$$

showing explicitly that the plasmon pole corresponds to the vanishing of the dielectric function. To distinguish them from the surface modes discussed below, we refer to these excitations as *bulk* plasmons.

Figure 6.1(a) shows the imaginary part of the screened density-density response function χ^{tt} in an AdS_4 Reissner-Nordström model at $T = 0.1\mu$ and with coupling $e = 1$. The exact bulk plasmon dispersion, shown in panel (b), is obtained by solving for the quasinormal modes $\omega(k) \in \mathbb{C}$ for which there exists a non-trivial solution when all sources are set to zero, as discussed in Section 4.4. Both panels reveal the existence of a gapped mode, dispersing approximately

[4] Dynamical electromagnetism can also be equivalently obtained through Dirichlet boundary conditions for a 2-form field dual to the bulk gauge field [169, 170].

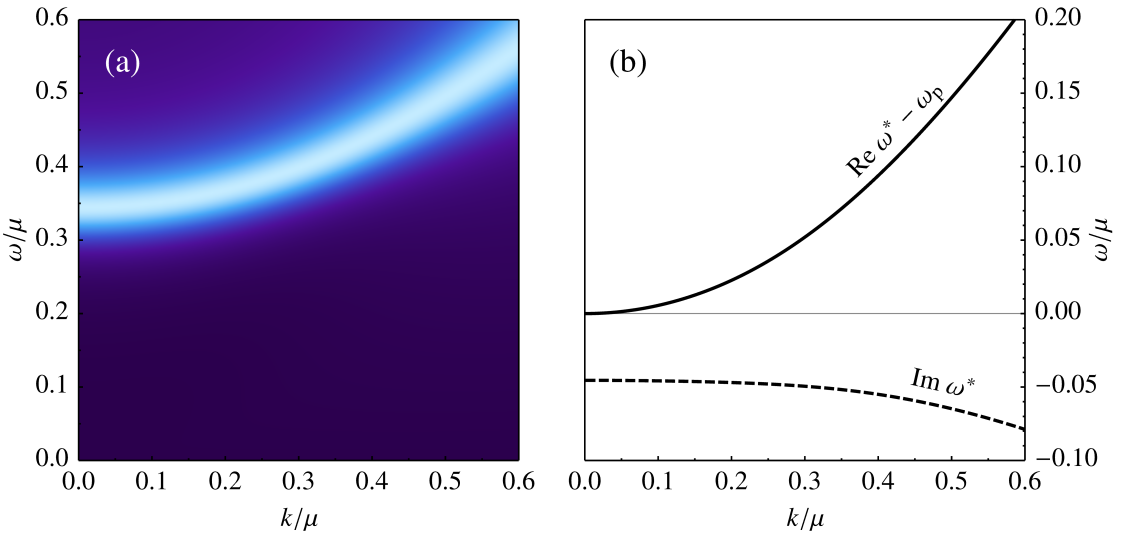

Figure 6.1: (a) Imaginary part of the screened density-density response function $-\operatorname{Im}\chi^{tt}(\omega, k)$ obtained in a holographic AdS_4 RN model at a temperature $T = 0.1\mu$. The function has been normalized to its peak value for each value of k for visibility, and lighter colors indicate a larger value. (b) Corresponding exact dispersion $\omega^*(k)$ of the holographic bulk plasmon. The real part has the plasma frequency $\omega_\mathrm{p} \equiv \operatorname{Re}\omega^*(k = 0)$ subtracted for clarity. The imaginary part shows the significant damping of the plasmon even at $k = 0$.

quadratically with momentum. While this resembles the conventional bulk plasmon in condensed matter textbooks [41, 65], it differs significantly in the imaginary part, where there is finite damping even at zero momentum [106]. In conventional Fermi liquids, damping arises only at momenta large enough for the plasmon to decay into particle-hole pairs inside the so-called Lindhard continuum. The decay in holographic models, which from the bulk point of view is caused by dissipation into the black hole, has been interpreted as a "quantum critical continuum" that extends throughout the entire momentum space [108].

Similar damped plasmons have also been obtained in SYK-like models [175]. There, however, the long-range Coulomb interaction introduces explicit momentum dependence into an otherwise locally critical 0+1-dimensional theory, making the plasmon sector no longer exactly solvable in the original SYK sense. The finite-momentum plasmon response therefore represents one example of where holographic approaches are more naturally suited.

Experimentally, the plasmon response of strange metals has been probed using both optical spectroscopy [176] and momentum-resolved electron energy-loss spectroscopy (M-EELS) [61, 64, 177]. These measurements reveal a plasmon near $k = 0$ that is unusually broad and strongly damped[5]. While quantitative

[5] A reconciliation of the different data generated some debate [178, 179], which now appears to have been settled [180, 181] with the consensus that there exists a broad, incoherent plasmon near $k = 0$, that decays very rapidly at larger momenta.

agreement is not expected for such a simple model as bare AdS-RN holography, where lattice effects, band structure, and the layered geometry of the materials[6] are absent, it is nevertheless remarkable how the dynamics of the black hole provides a mechanism that allows for a large damping even at zero momentum.

Out of the experimental techniques that probe the plasmon response, it is arguably M-EELS that provides the most information, as it measures it throughout frequency and momentum space, nowadays at meV precision [183]. However, M-EELS is inherently a surface probe, and captures both the surface and bulk response of the material [62]. A complete description of strange metal plasmons using holographic models therefore requires the incorporation of the surface response, which is the topic of the next section.

6.3 Surface plasmon polaritons

A key idea from the previous sections is that by setting all components of the external source s_α to zero, we are demanding that the boundary theory satisfies Maxwell's equations in the absence of an external current. This formulation allows one to go beyond the computation of the n-point functions of the boundary theory, and to consider other, more general computations involving electromagnetism in a medium with strong correlations.

In addition to bulk plasmons, metals can also support collective electromagnetic modes localized near their surface. These are known as *surface plasmon polaritons* (SPPs): hybrid excitations in which surface charge oscillations couple to electromagnetic waves propagating along the interface [184]. The term polariton emphasizes that the mode is part matter excitation and part photon. Since the bulk plasmon behaves anomalously in strange metals, one may expect similarly unconventional surface excitations.

The SPP is, just as the bulk plasmon, controlled by the dielectric response of the medium, captured in the dielectric function $\varepsilon(\omega, \boldsymbol{k})$: within a local ($k$-independent) approximation, the dispersion below the plasma frequency is given by [184]

$$k_{\mathrm{SPP}} = \frac{\omega}{c}\sqrt{\frac{\varepsilon(\omega)\varepsilon_1}{\varepsilon(\omega)+\varepsilon_1}}\,, \tag{6.9}$$

where k here refers to the component of the total wave vector tangent to the material surface, and ε_1 is the dielectric constant of the surrounding medium, e.g., air. The prototypical SPP dispersion is shown in Figure 6.2(a): at small frequencies and wave vectors, the excitation follows the light line $\omega = ck$, reflecting its photonic character. In the limit of large wave vectors, retardation

[6] A simple holographic model incorporating layered structure was proposed in [107], which shows an acoustic plasmon mode qualitatively similar to experiments using angle-resolved photon emission spectroscopy [182].

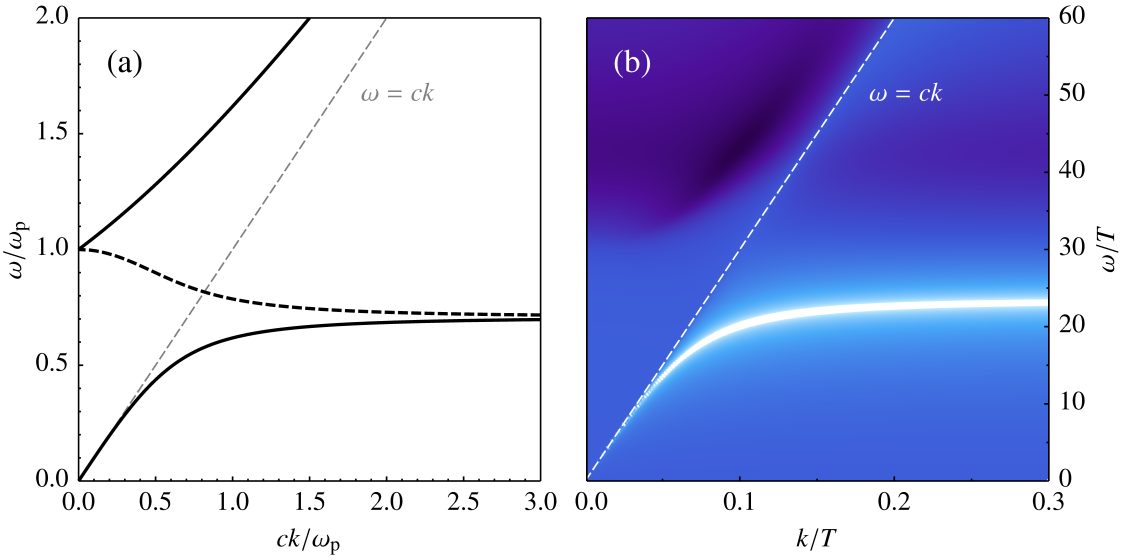

Figure 6.2: (a) Textbook SPP dispersion for a conventional metal, (6.9), using a Drude model for $\varepsilon(\omega)$ and $\varepsilon_1 = 1$. The upper branch is the bulk plasmon-polariton. (b) Logarithm of the reflection coefficient as computed self-consistently within a holographic AdS_5-RN model in Paper IV. Lighter colors indicate larger values. In both figures, k refers to the in-plane wave vector component of the surface excitation.

effects become negligible and the mode crosses over to the quasi-static *surface plasmon*, with characteristic surface plasmon frequency $\omega_{\rm sp} < \omega_p$. Above the plasma frequency, the metal is effectively transparent to transverse electromagnetic waves, which gives rise to the upper, *bulk plasmon-polariton* branch of the dispersion relation.

Unlike the bulk plasmon, which appears as a pole in the screened density-density response function (6.8), an SPP is excited only under specific electromagnetic boundary conditions. This prevents a description of it in terms of a simple two-point correlator, which the holographic framework excels at computing. In order to model SPPs holographically, we consider an electromagnetic wave impinging on the surface of a strongly correlated system, and use the reflection coefficient R — the ratio of the reflected and incoming waves' amplitudes — as the natural response function for surface excitations. The SPPs then manifest as poles in the reflection coefficient [185]. Furthermore, in the non-retarded limit, relevant for the electrons in M-EELS experiments, the reflection coefficient reduces to the surface response function[7],

$$R \xrightarrow{\omega \ll ck} g(\omega, k) = \int_{-\infty}^{0} \int_{-\infty}^{0} \mathrm{d}z\, \mathrm{d}z' \chi^{tt}(\omega, k; z, z') e^{|k|z} e^{|k|z'} \,, \tag{6.10}$$

which encodes the integrated density response near the surface. This func-

[7] This is true for a p-polarized incoming wave [185].

tion is the analogous quantity to the longitudinal dielectric function for bulk excitations [185], and is directly related to the signal measured in M-EELS experiments [62]. Taking the additional local limit $k \to 0$ of (6.10), one obtains $\mathrm{Im}\, g \to \mathrm{Im}(\varepsilon(\omega) + \varepsilon_1)^{-1}$, which carries the same pole structure as (6.9), thus reproducing the standard surface plasmon condition in this limit.

We evaluate the reflection coefficient in AdS_5 holographic models in Paper IV, an example of which is shown in Figure 6.2(b). The lower branch displays the expected SPP behavior: at small wave vectors it is tangent to the light line $\omega = ck$, while at large momentum it crosses over toward an approximately fixed surface plasmon frequency ω_{sp}. The bulk plasmon-polariton appears in our setup as a suppression in the reflection coefficient, reflecting that the energy is absorbed into a propagating bulk mode. A key part of this approach is that it does not rely on a local dielectric function or a constant magnetic permeability as for the approximate solution (6.9), but instead computes the full non-local electromagnetic response self-consistently. This illustrates that the holographic framework can successfully capture the crossover between photonic and electrostatic regimes, and is able to address surface electromagnetic phenomena in strongly correlated systems. Combined with the holographic results for bulk and other types of plasmons, this sets the stage for a more complete electromagnetic description of strongly correlated quantum matter.

6.4 Plasmons in ersatz Fermi liquids

In all holographic models discussed so far, finite density matter is captured by a non-zero background charge density due to the charge of the Reissner-Nordström black hole, as in (4.12). While this provides a simple description of compressible quantum matter, its interpretation in an electronic system is not straightforward. In particular, the conserved charge in holography need not coincide with the microscopic electron charge, but may instead represent an emergent collective charge sector[8]. A further subtlety is that part or all of the charge resides behind the black hole horizon. This implies that the Fermi surface as seen from the boundary does not account for the full microscopic charge density, leading to an apparent violation of Luttinger's theorem [187], which normally relates the Fermi surface volume $\mathcal{V}_F$ to the charge density as

$$\frac{\mathcal{V}_F}{(2\pi)^d} = \rho\,. \tag{6.11}$$

Motivated by this, Paper V builds on the framework of *ersatz Fermi liquids* introduced in [188], which aims to place conventional Fermi liquids and

[8] One may draw an analogy with fractionalized Fermi liquid phases, where only part of the total charge is carried by quasiparticle excitations, which coexist with a strongly correlated fractionalized sector [186].

non-Fermi liquids within a common description. Rather than relying on quasiparticles, metallic states are characterized through their symmetry structure and anomalies. In this approach, Luttinger's theorem is built-in from the start, which is therefore also true for holographic formulations of ersatz Fermi liquids. Such holographic models therefore provide a fresh perspective on strongly correlated systems at finite density.

6.4.1 An 't Hooft anomaly

To illustrate the underlying logic of ersatz Fermi liquids, consider a system of non-interacting massive fermions in one spatial dimension with a parabolic dispersion $\epsilon_k = \hbar^2 k^2/2m$. The microscopic description, which is invariant under a global U(1) symmetry, is given by

$$H = \int \mathrm{d}x \left[-\frac{1}{2m} \Psi^\dagger \nabla \Psi - \mu \Psi^\dagger \Psi \right] , \tag{6.12}$$

where a non-zero chemical potential μ yields a finite density of fermions. The ground state (Fermi surface) is obtained by filling all momentum states until the fermion energy $\epsilon_k = k^2/(2m) = \mu$, as is illustrated in Figure 6.3(a).

Although the microscopic ultraviolet description is fully known in this simple model, many-body systems are instead often described by their low-energy infrared theory — for example, in terms of quasielectrons and phonons. In the present case, it can be obtained by linearizing around the Fermi surface $k_{L/R} = \pm k_F$. The result, shown in Figure 6.3(b), is an effective theory in terms of linearly dispersing, massless (Dirac) fermions at *zero* charge density. Because the low-energy theory only resolves momenta within a cutoff $\Lambda \ll k_F$, no scattering processes can move the fermions very far in momentum space, making the charges at the two Fermi surface points k_L and k_R separately conserved. The infrared symmetry G_{IR} is therefore enlarged from the microscopic global U(1) to the chiral $G_{\mathrm{IR}} = \mathrm{U}(1)_L \times \mathrm{U}(1)_R$ [189]. Accordingly, there exist two separately conserved Noether currents J^α_L and J^α_R.

If an external electric field is applied, the fermions will start drifting. From the UV point of view, this process simply amounts to fermions "hopping" to adjacent momentum states, such that the net momentum of all fermions corresponds to that of the force exerted by the electric field. However, from the infrared perspective, the electric field results in a transfer of charge between left- and right-moving sectors, thus breaking the separate conservation[9]. This chiral anomaly is captured by the equations

$$\partial_\alpha J^\alpha_L = -\frac{E}{2\pi} , \qquad \partial_\alpha J^\alpha_R = \frac{E}{2\pi} , \tag{6.13}$$

[9] From the IR point of view, these extra charges seem to come from the infinite Fermi sea. Only in the UV picture do we see that this sea is in fact not infinite.

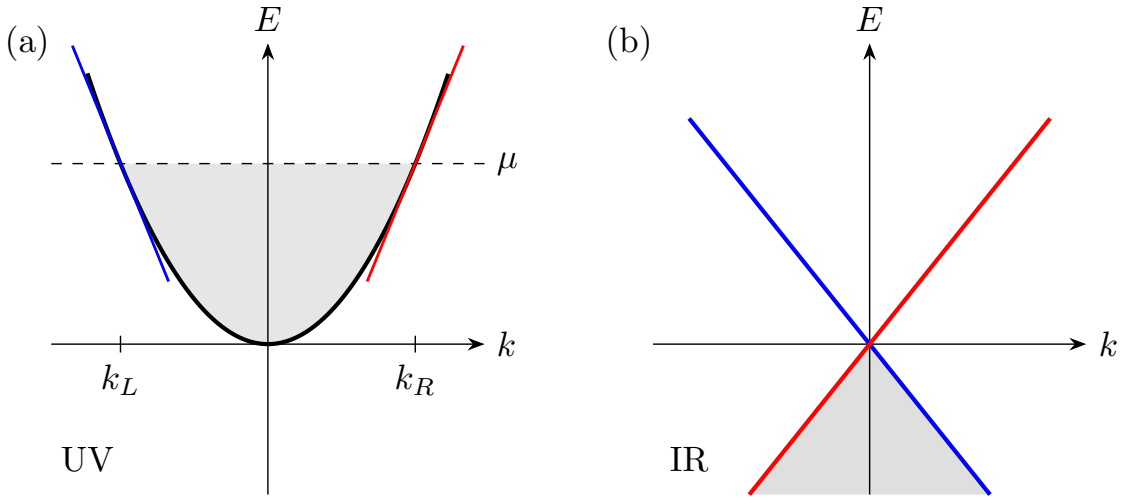

Figure 6.3: (a) Dispersion of non-interacting, 1D fermions subject to a chemical potential μ. The Fermi surface consists of two distinct points, k_L and k_R. (b) The corresponding IR effective theory. The Fermi sea is shown in gray.

and can be interpreted as an 't Hooft anomaly of the emergent IR symmetry, preventing the theory from being gauged. In both cases, the total charge is of course conserved — the 't Hooft anomaly appears only in the effective infrared description of the system, not in the full microscopic theory. Nevertheless, it encodes information about the underlying Fermi surface inherited from the ultraviolet theory. This is the key concept that allows for a formulation of metals without alluding to quasiparticles.

6.4.2 Fermi surfaces in two dimensions: LU(1)

In two dimensions, the same logic generalizes naturally. The two Fermi points are replaced by a continuous Fermi surface, parametrized by an angle $\theta \in S^1$. As a result, the emergent infrared symmetry is enlarged to the infinite-dimensional group $G_{\text{IR}} = \text{LU}(1)$, the loop group consisting of all smooth functions from the circle S^1 onto U(1). This describes the conservation of charge at each point on the Fermi surface [188].

But what about interactions — would they not break this separate conservation? As discussed in Chapter 2, generic interactions are irrelevant in the RG sense [67–69], except for the kinematical channels that correspond to either the BCS instability[10] or forward scattering. Thus, in the absence of superconductivity and additional gapless modes, one expects an emergent LU(1) symmetry in the deep IR [188]. This is the central argument for ersatz Fermi liquids serving as a framework underlying both Fermi and non-Fermi liquids.

[10] Whether this is marginally relevant or irrelevant depends on loop corrections.

Recently, this structure was implemented in a holographic effective theory [190], which builds in a Fermi surface through the anomaly equation

$$\partial_a \mathcal{J}^a(x^\alpha, \theta) = \frac{m}{8\pi^2}\epsilon^{abcd}\partial_a \mathcal{A}_b \partial_c \mathcal{A}_d \,, \qquad \mathcal{A}_a(x^\alpha, \theta) = (\mathcal{A}_\alpha, \mathcal{A}_\theta) \,. \tag{6.14}$$

This is the LU(1) generalization of (6.13), where the current and gauge field here are θ-resolved densities, and the gauge field now includes an additional $\mathcal{A}_\theta$-component parameterizing the Fermi surface[11]. This anomaly can alternatively be formulated via anomaly inflow from a higher-dimensional manifold containing a Chern-Simons term, which naturally suggests a holographic construction. Such a construction will therefore contain a Fermi surface satisfying Luttinger's theorem through the anomaly equation, but also exhibit a lack of quasiparticles due to the strong correlations inherent in holographic models.

As we saw in the previous subsection, the effective IR theory is at zero charge density. Nevertheless, the Fermi surface clearly contains charge. A natural next question therefore concerns collective charge oscillations. As discussed throughout this chapter, plasmons arise when the conserved global U(1) charge is promoted to a dynamical gauge symmetry through coupling to electromagnetism. Although the LU(1) group is anomalous and cannot be gauged, we show in Paper V that there exists an anomaly-free U(1) subgroup corresponding to the total charge. In order to gauge this subgroup, we use the periodicity of the Fermi surface to expand the bulk gauge field into Fourier modes as

$$A_M(x^\mu, \theta) = \sum_{n\in\mathbb{Z}} A_M^{(n)}(x^\mu) e^{in\theta} \,, \qquad A_M = (A_\mu, A_\theta) \,, \tag{6.15}$$

and similarly also for the boundary current $\mathcal{J}^\alpha(x^\alpha)$. The zeroth angular harmonic describes the total, conserved charge[12], since

$$\partial_\alpha \mathcal{J}^\alpha(x^\alpha) = \frac{1}{2\pi}\int \mathrm{d}\theta\, \partial_\alpha \mathcal{J}^\alpha(x^\alpha, \theta) = \partial_\alpha \mathcal{J}^\alpha_{(0)}(x^\alpha) = 0 \,, \tag{6.16}$$

where the zero comes from integrating the right-hand-side of (6.14). Dynamical boundary conditions can therefore be imposed for the zeroth angular harmonic to gauge the U(1) subgroup and implement dynamical electromagnetism. A central result of Paper V is that this construction indeed gives rise to a plasmon, even in the absence of a charged background geometry (i.e., at $\mu = 0$). The gap for the plasmon mode at zero momentum (i.e., the plasma frequency) is set by the charge contained in the Fermi surface, and similar to the typical holographic bulk plasmon, there is an appreciable damping already at zero momentum.

[11] In a conventional Fermi liquid, $\mathcal{A}_\theta$ can be interpreted as the Berry phase accumulated as a quasiparticle is transported around the Fermi surface [189].

[12] A requirement of LU(1) symmetry is that $\mathcal{J}^\theta = 0$; otherwise it would imply the existence of dynamic non-forward scattering [190]. Thus $\partial_\alpha \mathcal{J}^\alpha = \partial_a \mathcal{J}^a$, whereby (6.14) can be used.

The expansion into angular modes is reminiscent of the treatment of the Fermi surface deformations in Chapter 3, but the two should not be compared too literally. In the kinetic description, all angular modes contribute to the total distribution function $f(t; \boldsymbol{r}, \boldsymbol{p})$, which gives the particle density upon integration over the Fermi surface. Only the zero mode can change the total density, and will therefore couple to density perturbations. The $m = \pm 1$ modes instead correspond to momentum, and thus to the electrical current. In the LU(1) approach, by contrast, $\mathcal{J}^{\mu}(x^{\alpha}, \theta)$ represents a θ-resolved charge-current density associated with the emergent LU(1) symmetry. Its zero mode directly gives both the total charge and the electrical current, via its time and spatial components, while the higher modes integrate to zero.

Part III
Final remarks

7
Conclusions

"So begins... the final epoch"

Faceless Void

Describing condensed matter systems is a daunting task. In this thesis, we have approached the problem from two distinct viewpoints: one firmly rooted in Landau's quasiparticle description, and one that utilizes the exotic physics of black holes and the holographic duality. Together, these perspectives provide complementary insights into the dynamics of interacting quantum matter, bridging weakly and strongly coupled regimes. In this final chapter, we summarize the main findings and outline several directions for future work.

7.1 Main findings

In Paper I, we extend earlier work on the spectrum of the electron-electron collision operator by incorporating a screened Coulomb interaction, providing a more realistic description of electron scattering. By studying the entire spectrum, we find that only a small subset of modes relax at a suppressed rate $\gamma_m \sim T^4/T_F^3$, namely, the lowest-lying odd-parity modes of angular mode number $m \geq 3$. The lowest-lying even-parity modes, along with all higher eigenmodes, instead exhibit the standard $\gamma_m \sim T^2/T_F$ scaling. We further demonstrate that the separation between the slow and fast modes can be tuned by the strength of the Coulomb interaction, which may enable experimental realizations of the tomographic regime.

Notably, there is no logarithmic enhancement of the lowest-lying even-parity decay rates, in contrast to the quasiparticle lifetimes obtained from self-energy calculations. This is particularly important for transport, which is governed by the relaxation dynamics of collective deformations rather than by those of

single quasiparticles. An important example is the shear viscosity studied in Paper II, which is controlled by the quadrupole relaxation rate $\gamma_{m=2}$. The calculation of the shear viscosity also exemplifies the strength of the method presented in Paper I, as it applies to all temperatures and captures the full ballistic-to-hydrodynamic crossover.

On the other side of the spectrum, we studied strongly correlated systems. In Paper III, we demonstrate that strong translational symmetry breaking in quantum critical systems can give rise to an emergent effective medium description. This has important consequences for magnetotransport, where a meandering, inhomogeneous current flow can result in an approximately linear-in-B longitudinal magnetoresistance. Furthermore, we find that a local hydrodynamic description emerges within individual regions of the system, which reintroduces a weak Drude peak in the global electrical and thermal conductivities. These emergent transport channels provide a possible mechanism for multiple transport time scales in strange metals.

In Paper IV, we develop a framework for boundary electrodynamics in holographic models, incorporating both longitudinal and transverse responses, as well as the effects of a finite speed of light. This allows us to study electromagnetic response beyond two-point functions, including surface phenomena via the reflection coefficient. In particular, we show how both bulk and surface plasmons emerge from this description, providing a bridge between holographic models and experimentally relevant probes such as M-EELS.

Finally, in Paper V, we incorporate the symmetry structure of a Fermi surface into a holographic framework through an emergent LU(1) symmetry. By gauging its anomaly-free U(1) subgroup, we demonstrate the existence of a plasmon mode even in the absence of a charged background geometry. This shows that the charge encoded in the Fermi surface degrees of freedom gives rise to the expected collective dynamics, providing a non-trivial consistency check of the construction.

7.2 Outlook

The results presented in this thesis open up multiple avenues for future research, which includes the following.

Observable proxies of tomographic transport
The mathematical method presented in Paper I enables the computation of a wide range of observables beyond the shear viscosity studied in Paper II. This includes the thermoelectric transport and magnetotransport coefficients, as well as the density-density response we explored in the holographic models of Part II. In this pursuit, it would be particularly interesting to study observables that couple to the long-lived odd-parity modes, and would therefore show signs of the tomographic regime. These include, most notably, any momentum-resolved

probe; for instance, a non-trivial scaling of the non-local conductivity was recently revealed in Ref. [96]. Furthermore, the full spectrum of modes obtained in Paper I will be especially important for thermal transport, which is sensitive to the higher-lying modes that cannot be obtained from self-energy calculations. Further work could also extend the screened Coulomb interaction considered in Papers I and II to a more general interaction, in order to resolve effects of finite energy transfer. Finally, a key open question pertains to the robustness of the odd-even effect in the presence of impurities and phonons, which are unavoidable in realistic systems.

Holographic effective medium theory
An extension of the effective medium picture developed in Paper III to systems at finite average charge density would allow for a study of coupled charge and heat transport, including the Hall response. A central question is whether the emergent effective medium description, and the associated linear-in-B magnetoresistance, persists in this more general setting. If so, a magnetic Gubser-Rocha model could potentially produce a magnetoresistance of quadrature form, $\rho \sim \sqrt{T^2 + B^2}$, as observed in experiments [58–60]. Due to the apparent emergence of multiple time scales, it will be particularly interesting to investigate the Hall response, since it has been argued that two time scales could explain the concomitant T-linear resistivity and T^2 Hall angle in the cuprate strange metals [191].

Plasmons in lattices
Combining the ideas of Papers III and IV, it is straightforward to analyze the density response in a system with strong translational symmetry breaking from the lattice. Earlier studies of holographic plasmons with isotropic translational symmetry breaking revealed a "fake" plasmon [165]: another peak that does not scale with the charge density of the system. If such an excitation remains in the lattice setting, it could plausibly admit a description in terms of Umklapp hydrodynamics. A hybridization between multiple modes in this fashion could potentially help explain the continuum underlying the plasmon peak in the density response in strange metals [61, 177].

Adding an explicit lattice would also constitute a clear step in the direction of more realistic models. Combined with the ideas to incorporate the layered nature of cuprate strange metals employed in Refs. [168, 192], and the description of the surface response in Paper IV, it would provide a more realistic holographic framework for interpreting the experimental data.

An RG-complete geometry of holographic LU(1) models
The effective holographic LU(1) model employed in Paper V captures the infrared symmetry structure of a Fermi surface, but does not describe the full renormalization group flow from the ultraviolet. Constructing a geometry that interpolates between a UV theory and an LU(1)-symmetric IR fixed point would provide a more complete description and allow for a dynamical coupling between

gravitational and Fermi surface degrees of freedom. This would also allow one to study the regime where the emergent LU(1) symmetry is weakly broken, through the inclusion of irrelevant operators in the UV.

This concludes the thesis. Thank you for reading.

Bibliography

[1] E. Nilsson, *Electron Transport and Collective Modes in Fermi and non-Fermi Liquids*, Licentiate Thesis (Chalmers University of Technology, 2024).

[2] L. D. Landau, *The Theory of a Fermi Liquid*, Soviet Physics–JETP **3**, 920 (1957).

[3] D. Pines, *Electron interaction in solids*, Canadian Journal of Physics **34**, 1379–1394 (1956).

[4] J. Sólyom, *Fundamentals of the Physics of Solids* (Springer, 2007).

[5] A. Lucas and K. C. Fong, *Hydrodynamics of electrons in graphene*, Journal of Physics: Condensed Matter **30**, 053001 (2018).

[6] C. Kittel, *Introduction to Solid State Physics*, 8th ed (Wiley, Hoboken, NJ, 2005).

[7] P. Coleman, *Introduction to Many-Body Physics* (Cambridge University Press, Cambridge, 2015).

[8] N. E. Hussey, K. Takenaka, and H. Takagi, *Universality of the Mott–Ioffe–Regel limit in metals*, Philosophical Magazine **84**, 2847–2864 (2004).

[9] O. Gunnarsson, M. Calandra, and J. E. Han, *Colloquium: Saturation of Electrical Resistivity*, Reviews of Modern Physics **75**, 1085–1099 (2003).

[10] A. C. Keser, D. Q. Wang, O. Klochan, et al., *Geometric Control of Universal Hydrodynamic Flow in a Two-Dimensional Electron Fluid*, Physical Review X **11**, 031030 (2021).

[11] D. Wang, X.-B. Li, and H.-B. Sun, *Modulation doping: a strategy for 2D materials electronics*, Nano Letters **21**, 6298–6303 (2021).

[12] J. Zaanen, *Electrons go with the flow in exotic material systems*, Science **351**, 1026–1027 (2016).

[13] R. N. Gurzhi, *Minimum of resistance in impurity-free conductors*, Soviet Physics–JETP **44**, 045443–5 (1963).

[14] J. Crossno, J. K. Shi, K. Wang, et al., *Observation of the Dirac fluid and the breakdown of the Wiedemann-Franz law in graphene*, Science **351**, 1058–1061 (2016).

[15] R. Krishna Kumar, D. A. Bandurin, F. M. D. Pellegrino, et al., *Superballistic flow of viscous electron fluid through graphene constrictions*, Nature Physics **13**, 1182–1185 (2017).

[16] D. A. Bandurin, A. V. Shytov, L. S. Levitov, et al., *Fluidity onset in graphene*, Nature Communications **9**, 4533 (2018).

[17] A. I. Berdyugin, S. G. Xu, F. M. D. Pellegrino, et al., *Measuring Hall viscosity of graphene's electron fluid*, Science **364**, 162–165 (2019).

[18] J. A. Sulpizio, L. Ella, A. Rozen, et al., *Visualizing Poiseuille flow of hydrodynamic electrons*, Nature **576**, 75–79 (2019).

[19] A. Jenkins, S. Baumann, H. Zhou, et al., *Imaging the Breakdown of Ohmic Transport in Graphene*, Physical Review Letters **129**, 087701 (2022).

[20] Y. Nam, D.-K. Ki, D. Soler-Delgado, et al., *Electron–hole collision limited transport in charge-neutral bilayer graphene*, Nature Physics **13**, 1207–1214 (2017).

[21] L. W. Molenkamp and M. J. M. De Jong, *Observation of Knudsen and Gurzhi transport regimes in a two-dimensional wire*, Solid-State Electronics **37**, 551–553 (1994).

[22] M. J. M. De Jong and L. W. Molenkamp, *Hydrodynamic electron flow in high-mobility wires*, Physical Review B **51**, 13389–13402 (1995).

[23] A. Gupta, J. J. Heremans, G. Kataria, et al., *Hydrodynamic and Ballistic Transport over Large Length Scales in GaAs / AlGaAs*, Physical Review Letters **126**, 076803 (2021).

[24] G. M. Gusev, A. D. Levin, E. V. Levinson, et al., *Viscous transport and Hall viscosity in a two-dimensional electron system*, Physical Review B **98**, 161303 (2018).

[25] G. M. Gusev, A. S. Jaroshevich, A. D. Levin, et al., *Viscous magnetotransport and Gurzhi effect in bilayer electron system*, Physical Review B **103**, 075303 (2021).

[26] P. J. W. Moll, P. Kushwaha, N. Nandi, et al., *Evidence for hydrodynamic electron flow in $PdCoO_2$*, Science **351**, 1061–1064 (2016).

[27] J. Gooth, F. Menges, N. Kumar, et al., *Thermal and electrical signatures of a hydrodynamic electron fluid in tungsten diphosphide*, Nature Communications **9**, 4093 (2018).

[28] D. A. Bandurin, I. Torre, R. K. Kumar, et al., *Negative local resistance caused by viscous electron backflow in graphene*, Science **351**, 1055–1058 (2016).

[29] P. J. Ledwith, H. Guo, and L. Levitov, *The hierarchy of excitation lifetimes in two-dimensional Fermi gases*, Annals of Physics **411**, 167913 (2019).

[30] P. Ledwith, H. Guo, and L. Levitov, *Angular Superdiffusion and Directional Memory in Two-Dimensional Electron Fluids*, 2019, arXiv:1708.01915.

[31] P. Ledwith, H. Guo, A. Shytov, et al., *Tomographic Dynamics and Scale-Dependent Viscosity in 2D Electron Systems*, Physical Review Letters **123**, 116601 (2019).

[32] J. Hofmann and S. Das Sarma, *Collective modes in interacting two-dimensional tomographic Fermi liquids*, Physical Review B **106**, 205412 (2022).

[33] J. Hofmann and U. Gran, *Anomalously long lifetimes in two-dimensional Fermi liquids*, Physical Review B **108**, L121401 (2023).

[34] J. Hofmann and H. Rostami, *Nonlinear thermoelectric probes of anomalous electron lifetimes in topological Fermi liquids*, Physical Review Research **6**, L042042 (2024).

[35] J. Maki, U. Gran, and J. Hofmann, *Odd-parity effect and scale-dependent viscosity in atomic quantum gases*, Communications Physics **8**, 319 (2025).

[36] N. Ben-Shachar and J. Hofmann, *Magnetotransport of tomographic electrons in a channel*, 2025, arXiv:2503.14431.

[37] N. Ben-Shachar and J. Hofmann, *Tomographic electron flow in confined geometries: Beyond the dual-relaxation time approximation*, 2025, arXiv:2503.14461.

[38] J. Estrada-Álvarez, F. Domínguez-Adame, and E. Díaz, *Generalized Navier-Stokes model for ballistic and tomographic electrons*, Scientific Reports **15**, 38326 (2025).

[39] J. Estrada-Álvarez, E. Díaz, and F. Domínguez-Adame, *Superballistic Paradox in Electron Fluids: Relevance of Tomographic Transport*, Physical Review Letters **135**, 206301 (2025).

[40] J. Maki and J. Hofmann, *Tomographic collective modes in a magnetic field*, 2026, arXiv:2603.06518.

[41] G. F. Giuliani and G. Vignale, *Quantum Theory of the Electron Liquid* (Cambridge University Press, New York, 2005).

[42] J. Zaanen, *Planckian dissipation, minimal viscosity and the transport in cuprate strange metals*, SciPost Physics **6**, 061 (2019).

[43] B. Keimer, S. A. Kivelson, M. R. Norman, et al., *From quantum matter to high-temperature superconductivity in copper oxides*, Nature **518**, 179–186 (2015).

[44] J. Bardeen, L. N. Cooper, and J. R. Schrieffer, *Theory of Superconductivity*, Physical Review **108**, 1175–1204 (1957).

[45] J. G. Bednorz and K. A. Müller, *Possible high T_c superconductivity in the Ba-La-Cu-O system*, Zeitschrift für physik B condensed matter **64**, 189–193 (1986).

[46] P. W. Phillips, N. E. Hussey, and P. Abbamonte, *Stranger than metals*, Science **377**, eabh4273 (2022).

[47] M. Gurvitch and A. T. Fiory, *Resistivity of $La_{1.825}Sr_{0.175}CuO_4$ and $YBa_2Cu_3O_7$ to 1100 K: Absence of saturation and its implications*, Physical Review Letters **59**, 1337–1340 (1987).

[48] D. V. D. Marel, H. J. A. Molegraaf, J. Zaanen, et al., *Quantum critical behaviour in a high-Tc superconductor*, Nature **425**, 271–274 (2003).

[49] S. A. Hartnoll and A. P. Mackenzie, *Colloquium: Planckian dissipation in metals*, Reviews of Modern Physics **94**, 041002 (2022).

[50] A. Legros, S. Benhabib, W. Tabis, et al., *Universal T-linear resistivity and Planckian dissipation in overdoped cuprates*, Nature Physics **15**, 142–147 (2019).

[51] M. Troyer and U.-J. Wiese, *Computational Complexity and Fundamental Limitations to Fermionic Quantum Monte Carlo Simulations*, Physical Review Letters **94**, 170201 (2005).

[52] E. Berg, S. Lederer, Y. Schattner, et al., *Monte Carlo Studies of Quantum Critical Metals*, Annual Review of Condensed Matter Physics **10**, 63–84 (2019).

[53] E. Y. Loh, J. E. Gubernatis, R. T. Scalettar, et al., *Sign problem in the numerical simulation of many-electron systems*, Physical Review B **41**, 9301–9307 (1990).

[54] J. Zaanen, Y. Liu, Y.-W. Sun, et al., *Holographic Duality in Condensed Matter Physics* (Cambridge University Press, Cambridge, 2015).

[55] S. A. Hartnoll, A. Lucas, and S. Sachdev, *Holographic Quantum Matter* (The MIT Press, Cambridge, 2018).

[56] S. Sachdev, *Statistical mechanics of strange metals and black holes*, 2022, arXiv:2205.02285.

[57] F. Balm, N. Chagnet, S. Arend, et al., *T-linear resistivity, optical conductivity, and Planckian transport for a holographic local quantum critical metal in a periodic potential*, Physical Review B **108**, 125145 (2023).

[58] I. M. Hayes, R. D. McDonald, N. P. Breznay, et al., *Scaling between magnetic field and temperature in the high-temperature superconductor $BaFe_2(As_{1-z}$-$P_x)_2$*, Nature Physics **12**, 916–919 (2016).

[59] P. Giraldo-Gallo, J. A. Galvis, Z. Stegen, et al., *Scale-invariant magnetoresistance in a cuprate superconductor*, Science **361**, 479–481 (2018).

[60] J. Ayres, M. Berben, M. Čulo, et al., *Incoherent transport across the strange-metal regime of overdoped cuprates*, Nature **595**, 661–666 (2021).

[61] M. Mitrano, A. A. Husain, S. Vig, et al., *Anomalous density fluctuations in a strange metal*, Proceedings of the National Academy of Sciences **115**, 5392–5396 (2018).

[62] A. A. Husain, *Charge Fluctuations of the Strange Metal in Space and Time*, PhD thesis (University of Illinois at Urbana-Champaign, 2020).

[63] X. Guo, J. Chen, F. Hoveyda-Marashi, et al., *Conformally invariant charge fluctuations in a strange metal*, 2024, arXiv:2411.11164.

[64] N. de Vries, E. Hoglund, D. Chaudhuri, et al., *Reexamining the strange metal charge response with transmission inelastic electron scattering*, 2026, arXiv:2602.02348.

[65] D. Pines and P. Nozières, *The Theory of Quantum Liquids: Normal Fermi Liquids*, 1st ed., Vol. 1 (CRC Press, Boca Raton, 2018).

[66] G. F. Giuliani and J. J. Quinn, *Lifetime of a quasiparticle in a two-dimensional electron gas*, Physical Review B **26**, 4421–4428 (1982).

[67] G. Benfatto and G. Gallavotti, *Renormalization-group approach to the theory of the Fermi surface*, Physical Review B **42**, 9967–9972 (1990).

[68] R. Shankar, *Renormalization-group approach to interacting fermions*, Reviews of Modern Physics **66**, 129–192 (1994).

[69] J. Polchinski, *Effective Field Theory and the Fermi Surface*, 1999, arXiv:hep-th/9210046.

[70] D. Arovas, *Lecture Notes on Thermodynamics and Statistical Mechanics (A Work in Progress)*, 2019.

[71] D. Tong, *Kinetic theory*, 2012.

[72] A. Altland and B. Simons, *Condensed Matter Field Theory*, 3rd ed. (Cambridge University Press, 2023).

[73] T. Kita, *Introduction to Nonequilibrium Statistical Mechanics with Quantum Field Theory*, Progress of Theoretical Physics **123**, 581–658 (2010).

[74] H. J. Haug and A.-P. Jauho, *Quantum Kinetics in Transport and Optics of Semiconductors*, Vol. 123, Solid-State Sciences (Springer Berlin Heidelberg, Berlin, Heidelberg, 2008).

[75] J. Rammer, *Quantum Transport Theory* (CRC Press, 2018).

[76] L. Fritz and T. Scaffidi, *Hydrodynamic Electronic Transport*, Annual Review of Condensed Matter Physics **15**, 17–44 (2024).

[77] E. Nilsson, U. Gran, and J. Hofmann, *Nonequilibrium Relaxation and Odd-Even Effect in Finite-Temperature Electron Gases*, Physical Review X **15**, 041007 (2025).

[78] A. A. Abrikosov and I. M. Khalatnikov, *The Theory of a Fermi Liquid (the Properties of Liquid ^{3}He at low temperatures)*, Reports on Progress in Physics **22**, 329–367 (1959).

[79] G. A. Brooker and J. Sykes, *Transport Properties of a Fermi Liquid*, Physical Review Letters **21**, 279–282 (1968).

[80] H. H. Jensen, H. Smith, and J. W. Wilkins, *Exact transport coefficients for a Fermi liquid*, Physics Letters A **27**, 532–533 (1968).

[81] A. V. Chaplik, *Energy spectrum and electron scattering processes in inversion layers*, Soviet Physics–JETP **33**, 997–1000 (1971).

[82] C. Hodges, H. Smith, and J. W. Wilkins, *Effect of Fermi Surface Geometry on Electron-Electron Scattering*, Physical Review B **4**, 302–311 (1971).

[83] L. Zheng and S. Das Sarma, *Coulomb scattering lifetime of a two-dimensional electron gas*, Physical Review B **53**, 9964–9967 (1996).

[84] T. Jungwirth and A. H. MacDonald, *Electron-electron interactions and two-dimensional–two-dimensional tunneling*, Physical Review B **53**, 7403–7412 (1996).

[85] S. Musser, S. Das Sarma, and J. Hofmann, *Odd relaxation in three-dimensional Fermi liquids*, Physical Review Research **8**, 013176 (2026).

[86] G. B. Arfken and H.-J. Weber, *Mathematical Methods for Physicists*, 6th ed (Elsevier, Boston, 2005).

[87] T. Hahn, *Cuba—a library for multidimensional numerical integration*, Computer Physics Communications **168**, 78–95 (2005).

[88] S. Das Sarma and Y. Liao, *Know the enemy: 2D Fermi liquids*, Annals of Physics **435**, 168495 (2021).

[89] J. J. Sakurai and J. Napolitano, *Modern Quantum Mechanics*, 2nd ed. (Cambridge University Press, Cambridge, 2017).

[90] S. Chapman and T. G. Cowling, *The Mathematical Theory of Non-Uniform Gases: An Account of the Kinetic Theory of Viscosity, Thermal Conduction and Diffusion in Gases* (Cambridge University Press, Cambridge, 1990).

[91] D. Enskog, *Kinetische theorie der Vorgänge in mässig verdünnten Gasen.* PhD thesis (Lund University, 1917).

[92] M. Stephanov and Y. Yin, *Hydrodynamics with parametric slowing down and fluctuations near the critical point*, Physical Review D **98**, 036006 (2018).

[93] S. Grozdanov, A. Lucas, and N. Poovuttikul, *Holography and hydrodynamics with weakly broken symmetries*, Physical Review D **99**, 086012 (2019).

[94] H. Rostami, N. Ben-Shachar, S. Moroz, et al., *Magnetic field suppression of tomographic electron transport*, Physical Review B **111**, 155434 (2025).

[95] S. Kryhin, Q. Hong, and L. Levitov, *Linear-in-temperature conductance in two-dimensional electron fluids*, Physical Review B **111**, L081403 (2025).

[96] D. Thuillier and T. Scaffidi, *AC Fingerprints of 2D Electron Hydrodynamics: Superdiffusion and Drude Weight Suppression*, 2026, arXiv:2603.15737.

[97] P. K. Kovtun, D. T. Son, and A. O. Starinets, *Viscosity in Strongly Interacting Quantum Field Theories from Black Hole Physics*, Physical Review Letters **94**, 111601 (2005).

[98] D. Forster, *Hydrodynamic Fluctuations, Broken Symmetry, and Correlation Functions*, 1st ed. (CRC Press, 2018).

[99] M. Ammon and J. Erdmenger, *Gauge/Gravity Duality: Foundations and Applications* (Cambridge University Press, Cambridge, 2015).

[100] J. M. Maldacena, *The Large N Limit of Superconformal Field Theories and Supergravity*, International Journal of Theoretical Physics **38**, 1113–1133 (1999).

[101] G. T. Horowitz, J. E. Santos, and D. Tong, *Optical conductivity with holographic lattices*, Journal of High Energy Physics **2012**, 168 (2012).

[102] L. Alberte, M. Ammon, A. Jiménez-Alba, et al., *Holographic Phonons*, Physical Review Letters **120**, 171602 (2018).

[103] M. Čubrović, J. Zaanen, and K. Schalm, *String Theory, Quantum Phase Transitions, and the Emergent Fermi Liquid*, Science **325**, 439–444 (2009).

[104] H. Liu, J. McGreevy, and D. Vegh, *Non-Fermi liquids from holography*, Physical Review D **83**, 065029 (2011).

[105] S.-S. Lee, *Non-Fermi liquid from a charged black hole: A critical Fermi ball*, Physical Review D **79**, 086006 (2009).

[106] U. Gran, M. Tornsö, and T. Zingg, *Holographic plasmons*, Journal of High Energy Physics **2018**, 176 (2018).

[107] E. Mauri and H. Stoof, *Screening of Coulomb interactions in Holography*, Journal of High Energy Physics **2019**, 35 (2019).

[108] A. Romero-Bermúdez, A. Krikun, K. Schalm, et al., *Anomalous attenuation of plasmons in strange metals and holography*, Physical Review B **99**, 235149 (2019).

[109] M. Tornsö, *Plasma Oscillations in Holographic Quantum Matter*, PhD thesis (Chalmers University of Technology, 2021).

[110] E. Witten, *Anti De Sitter Space And Holography*, 1998, arXiv:`hep-th/9802150`.

[111] S. S. Gubser, I. R. Klebanov, and A. M. Polyakov, *Gauge theory correlators from non-critical string theory*, Physics Letters B **428**, 105–114 (1998).

[112] P. Romatschke and U. Romatschke, *Viscosity Information from Relativistic Nuclear Collisions: How Perfect is the Fluid Observed at RHIC?*, Physical Review Letters **99**, 172301 (2007).

[113] Y. Kats and P. Petrov, *Effect of curvature squared corrections in AdS on the viscosity of the dual gauge theory*, Journal of High Energy Physics **2009**, 044–044 (2009).

[114] S. Das Sarma, S. Adam, E. H. Hwang, et al., *Electronic transport in two-dimensional graphene*, Reviews of Modern Physics **83**, 407–470 (2011).

[115] S. Sachdev, *Quantum Phase Transitions*, 2nd ed. (Cambridge University Press, 2011).

[116] S. Sachdev and J. Ye, *Gapless spin-fluid ground state in a random quantum Heisenberg magnet*, Physical Review Letters **70**, 3339–3342 (1993).

[117] A. Kitaev, *A simple model of quantum holography*, Kavli Institute for Theoretical Physics, 2015.

[118] A. A. Patel, H. Guo, I. Esterlis, et al., *Universal theory of strange metals from spatially random interactions*, Science **381**, 790–793 (2023).

[119] C. Li, D. Valentinis, A. A. Patel, et al., *Strange Metal and Superconductor in the Two-Dimensional Yukawa-Sachdev-Ye-Kitaev Model*, Physical Review Letters **133**, 186502 (2024).

[120] B. Michon, C. Berthod, C. W. Rischau, et al., *Reconciling scaling of the optical conductivity of cuprate superconductors with Planckian resistivity and specific heat*, Nature Communications **14**, 3033 (2023).

[121] R. A. Cooper, Y. Wang, B. Vignolle, et al., *Anomalous Criticality in the Electrical Resistivity of $La_{2-x}Sr_xCuO_4$*, Science **323**, 603–607 (2009).

[122] E. van Heumen, X. Feng, S. Cassanelli, et al., *Strange metal dynamics across the phase diagram of $Bi_2Sr_2CuO_{6+\delta}$ cuprates*, Physical Review B **106**, 054515 (2022).

[123] G.-A. Inkof, K. Schalm, and J. Schmalian, *Quantum critical Eliashberg theory, the Sachdev-Ye-Kitaev superconductor and their holographic duals*, npj Quantum Materials **7**, 56 (2022).

[124] R. Emparan, C. V. Johnson, and R. C. Myers, *Surface terms as counterterms in the AdS-CFT correspondence*, Physical Review D **60**, 104001 (1999).

[125] V. Balasubramanian and P. Kraus, *A Stress Tensor for Anti-de Sitter Gravity*, Communications in Mathematical Physics **208**, 413–428 (1999).

[126] T. Faulkner, H. Liu, J. McGreevy, et al., *Emergent quantum criticality, Fermi surfaces, and AdS 2*, Physical Review D **83**, 125002 (2011).

[127] J. Zaanen, *Lectures on quantum supreme matter*, 2021, arXiv:2110.00961.

[128] S. S. Gubser and F. D. Rocha, *Peculiar properties of a charged dilatonic black hole in AdS 5*, Physical Review D **81**, 046001 (2010).

[129] C. P. Herzog and D. T. Son, *Schwinger-Keldysh propagators from AdS/CFT correspondence*, Journal of High Energy Physics **2003**, 046 (2003).

[130] D. T. Son and A. O. Starinets, *Minkowski-space correlators in AdS/CFT correspondence: recipe and applications*, Journal of High Energy Physics **2002**, 042 (2002).

[131] D. T. Son and A. O. Starinets, *Viscosity, Black Holes, and Quantum Field Theory*, Annual Review of Nuclear and Particle Science **57**, 95–118 (2007).

[132] D. Vegh, *Holography without translational symmetry*, 2013, arXiv:1301.0537.

[133] R. A. Davison, *Momentum relaxation in holographic massive gravity*, Physical Review D **88**, 086003 (2013).

[134] M. Blake, D. Tong, and D. Vegh, *Holographic Lattices Give the Graviton an Effective Mass*, Physical Review Letters **112**, 071602 (2014).

[135] T. Andrade and B. Withers, *A simple holographic model of momentum relaxation*, Journal of High Energy Physics **2014**, 101 (2014).

[136] M. Baggioli, K.-Y. Kim, L. Li, et al., *Holographic axion model: A simple gravitational tool for quantum matter*, Science China Physics, Mechanics & Astronomy **64**, 270001 (2021).

[137] A. Donos and J. P. Gauntlett, *Holographic Q-lattices*, Journal of High Energy Physics **2014**, 40 (2014).

[138] D. M. DeTurck, *Deforming metrics in the direction of their ricci tensors*, Journal of Differential Geometry **18**, 157–162 (1983).

[139] M. Headrick, S. Kitchen, and T. Wiseman, *A new approach to static numerical relativity and its application to Kaluza–Klein black holes*, Classical and Quantum Gravity **27**, 035002 (2010).

[140] M. Rangamani, M. Rozali, and D. Smyth, *Spatial modulation and conductivities in effective holographic theories*, Journal of High Energy Physics **2015**, 24 (2015).

[141] A. Donos and J. P. Gauntlett, *Thermoelectric DC conductivities from black hole horizons*, Journal of High Energy Physics **2014**, 81 (2014).

[142] A. Donos and J. P. Gauntlett, *The thermoelectric properties of inhomogeneous holographic lattices*, Journal of High Energy Physics **2015**, 35 (2015).

[143] E. Banks, A. Donos, and J. P. Gauntlett, *Thermoelectric DC conductivities and Stokes flows on black hole horizons*, Journal of High Energy Physics **2015**, 103 (2015).

[144] A. Donos, J. P. Gauntlett, T. Griffin, et al., *Holographic DC conductivity and Onsager relations*, JHEP **07**, 006 (2017).

[145] F. Balm, *Translational symmetry breaking in holographic strange metals*, PhD thesis (Leiden University, 2023).

[146] P. Kovtun, *Lectures on hydrodynamic fluctuations in relativistic theories*, Journal of Physics A: Mathematical and Theoretical **45**, 473001 (2012).

[147] E. Nilsson and K. Schalm, *Quantum critical theories in a periodic potential: strange metallic thermoelectric and magneto-transport*, 2025, arXiv:2512.19480.

[148] R. A. Davison and B. Goutéraux, *Dissecting holographic conductivities*, Journal of High Energy Physics **2015**, 90 (2015).

[149] N. Chagnet and K. Schalm, *Hydrodynamics of a relativistic charged fluid in the presence of a periodically modulated chemical potential*, SciPost Physics **16**, 028 (2024).

[150] P. Chesler, A. Lucas, and S. Sachdev, *Conformal field theories in a periodic potential: Results from holography and field theory*, Physical Review D **89**, 026005 (2014).

[151] A. Carrington, A. P. Mackenzie, C. T. Lin, et al., *Temperature Dependence of the Hall Angle in Single-Crystal YBa_2 $(Cu_{1-x}Co_x)_3$ $O_{7-\delta}$*, Physical Review Letters **69**, 2855–2858 (1992).

[152] N. Chagnet, S. Arend, F. Balm, et al., *Natural anomalous cyclotron response in a hydrodynamic local quantum critical metal in a periodic potential*, 2024, arXiv:2409.11095.

[153] A. A. Patel, J. McGreevy, D. P. Arovas, et al., *Magnetotransport in a Model of a Disordered Strange Metal*, Physical Review X **8**, 021049 (2018).

[154] C. Boyd and P. W. Phillips, *Single-parameter scaling in the magnetoresistance of optimally doped $La_{2-z}Sr_xCuO_4$*, Physical Review B **100**, 155139 (2019).

[155] K. Maeda, M. Natsuume, and T. Okamura, *Two pieces of folklore in the AdS/CFT duality*, Physical Review D **82**, 046002 (2010).

[156] S. A. Hartnoll, C. P. Herzog, and G. T. Horowitz, *Building a Holographic Superconductor*, Physical Review Letters **101**, 031601 (2008).

[157] M. Natsuume and T. Okamura, *Holographic Meissner effect*, Physical Review D **106**, 086005 (2022).

[158] M. E. Peskin and D. V. Schroeder, *An Introduction To Quantum Field Theory* (CRC Press, 2018).

[159] E. Witten, *Multi-Trace Operators, Boundary Conditions, And AdS/CFT Correspondence*, 2002, arXiv:`hep-th/0112258`.

[160] W. Mück, *An improved correspondence formula for AdS/CFT with multi-trace operators*, Physics Letters B **531**, 301–304 (2002).

[161] E. Mauri, *Applications of the gauge/gravity duality to the cuprate strange metal*, PhD thesis (Utrecht University, 2022).

[162] U. Gran, M. Tornsö, and T. Zingg, *Exotic holographic dispersion*, Journal of High Energy Physics **2019**, 32 (2019).

[163] U. Gran, M. Tornsö, and T. Zingg, *Holographic response of electron clouds*, Journal of High Energy Physics **2019**, 19 (2019).

[164] M. Baggioli, U. Gran, A. J. Alba, et al., *Holographic plasmon relaxation with and without broken translations*, Journal of High Energy Physics **2019**, 13 (2019).

[165] T. Andrade, A. Krikun, and A. Romero-Bermúdez, *Charge density response and fake plasmons in holographic models with strong translation symmetry breaking*, Journal of High Energy Physics **2019**, 159 (2019).

[166] U. Gran, N. Jokela, D. Musso, et al., *Holographic fundamental matter in multilayered media*, Journal of High Energy Physics **2019**, 38 (2019).

[167] U. Gran, M. Tornsö, and T. Zingg, *Plasmons in Holographic Graphene*, SciPost Physics **8**, 093 (2020).

[168] S. T. Van Den Eede, T. J. N. van Stralen, C. F. J. Flipse, et al., *Plasmons in a layered strange metal using the gauge-gravity duality*, Physical Review B **109**, 085119 (2024).

[169] S. Grozdanov and N. Poovuttikul, *Generalised global symmetries in holography: magnetohydrodynamic waves in a strongly interacting plasma*, Journal of High Energy Physics **2019**, 141 (2019).

[170] O. DeWolfe and K. Higginbotham, *Generalized symmetries and 2-groups via electromagnetic duality in AdS/CFT*, Physical Review D **103**, 026011 (2021).

[171] M. Baggioli, U. Gran, and M. Tornsö, *Collective modes of polarizable holographic media in magnetic fields*, Journal of High Energy Physics **2021**, 14 (2021).

[172] Y. J. Ahn, M. Baggioli, K.-B. Huh, et al., *Holography and magnetohydrodynamics with dynamical gauge fields*, Journal of High Energy Physics **2023**, 12 (2023).

[173] G. Compère and D. Marolf, *Setting the boundary free in AdS/CFT*, Classical and Quantum Gravity **25**, 195014 (2008).

[174] A. Ishibashi, K. Maeda, and T. Okamura, *Semiclassical Einstein equations from holography and boundary dynamics*, Journal of High Energy Physics **2023**, 212 (2023).

[175] X. Wang and D. Chowdhury, *Collective density fluctuations of strange metals with critical Fermi surfaces*, Physical Review B **107**, 125157 (2023).

[176] J. Levallois, M. K. Tran, D. Pouliot, et al., *Temperature-Dependent Ellipsometry Measurements of Partial Coulomb Energy in Superconducting Cuprates*, Physical Review X **6**, 031027 (2016).

[177] A. A. Husain, M. Mitrano, M. S. Rak, et al., *Crossover of Charge Fluctuations across the Strange Metal Phase Diagram*, Physical Review X **9**, 041062 (2019).

[178] J. Fink, *Comment on: Crossover of Charge Fluctuations across the Strange Metal Phase Diagram*, 2021, arXiv:2103.10268.

[179] A. Husain, M. Mitrano, M. S. Rak, et al., *Reply to arXiv:2103.10268 'Comment on "Crossover of Charge Fluctuations across the Strange Metal Phase Diagram"'*, 2021, arXiv:2106.03301.

[180] J. Chen, X. Guo, C. Boyd, et al., *Consistency between reflection momentum-resolved electron energy loss spectroscopy and optical spectroscopy measurements of the long-wavelength density response of* $Bi_2Sr_2CaCu_2O_{8+x}$, Physical Review B **109**, 045108 (2024).

[181] P. Abbamonte and J. Fink, *Collective charge excitations studied by electron energy-loss spectroscopy*, 2024, arXiv:2404.04670.

[182] M. Hepting, L. Chaix, E. W. Huang, et al., *Three-dimensional collective charge excitations in electron-doped copper oxide superconductors*, Nature **563**, 374–378 (2018).

[183] S. Vig, A. Kogar, M. Mitrano, et al., *Measurement of the dynamic charge response of materials using low-energy, momentum-resolved electron energy-loss spectroscopy (M-EELS)*, SciPost Physics **3**, 026 (2017).

[184] S. A. Maier, *Plasmonics: Fundamentals and Applications* (Springer US, New York, NY, 2007).

[185] A. Liebsch, *Electronic Excitations at Metal Surfaces* (Springer US, Boston, MA, 1997).

[186] T. Senthil, S. Sachdev, and M. Vojta, *Fractionalized Fermi Liquids*, Physical Review Letters **90**, 216403 (2003).

[187] N. Iqbal and H. Liu, *Luttinger's theorem, superfluid vortices and holography*, Classical and Quantum Gravity **29**, 194004 (2012).

[188] D. V. Else, R. Thorngren, and T. Senthil, *Non-Fermi Liquids as Ersatz Fermi Liquids: General Constraints on Compressible Metals*, Physical Review X **11**, 021005 (2021).

[189] D. V. Else, *'t Hooft anomalies in metals*, 2025, arXiv:2502.19471.

[190] D. V. Else, *Holographic models of non-Fermi liquid metals revisited: An effective field theory approach*, Physical Review B **109**, 035163 (2024).

[191] P. Anderson, *Hall effect in the two-dimensional Luttinger liquid*, Physical Review Letters **67**, 2092–2094 (1991).

[192] E. Mauri and H. T. C. Stoof, *Coulomb drag between two strange metals*, Physical Review B **106**, 205116 (2022).